Sudan University of Science and Technology

Collage of Graduate Studies

Developing a Real Time Algorithm for Diagnosing Glaucoma

تطوير خوارزمية زمن حقيقى لتشيخص الجلايكوما

A thesis submitted to fulfillment of the requirements for the award of the degree of Doctor of Philosophy

In

Biomedical Engineering

Arwa Ahmed Gasm Elseid Ahmed

Supervisor:

Professor: Alnazier Ahmed Osman Hamza

Co Supervisor: Dr. Ahmed Fragoon

August, 2018

LIST OF PUBLICATIONS

 Arwa Ahmed Gasm Elseid, Mohamed Eltahir Elmanna, Alnazier Osman Hamza, Evaluation of Spatial Filtering Techniques in Retinal Fundus Images, American Journal of Artificial Intelligence. Vol. 2, No. 2, 2018, pp. 16-21. doi: 10.11648/j.ajai.20180202.11.

 Arwa Ahmed, and Alnazier Osman (2018). Optic Disc Segmentation Using Manual Thresholding Technique, Journal of Clinical Engineering, Vol. 44, N0.1, issue: January/March 2019, Copyright © 2018 Wolters Kluwer Health.

 Arwa Ahmed Gasm Elseid, Alnazier Osman Hamza, and Ahmed Fragoon (2018). Developing A Real Time Algorithm For Diagnosing Glaucoma, ICTACT Journal On Image And Video Processing, VOL.09, ISSUE: 02.

 Arwa A. Gasm Elseid and Alnazier O. Hamza (2018). Glaucoma Detection Based On Shape Features and SMOTE Algorithm, CiiT International Journal of Digital Image Processing, Vol. 10, No. 10, ISSUE: October – November.

DEDICATION

To my parents and family

ACKNOWLEDGEMENTS

First and foremost, thanks should be expressed to Allah for his assistance and for giving me the opportunity of being engaged in this study, and great help to overcome all the difficulties throughout the period of my research. I would like to thank Prof. Alnazier Osman Hamza my supervisor who help me in completing this study by his great efforts and continues guidance and assessment. Also I would like to express my deepest thanks to Dr. Fragoon Mohamed Ahmed for his precious advice and support. Special thank goes to Dr. Ahmed Gasm Elseid, Dr. Egbal Suliman. Finally, I shall be eternally grateful to members of my family; my husband Eng. Sohaib Abd Elgawiy and my kids. I thank all those who assisted and supported me during this study.

ABBREVIATION

ACG	Angle Closure Glaucoma.
AMD	Age-Related Macular Degenerate.
AUC	Area Under Curve.
BRIEF	Binary Robust Independent Elementary Features.
CAD	Computer Aided Diagnosis.
CDR	Cup to Disc Ratio.
CFI	Colors Funds Image.
CSL	Cost Sensitive Learning.
CSLO	Confocal Scanning Laser Ophthalmoscopy.
DOG	Difference of Gaussians.
DSC	Disc Similarity Coefficient.
DWT	Discrete Wavelet Transform
FA	Fluorescein Angiography.
FAF	Funds Auto Fluorescein.
FN	False Negative.
FP	False Positive.
FPR	False Positive Rate.
GLCM	Gray Level Co- Occurrence.
GMRF	Gaussian Markov random fields
GRI	Glaucoma Risk Index
GUI	Graphical User Interface.
HOS	Higher Order Spectra
HRT	Heidelberg Retinal Tomography.
HRT	Heidelberg Retinal Tomography.
HSI	Hue, Saturation and Intensity.
IOP	Intraocular Pressure.
ISNT	Inferior, Superior nasal and temporal.
K-NN	K-Nearest Neighbors algorithm.
LOG	Laplacian of Gaussian.
MSF	Mean Squared Error.

NTG	Normal Tension Glaucoma
OAG	Open Angle Glaucoma.
OC	Optic Cup.
OCT	Optical Coherence Tomography.
OCT	Optical Coherence Tomography.
OD	Optic Disc.
ONH	Optic Nerve Head.
PPA	Parapapillary Atrophy.
PSNR	Peak Signal Noise Ratio.
RBF	Radial Basis Function
RGB	Red, Green, Blue Channels.
RNFL	Rental Nerve Fiber Layer.
ROC	Receiver Operating Characteristic.
SBFS	Sequential Backward Floating Selection.
SBS	Sequential Backward Selection.
SFFS	Sequential Forward Floating Selection.
SFS	Sequential Feature Sector.
SFS	Sequential Forward Selection.
SLIC	Simple Linear Iterative Clustering algorithm.
SMOTE	Synthetic Minority Over-sampling Technique.
SNR	Signal to Noise Ratio.
SSIM	Structural Similarity.
STD	Standard Deviation.
SVM	Support Vector Machine.
TN	True Negative.
TP	True Positive.
TPR	True Positive Rate.
TT	Trace Transform
WHO	World Health Organization.

ABSTRACT

A Glaucoma is a group of eye diseases causing optic nerve damage, as it has no symptoms and if not detected at an early stage it may cause permanent blindness. Glaucoma progression precedes some structural damage to the retina are the marked symptoms of Glaucoma. Mainly, it is diagnosed by examination of size, structure, shape, and color of the optic disc (OD) and optic cup (OC) and retinal nerve fiber layer (RNFL), which suffer from the subjectivity of human due to experience, fatigue factor etc. Fundus camera is among one of the biomedical imaging techniques to analyze the internal structure of retina, with the widespread adoption of higher quality medical imaging techniques and data, there are increasing demands for medical image-based computer-aided diagnosis (CAD) systems for glaucoma detection, because the human mistakes, other retinal diseases like Age-related Macular Degeneration (AMD) and the existing medical devices like Optical Coherence Tomography (OCT) and Heidelberg Retinal Tomography (HRT) affecting in early glaucoma detection. The proposed technique provides a novel algorithm to detect glaucoma from digital fundus image using combined features set and evaluation of proposed algorithm is performed using a RIM_ONE (version two) database containing fundus images from 158 patients (118 healthy and 40 glaucoma image), Drishti_GS which contain 101 fundus images (70 glaucoma image and 31 healthy images), and RIM_ONE (version one) which contain (200 glaucoma and 255 healthy images) via Matlab software. The proposed system used to detect glaucoma via 3 steps; firstly, OD and OC segmentation. In OD and OC segmentation several steps were done like prepressing, thresholding, boundary smoothing and disc reconstruction to be a full circle where, OD segmentation achieved best dice coefficient (DSC) 90% and Structural Similarity (SSIM) 83% and OC segmentation results are dice coefficient 73% and Structural Similarity (SSIM) 93%, secondly shape, color, and texture features were extracted from segmented parts and then select the most relevant features, thirdly and finally many classifiers were applied to find the best classification accuracy, which was the support vector machine (SVM). This research proposes a novel combination of color-based, shape-based and texture features by extract 13 shape features from disc and cup, extract 25 texture features from RNFL(retinal nerve fiber layer) using gray level co-occurrence method and Tamar algorithm and 3 color feature for each of disc, cup, and RNFL. Next, best features were selected by T-test method and Sequential feature selection (SFS) to introduce eight features with average accuracy 97%, maximize area under

curve (AUC) 0.99, specificity 96.6% and sensitivity 98.4% to the first database and 91.5 and 94.5 to the second, and third database respectively with training time 1.5623 sec and prediction time 2600 obs/sec (One billionth of a second). The proposed algorithm achieved excellent performance compared with previous studies from 2011 until now in features types and overall performance. The key contribution in this work is the proposed real-time algorithm for glaucoma detection with high accuracy achieved, the proposed method can make a valuable contribution to medical science by supporting medical image analysis for glaucoma detection. Future works suggested to design a complete, integrated, automated system to classify all different types of glaucoma namely: Primary Open-Angle Glaucoma, Normal Tension Glaucoma, Angle Closure Glaucoma, Acute Glaucoma, Exfoliation Syndrome and Trauma-Related Glaucoma, and to upgrade the system to compute the progress of the disease by comparing different image of the same patient to be used for follow up.

المستخلص

الجلوكوما هو مجموعة من أمراض العيون التي تسبب تلف العصب البصري ، لأنه لا يوجد لديه أعراض وإذا لم يتم الكشف عنها في مرحلة مبكرة فإنها قد تسبب العمى الدائم. تسبق زرق الجلوكوما بعض الأضرار الهيكلية في شبكية العين وهي الأعراض الملحوظة للجلوكوما. بشكل رئيسي يتم تشخيص الجولوكوما من خلال فحص حجم وبنية وشكل ولون القرص البصري (OD) والكأس البصرية (OC) وطبقة الألياف العصبية للشبكية (RNFL) ، والتي تعاني من ذاتية الإنسان بسبب الخبرة ، عامل التعب الخ .

كاميرا قاع العين هي واحدة من تقنيات التصوير الطبي الحيوي لتحليل البنية الداخلية لشبكية العين ، مع اعتماد واسع النطاق لتقنيات وبيانات التصوير الطبي ذات الجودة العالية ، هناك طلبات متزايدة على أنظمة التشخيص بمساعدة الحاسوب (CAD)القائمة على الصور الطبية للكشف عن الجلوكوما ، وذلك لأن الأخطاء البشرية ، وأمراض الشبكية الأخرى مثل التنكس البقعي المرتبط بالعمر (AMD) والأجهزة الطبية القائمة مثل التصوير البصرى المقطعى(OCT) و هايدلبرغ الشبكية التصوير المقطعي (HRT) (مرتفعة الثمن وذلك يؤثر في الكشف المبكر للزرق. توفر التقنية المقترحة خوارزمية جديدة للكشف عن الجلوكوما من صورة القاعدة رقمية باستخدام مجموعة من الميزات المشتركة ويتم تقييم الخوارزمية المقترحة باستخدام قاعدة بيانات RIM_ONE (الإصدار الثاني) التي تحتوي على 158صور قاعدية من118 مريض و40 صورة صحية ، Drishti_GS التي تحتوي على 101 صورة قاعدية 70 صورة من الجلوكوما و 31 صورة صحية.

RIM_ONE (الإصدار الأول) التي تحتوي على 244 جولوكوما و 255 صورة صحية عبر برنامج

Matlab يستخدم النظام المقترح للكشف المبكرعن الجلوكوما 1 خطوات: الخطوة الأولى ، تقسيم القرص البصري (OD) والكأس البصرية(OC) في تجزيء OD و OC تم إجراء عدة خطوات مثل prepressing و thresholding وتمهيد الحدود وإعادة تشكيل القرص لتكون دائرة كاملة حيث حققت تقسيم OD أفضل معامل نرد (DSC) 90 ٪ وتشابه بنيوي (SSIM) 83٪ ونتائج تجزئة OCتم استخراج معامل النرد 73 ٪ والتشابه البنيوي93 ٪ ، والخطوة الثانية :إستخراج ميزلت اللون والشكل والبنية من الأجزاء المجزأة ثم حددت الميزات الأكثرملاءمة ، والخطوة الثالثة والاخيرة: تم

تطبيق العديد من المصنفات للعثور على أفضل دقة للتصنيف ، والتي كانت دعم ناقلات الجهاز) . SVM)

يقترح هذا البحث مزيجًا جديدًا من الميزات المستندة إلى الألوان والقائمة على الأشكال والقوام عن طريق استخلاص 13 شكلًا من الميزات من القرص والكوب ، واستخلاص 25 من خصائص النسيج من RNFL (طبقة ألياف العصب في الشبكية) باستخدام طريقة التواجد بمستوى الرمادي وخوارزمية تمار و ميزة 3 لون لكل قرص ، وكأس ، و RNFL. بعد ذلك ، تم اختيار أفضل الميزات بواسطة طريقة T-test وميزة اختيار التسلسل (SFS) لتقديم ثمانية ميزات بمتوسط دقة 97٪ ، وتعظيم المساحة تحت المنحنى 0.99 (AUC) ، وخصوصية 96.6٪ والحساسية 98.4٪ لقاعدة البيانات الأولى و 91.5 و 94.5 إلى الثانية ، وقاعدة البيانات الثالثة على التوالي مع وقت التدريب 1.5623 ثانية ووقت التنبؤ 2600 م / ثانية (واحد من مليار من الثانية). حققت الخوارزمية المقترحة أداءً ممتازًا مقارنة بالدراسات السابقة من عام 2011 وحتى الآن في أنواع الميزات والأداء العام. وتتمثل المساهمة الرئيسية في هذا العمل في الخوارزمية المقترحة في الوقت الفعلي للكشف عن الجلوكوما بدقة عالية ، ويمكن أن تسهم الطريقة المقترحة إسهاما قيما في العلوم الطبية من خلال دعم تحليل الصور الطبية للكشف عن المياه الزرقاء. واقترح أعمال في المستقبل لتصميم ومتكامل نظام كامل، آلية لتصنيف جميع أنواع مختلفة من الجلوكوما هي: الابتدائية المفتوح زاوية الزرق، التوتر العادي الزرق، زاوية إغلاق الزرق، الحادة الزرق، متلازمة تقشير والزرق الصدمة، ذات، ورفع مستوى نظام لحساب تقدم المرض من خلال مقارنة صورة مختلفة للمريض نفسه لاستخدامها في المتابعة.

Table of Content

Title	Page
DEDICATION	I
ACKNOWLEDGEMENTS	II
Abbreviation	III
Abstract	V
Table of Contents	VII
List of Tables	XI
List of Figures	XIII
CHAPTER ONE: INTRODUCTION	
1.1 Background	1
1.1.1 Tonometry	3
1.1.2 Ophthalmoscopy	3
1.1.3 Gonioscopy	3
1.1.4 Visual Field Testing	4
1.1.5 Nerve Fiber Analysis	4
1.1.6 Pachymetry	4
1.2 Computer Aided Diagnosis	4
1.3 Problem of the Study	5
1.4 Objectives	7
1.4.1 General aim	7
1.4.2 Specific Objectives are to	7
1.5 Research Methodology	7
1.6 Significance of the Study	9
1.7 Contributions	10
1.8 Organization of the Thesis	10
CHAPTER TWO: MEDICAL BACKGROUND	
2.1 Introduction	11
2.2 The Human Eye	11
2.2.1 Structure of the Human Eye	11
2.3 Image Acquisition of the Retina	14
2.3.1 Fundus Image Capture	14
2.3.2 Other Imaging Devices	15
2.4 The Glaucoma Disease	18
2.4.1 Glaucoma and the Visual Pathway	20
2.5 Glaucoma Diagnosis	21

2.5.1 Optic Nerve Head 22
2.5.2 Intraocular Pressure 23
2.5.3 Visual field Function 23
2.5.4 Glaucoma Assessment 25
2.5.5 Glaucoma ONH Evaluation 27
2.5.5.1 Cup-to-Disc Ratio 27
2.5.5.2Parapapillary Atrophy 28
2.5.5.3 Disc Hemorrhage 29
2.5.5.4 Notching 30
2.5.5.5 Neuroretinal Rim Thinning 31
2.5.5.6 Inter-eye Asymmetry 32
2.5.5.7 Retinal Nerve Fiber Layer Defect 32
2.6 Motivation of Fundus Image Processing 33
2.6.1 Fundus Image Processing 34
2.6.2 Channel Separation 35
2.6.3 Histogram Equalization 35
2.6.4 Filtering 37
2.6.5 Morphological Processing 39
2.7 Feature Extraction Background 45
2.8 Shape Features 48
2.8.1 The Centroid 48
2.8.2 Eccentricity 49
2.8.3 Solidity 49
2.8.4 Area 49
2.8.5 Major axes 49
2.8.6 Minor axes 49
2.8.7 Extent 50
2.8.8 perimeter 50
2.9 Color Feature 50
2.9.1 Mean 51
2.9.2 Standard Deviation 51
2.9.3 Skewness 51
2.10 Texture Feature 51
2.10.1 GLCM Algorithm 52
2.11 Tamara Method 55
2.11.1 Coarseness 55
2.11.2 Contrast 56
2.11.3 Direction Degrees 56
2.12 Feature Selection 57

2.12.1 Sequential Feature Selector 58
2.12.2 Sequential Forward Selection (SFS) 58
2.13 Classification 60
2.13.1 Statistical Classification Methods 60
2.13.2 Rule-Based Systems 60
2.13.3 Support Vector Machine (SVM) 61
2.13.4 k-Nearest Neighbors Algorithm (*k*-NN) 62
2.13.5 Some advantages and dis-advantages of KNN 64
2.13.5.1 Advantages 64
2.13.5.2 Disadvantages 64
2.13.6 Ensemble Learning 64
2.13.6.1 Bootstrap Aggregating (Bagging) 65
2.13.6.2 Boosting 65
2.14 Classification Imbalanced 66
2.15 Theoretical Conclusion 67
CHAPTER THREE: RELATED WORKS
3.1 OD and OC Segmentation 69
3.2 Disc to Cup Ratio (CDR) 75
3.3RNFL Review 82
CHAPTER FOUR: RESEARCH METHODOLGY
4.1 Introduction 95
4.2 Fundus Image Datasets 95
4.2.1 RIM- ONE Database(version two) 96
4.2.2 Drishti –GS Database 97
4.2.3 RIM- ONE Database (version one) 98
4.3 Programming Environment 98
4.4 Methodology 99
4.4.1 Image Preprocessing and Enhancement 99
4.4.2 Segmentation 101
4.4.2.1 Optic Disc Segmentation 101
4.4.2.2 Optic Cup Segmentation 103
4.4.2.3 Cup Proposed Method 103
4.4.3 RNFL ROI Extraction 105
4.4.4 Feature Extraction Step 105
4.4.5 Features Selection 108
4.4.6 Classification 109
4.4.7 Validation and Comparison 109
4.4.8. Evaluation Parameters 109
4.4.9 Graphical User Interface 113

CHAPTER FIVE: RESULTS AND DISCUSSIONS
5.1 Introduction 114
5.2 Section one Image preparing 114
5.2.1 Image Preprocessing and Enhancement step 114
5.2.2 Channel Separation Results 116
5.2.3 Image Noise Filtration Results 116
5.2.4 Optic disc segmentation Step 121
5.2.4.1 OD discussion 125
5.2.5 Optic Cup Segmentation Step 127
5.2.5.1 Experimental Results 128
5.2.5.2 OC Discussion 131
5.2.6 RNFL ROI Extraction Step 132
5.3 Section two Glaucoma detection 133
5.3.1 Feature Extraction Step 133
5.3.1.1 Shape Features 133
5.3.1.2 Color Features 136
5.3.1.3 Texture Features 140
5.3.1.4 combined Features 143
5.4 section three Classification 144
5.4.1 Shape features classification 147
5.4.2 Color features classification 150
4.5.3 Texture features classification 152
4.5.4 Combined features classification 154
CHAPTER SIX: CONCLUSION AND FUTURE SCOPE
6.1 Conclusions 164
6.2 Future Scope 166
REFERANCE 167

LIST OF TABLES

No	Subject	Page
2.1	Overview comparison of retinal acquisition devices	17
3.1	Comparison between different segmentation methods	92
3.2	Comparison between different features types used to detect glaucoma from digital fundus images	93
5.1	Mean value of comparison of PSNR, SNR, SSIM and MSE, parameters to 158 images for Adaptive, Guided, Gaussian, Mean and Median filters in the original image corrupted by Gaussian noise (0.05)	117
5.2	Comparison of PSNR, SNR, SSIM and MSE, values for Adaptive, Guided, Gaussian, Mean and Median filters in the original image corrupted by salt& paper noise (0.02).	118
5.3	PSNR of different filtering methods (Salt & Pepper Noise)	119
5.4	PSNR of different filtering methods (Gaussian Noise)	120
5.5	The mean value of the DSC, jaccard coefficient and SSIM acquired using 158 images segmented by proposed method and compared with the five ground truth in the database.	124
5.6	Comparison of the proposed method against other segmentation methods (Otsu Thresholding, global Thresholding) by same database and same evaluation parameters.	124
5.7	Comparison of the proposed method against other segmentation methods by same database and same evaluation parameters.	130
5.8	Illustrates an example of the cup shape features for only 10 image.	134
5.9	Illustrates an example of the disc shape features only for	134

	only 10 images.	
5.10	Shows the t-test results from the shape features.	135
5.11	The selected shape features for the glaucoma and healthy images.	136
5.12	Illustrates an example of cup color features for only 10 images.	137
5.13	Illustrates an example of disc color features for only 10 images	137
5.14	Illustrates an example of RNFL color features for only 10 images	138
5.15	Shows the t-test results from the color features.	139
5.16	Illustrates the mean value of the selected color features for 40 glaucoma and 118 healthy images.	140
5.17	Illustrates an example of RNFL texture features for only 10 images	141
5.18	Shows the selected feature by SFS method	141
5.19	Shows the t-test results from the texture features.	143
5.20	Shows the different types of features classification results at 10 folds.	156
5.21	Shows the proposed method classification results in the 2 database at 10 folds.	157
5.22	Shows the Comparisons of the research method with previous studies.	158
5.23	Shows the comparisons of the proposed system with previous studies used the same databases.	161
5.24	Shows the final proposed system evaluation parameters values.	162

LIST OF FIGURES

Fig. No.	Description	Page
1.1	Shows an example of fundus image obtained from fundus camera used for glaucoma detection.	2
1.2	Shows the proposed algorithm approach for detecting glaucoma in color fundus images.	8
2.1	Shows the Human Eye inside and outside structure.	11
2.2	Shows anatomy and schematic diagram of the human eye (a) Sagittal view of the human eye with a schematic enlargement of the Retina, (b) Example of a retina image, (C) Schema of the layers of the developing retina around 5 month's gestation (Modified from (Odgen, 1989).	13
2.3	Shows images produced via angiography as a type from the fundus image	15
2.4	Shows images produced via Fundus Auto Fluorescence device as a type from the fundus image	16
2.5	Shows images produced via Heidelberg Retina Tomography as a type from the fundus image	16
2.6	Shows images produced via Optical Coherence Tomography, can used to detect glaucoma	17
2.7	The distribution of open angle glaucoma (OAG) and angle closure glaucoma (ACG) in the year 2010 and 2020 according to the estimation in (Quigley and Broman, 2006).	19
2.8	Fundus images showing the background of the retina for a (a) healthy subject and a glaucoma (b) patient	23
2.9	Two sample HRT-II images for a healthy subject (a) and a glaucoma (b) patient. The glaucomatous cupping is present in the optic nerve head.	24
2.10	An example of a circular optical coherence tomography (OCT) scan around the optic disc. The retinal nerve fiber layer is segmented and the different retinal layers.	24
2.11	Anatomy of the Optic Nerve Head - Clinical features of the optic nerve (Community eye health, 2017).	24
2.12	Progression of OC Enlargement Changes in Glaucoma (Left) a normal ONH. (Centre) Early glaucoma ONH. (Right) Advanced glaucoma ONH.	25

2.13	Shows (a) Vision with normal eye (b) Vision with abnormal eye (Eye diseases, 2017).	25
2.14	Cup-to-Disc Ratio - The vertical cup-to-disc ratio is used as clinical measure in assessing glaucoma.	27
2.15	Measurement of cup to disc ratio (CDR) on fundus image, used as indicator of glaucoma big CDR suspected of having glaucoma.	28
2.16	Grading of PPA according to scale, occurs more frequently in glaucomatous eyes.	29
2.17	Disc hemorrhage in the inferior temporal side indicate to glaucoma.	30
2.18	Shows an example of focal notching of the rim, Left notch at 7 o'clock, which is indicator of glaucoma, Right healthy disc.	31
2.19	Shows rim widths in the inferior, superior, nasal and temporal sectors, also indicators to the glaucoma disease based on ISNT rule.	31
2.20	Shows an example of inter-eye asymmetry of optic disc cupping. Left eye with small CDR. Right eye with large CDR, where a big CDR usually considered to be a significant asymmetry and indicator of glaucoma.	32
2.21	Show an examples of RNFL defect. (a) Cross section view of normal RNFL. (b) Cross section view of RNFL defect. (c) Normal RNFL in fundus image. (d) RNFL defect in fundus image.	33
2.22	A) Original color retinal image, b) Highlighting ill-defined boundary region and image variation near OD boundary due to atrophy (a pathological change).	45
2.23	Show support vector machines	61
4.1	Shows Eye RIM-ONE database images (a) Normal image, (d) Glaucoma image (abnormal), an example of images used in the research.	95
4.2	Show examples of normal fundus images from RIM-ONE database.	96
4.3	An examples the abnormal fundus images from RIM-ONE database.	97
4.4	Shows an examples the original fundus images from drishti _GS database.	97
4.5	Shows an examples the ROI fundus images from drishti	98

	_GS database.	
4.6	Proposed Methodology used in this research to diagnose glaucoma disease.	99
4.7	Shows the preprocessing steps, the gray box was the selected methods.	100
4.8	Shows the segmentation steps, the gray box was the selected methods.	101
4.9	Proposed method for optic disc segmentation algorithm.	102
4.10	Cup segmentation proposed algorithm based on thresholding technique from optic disc region.	104
5.1	Shows the steps of an image enhancement for healthy image show the original image, image after resized, the channel selected, image histogram (x-axis to show intensity levels and y-axis intensity values), image after histogram equalization and filtered image.	115
5.2	Shows the steps of image enhancement for glaucoma image show the original image, image after resized, the channel selected, image histogram (x-axis to show intensity levels and y-axis intensity values), image after histogram equalization and filtered image.	115
5.3	Shows digital fundus image color channels extraction as the red, green and blue channel to select the best one suitable for the segmentation.	116
5.4	Shows an example of different filters applied in (salt& paper) noisy glaucoma image: the original image, mean, median, adaptive, Gaussian and guided filters.	117
5.5	Bar chart show the comparison between the different filters types applied to image corrupted by Gaussian noise.	118
5.6	Bar chart show the comparison between the different filters types applied to the original image corrupted by salt &paper noise.	119
5.7	Bar chart shows results of filtration applied to the original image at different level of Salt & Pepper Noise.	120
5.8	Bar chart shows results of filtration applied to the original image at different level of Gaussian Noise.	120
5.9	Show glaucoma image OD segmentation steps as vessel remove, thresholding, post processing and circle	122

	reconstruction (A) wrong OD segmentation duo to PPA affect (B) right OD segmentation.	
5.10	Shows healthy image OD segmentation steps as vessel remove, thresholding, post processing and circle reconstruction (C) right OD segmentation (D) wrong OD segmentation.	122
5.11	Shows comparison results of different segmentation algorithms (a) Original image (b) ground truth image (c) Otsu Thresholding (d) Global Thresholding (e) Proposed method.	123
5.12	Bar chart show comparison between 3 different types of segmentation applied for disc segmentation to the same database.	124
5.13	Shows accurate segmentation (a) the original image (b) ground truth OD (c) proposed OD (d) absolute difference between the two images too small.	125
5.14	Shows inaccurate segmentation (e) the original image (f) ground truth OD (g) proposed OD (h) absolute difference between the two images too big.	125
5.15	Shows an example of non-segmented images duo to some reasons like (i) big size PPA (j) non-uniform illumination.	126
5.16	Shows an example of segmented disc images with main blood vessels (a): original image, (b) segmentation output before circle construction.	126
5.17	Sample Images and Ground-Truth in Drishti_GS dataset - (From Left to Right) Original image (2047x1751) in the dataset, Ground-truth Optic Disc Mask, proposed segmented Optic Cup Mask.	128
5.18	Show a cup segmentation and binarization from the disc part for glaucoma image using global thresholding technique.	129
5.19	Shows a cup segmentation and binarization from the disc part for healthy image using global thresholding technique.	129
5.20	Show (a) the original image (b) ground truth image (c) super pixel segmentation (d) super pixel segmentation with circle construction (e) global thresholding (f) global Thresholding segmentation with circle construction.	130
5.21	Bar chart illustrates the comparison between different	131

	segmentation techniques.	
5.22	An examples of un segmented image duo to ROI bad localization.	131
5.23	Show RNFL for glaucoma image,which is apart surrounded the disc.	132
5.24	Show RNFL for healthy image, extracted by substract the optic nerve head from the segmented optic disc.	133
5.25	Bar chart shows the cup minor axes and disc solidity for 40 glaucoma images and 118 healthy images	136
5.26	Bar chart of selected color features for 40 glaucoma images and 118 healthy images.	140
5.27	Shows the difference means between the glaucoma and healthy RNFL coarseness feature.	143
5.28	Format of a confusion matrix	145
5.29	ROC curve: regions of a ROC graph	146
5.30	ROC curves: (a) an almost perfect classifier (b) a reasonable classifier (c) a poor classifier	146
5.31	Shows confusion matrix and ROC curve results from the shape selected features	148
5.32	Show confusion matrix and ROC curve results from the shape balanced features at 5 folds cross validation.	149
5.33	Show confusion matrix and ROC curve results from the shape balanced features at 10 folds cross validation.	149
5.34	Show confusion matrix and ROC curve results from the color selected features at 5 folds cross validation.	150
5.35	Show confusion matrix and ROC curve results from the color balanced features at 5 folds cross validation.	151
5.36	Show confusion matrix and ROC curve results from the color balanced features at 10 folds cross validation.	151
5.37	Show confusion matrix and ROC curve results from the texture selected features at 5folds cross validation.	152
5.38	Show confusion matrix and ROC curve results from the texture balanced features at 5 folds cross validation.	153
5.39	Show confusion matrix and ROC curve results from the texture balanced features at 10 folds cross validation.	153
5.40	Show confusion matrix and ROC curve results from the combined features at 5 folds cross validation.	154
5.41	Show confusion matrix and ROC curve results from the combined features at 10 folds cross validation.	155

5.42	Show confusion matrix and ROC curve results from the combined features applied to Drishti-GS database at 10 folds cross validation.	155
5.43	Show confusion matrix and ROC curve results from the combined features applied to RIM-ONE (version one) database at 10 folds cross validation.	156
5.44	Bar chart illustrate the different features applied for glaucoma detection.	157
5.45	Glaucoma CAD system	163

CHAPTER ONE
INTRODUCTION

1.1 Background

Glaucoma is dangerous an ocular disease because is the second leading cause of blindness with about 60 million glaucomatous cases globally in (Lim *et al.* 2010), and it is responsible for 5.2 million cases of blindness based on (Lim *et al.* 2012), with more than 90% of the patients unaware of the condition mentioned at (Zhang *et al*. 2014). In 2014, the World Health Organization (WHO) reported that 285 million people were estimated to be visually impaired worldwide: 39 million were blind and 246 had low vision, in which 80% of all visual impairment could be prevented or cured. The WHO also stated that around 90% of the world's visually impaired people lived in low-income settings at (Koprowski, 2014). Clinically, glaucoma is a chronic eye disease damage the optic nerve progressively as the disease progresses, more optic head damage due to loss of peripheral vision and a resultant in gradually vision loss. Finally the glaucoma is associated with total blindness. As the optic nerve damage is irreversible, glaucoma can be managed. However, treatment can prevent progression of the disease. Therefore, early detection of glaucoma is important to prevent from blindness.

Currently, there are three methods for detecting glaucoma: assessment of abnormal visual field, assessment of intraocular pressure (IOP) and assessment of optic nerve damage. Visual field problem is requires special equipment that is usually present only in hospitals because is a subjective examination as it assumes that patients fully understand the testing

instructions, cooperate and complete the test. Moreover, and the information obtained may not be reliable for kids or ICU patient.

In the second method a large proportion of glaucoma patients have normal level of IOP. Thus, IOP measurement is neither specific nor sensitive enough to be used for effective screening for early glaucoma. The assessment of optic nerve damage is the best to the other two methods (Zhang, Khow *et al.* 2012). Optic nerve can be assessed by trained specialists or through 3D imaging techniques such as Heidelberg Retinal Tomography (HRT) and Ocular Computing Tomography (OCT). However, optic nerve assessment by specialists is subjective and the availability of HRT and OCT equipment is limited due to the high cost involved. In summary, there is still no systematic and economic way of detecting glaucoma. There is a need for automatic and economic system for detection of glaucoma in accurate way, using the digital color fundus image (Figure 1.1) which is more cost effective imaging modality to assess optic nerve damage compared to HRT and OCT, and it has been widely used in recent years to diagnose various ocular diseases, including glaucoma and. In this research, a system for diagnosing glaucoma from non-glaucoma cases via fundus images analysis.

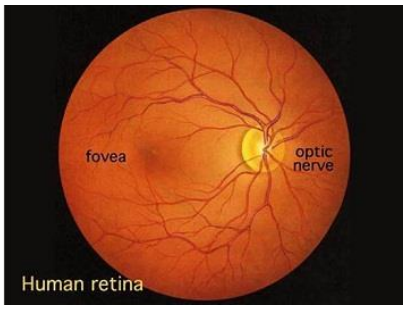

Figure [1.1]: Shows an example of fundus image obtained from fundus camera used for glaucoma detection (http://medical4help.blogspot.com/p/fundus-camera.html).

Therefore , If glaucoma diagnosed early enough, can be properly managed to prevent major loss of vision and most common causes of

permanent blindness worldwide, based on there is no cure for glaucoma, but medication can be used to prevent vision loss (Lim et al.2012). Following are six tests used to help detect glaucoma mentioned at www.biomedical-engineering-online.com.

1.1.1 Tonometry

Tonometry test used to measure the pressure inside the eye, also known as intraocular pressure (IOP). Having eye pressure higher than normal count as glaucoma risk factors but not mean a definite diagnosis of glaucoma.

1.1.2 Ophthalmoscopy

Ophthalmoscopy is device used to examine the inside part of the eye and can be performed on a dilated or undulated eye. The color, shape and overall health of the optic nerve is important signs in glaucoma diagnosis this can checked directly or by use a digital camera to photograph the optic nerve.

1.1.3 Gonioscopy

Gonioscopy is a test for examine the angle where the cornea meets the iris using a special mirrored device to gently touch the surface of the eye. Whether this angle is open or closed can show the doctor what type of glaucoma and how severe glaucoma may be.

1.1.4 Visual Field Testing

Visual field testing (perimetry) is a test that measures the patient vision. The patient will look straight ahead at a small light and will be asked to tell the examiner when he see a light flash stop to the side in the peripheral vision.

1.1.5 Nerve Fiber Analysis

Nerve fiber analysis is test for glaucoma in which the thickness of the nerve fiber layer is measured. Thinner areas may indicate damage caused by

glaucoma especially for patients who may be a glaucoma suspect and can be used to know if the glaucoma becoming worse.

1.1.6 Pachymetry

Pachymetry used to measure the thickness of the cornea because it reflect the influence the eye pressure. But research is still being conducted about the importance of corneal thickness in glaucoma testing.

1.2 Computer Aided Diagnosis

Computer Aided Diagnosis (CAD), the way to automate the detection process for glaucoma disease, which attracted extensive attention from clinicians and researchers. It not only alleviates the burden on the clinicians by providing an objective opinion with valuable insights, but also offers early detection and easy access for patients. By reviewed ocular CAD methodologies for various data types for each data type, and investigate the databases and the algorithms to detect different ocular diseases, found their advantages and shortcomings will analyze and discuss, and find three types of data (i.e., clinical, genetic and imaging) that have been commonly used in existing methods for CAD.

The recent developments in methods used in CAD of ocular diseases (such as Diabetic Retinopathy, Glaucoma, Age-related Macular Degeneration, and Pathological Myopia) are investigated and summarized, the CAD for glaucoma disease has shown big progress over the past years, the clinical importance of fully automatic CAD systems which are able to improve clinical knowledge and research sources (Zhang and Khow, 2012).

There have been surveys on retinal imaging in the area of ocular research (Abràmoff et al. 2010), (Bernardes et al. 2011). However, there are

still shortage in CAD systems for ocular disease diagnosis. This has motivated us to write a systemic method for CAD in glaucoma disease.

1.3 Problem of the Study

In the cases of glaucoma in which the visual field test result and IOP assessment are not reliable, at advanced AMD disease (Age-related Macular Degeneration). The visual field measurement is usually carried out using a static perimeter, which is difficult for different diseases e.g. advanced AMD, and it need patient corporation to follow the instruction and the IOP not sensitive because in some kind of glaucoma the pressure is normal which called normal tension glaucoma, the best way to detect glaucoma via ONH and imaging modality used for (OCT, HRT) are expensive. Then, it is necessary to search for other methods which will enable to determine the glaucoma disease. One such method is the analysis of digital fundus images of the eye fundus taken via fundus camera device.

Where studies indicate that radiologists do not detect all abnormalities on images that are visible on retrospective review, and they do not always correctly characterize abnormalities that are found. In the clinical interpretation of medical images, limitations in the human eye-brain visual system, reader fatigue, distraction, the presence of overlapping structures that camouflage disease in images, and the vast number of normal cases seen in screening programs provide cause for detection and interpretation errors as at (Adrian et al. 2012). For the previous reasons of human mistakes, other diseases affect in glaucoma diagnosing and founded devices are expensive (OCT, HRT) there is a need to determine the severity of glaucoma, mainly on the basis of optic nerve head (ONH) and retinal nerve fiber layer (RNFL) in the digital fundus image structure to develop a reliable automated computer-

aided diagnosis system (CAD) for detecting glaucoma capable of analyzing changes in both, ONH and RNFL in glaucoma. Like (Zhou *et al*. 2012), who investigated the use of MRMR-based Feature Selection in automatic Glaucoma diagnosis the featured used from heterogeneous data sources, i.e., retinal image and eye screening data to improve and facilitate a better understanding of the CAD system and data collection for glaucoma research.

1.4 Objectives

In this research, a review on the current approaches for automatic glaucoma detection is presented, and new features for detect glaucoma in fundus images are proposed, the recommended methods of diagnosis, challenges, and the existing automated methods will be surveyed. Based on recent successful machine learning techniques and Ophthalmologists observation, the new learning-based technique for glaucoma detection are investigated and proposed. The RIM-ONE database will be used to evaluate the accuracy of the proposed methods.

1.4.1 General Aim

The general aim of this project is to develop a reliable automated computer-aided diagnosis system (CAD) for detecting glaucoma and develop an algorithm that detects optic disc and optic cup.

1.4.2 Specific Objectives

1. Choose the best subset of features that describes the optic nerve and detect the glaucoma disease.
2. Assess the accuracy, sensitivity, and specificity of the classifier.

1.5 Research Methodology

This thesis presents a detection strategy motivated by the evaluation guidelines used by ophthalmologists for the diagnosis of glaucoma. The proposed strategy can be seen as an approach of integrating multiple features gathered from the analysis of optic disc, cup, and RNFL indicators from retinal fundus images. The analysis part consists of quantification of changes happened in OD, OC and RNFL.

The resultant parameters of the analysis components encode information to detect the glaucoma disease from the obtained features along with the differences between glaucoma and healthy images. The final decision on the presence of glaucoma is made by classification these features and evaluate the results compared with the ground truth. Figure [1.2] illustrates the proposed detection approach for detecting glaucoma in digital fundus images based on employing many of the publicly available image datasets with diagnosing and segmentations ground truth. The chosen datasets act as a base in order to provide robust evaluations and consistent.

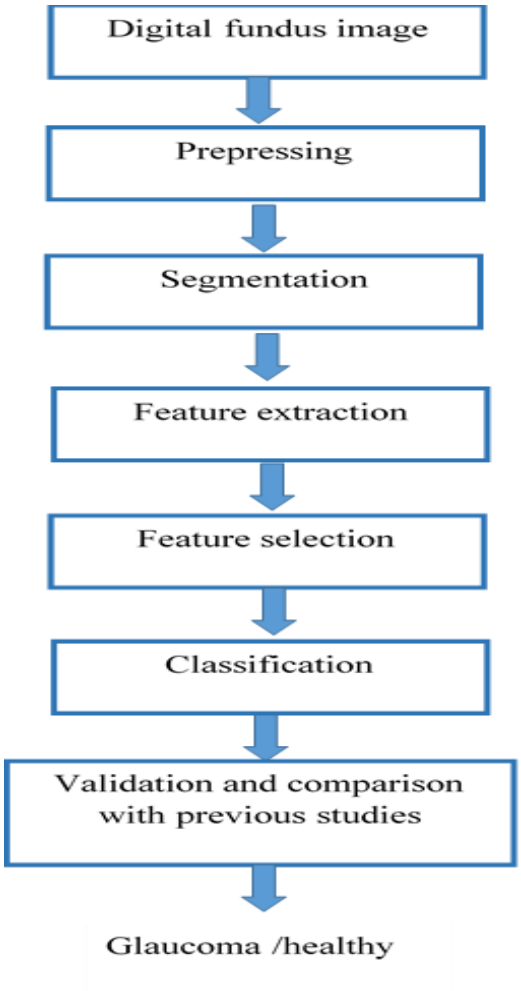

Figure [1.2]: Shows the proposed algorithm approach for detecting glaucoma in digital fundus images

1.6 Significance of the Study

- This study provides an expert system for real-time fundus image analysis, which gives the radiologists an opportunity to improve their image interpretation. The proposed system will improve the diagnosis of glaucoma and therefore, it will minimize the miss detection rate and help in early diagnosis and treatment, which can significantly improve the chance of managing the glaucoma disease. The diagnosis results and images can be stored in a digital format (an image file for the retina

photo and a medical report) use to generate a diagnoses database useful for researchers, for medical practice and for patient follow up.

- A database with patient personal and care information can be developed with a secured password. The long treatment costs, the supplementary tests and the founded images will help the doctors in follow up the patient. The quality and accessibility of eye medical services will increase.
- Finally, an accurate, novel automated technique for glaucoma detection will be designed to reduce the workload of ophthalmologists, checking the disease progression, easy to operate, and inexpensive, thus, once glaucoma is correctly diagnosed then they can take proper medicine or undergo surgery in a timely manner to prevent permanent blindness.

1.7 Contributions

The contributions of this thesis come from the novel digital fundus image analysis solutions developed for different glaucoma indicators are summarized here:

An automatic CAD system for glaucoma detection with high accuracy is developed, through that:

1. The optic disc segmentation algorithm is modified by circle reconstruction approach is used to improve the thresholding model and extended to the optic cup segmentation.
2. An algorithm is developed to detect Cup and disc color, shape features and RNFL texture features.
3. The performance of the proposed algorithms is presented. Cup, disc and RNFL features are evaluated on several databases for glaucoma

diagnosis. A more powerful algorithm will use, classification accuracy may further be improved.

4. New features set will use to describe the disease.

1.8 Organization of the book chapters

The outline of the thesis are in chapter two, a brief review of medical background is presented, followed by a theoretical and mathematical background used in fundus image processing. Chapter three, literature review about segmentation and feature extraction, Chapter four, the formulation of the proposed methodology. And Chapter five, the results of optic disc and optic cup segmentation algorithm is presented, the feature extraction and selection method experimental results and performance evaluations of the classifier are given, Chapter six**,** the conclusions and discussion.

CHAPTER TWO
MEDICAL BACKGROUND

2.1 Introduction

This chapter will cover the medical background of the glaucoma disease. The human eye, the image acquisition of the retina, medical overview of the glaucoma disease and retinal image assessment, the digital image processing techniques and mathematical background.

2.2 The Human Eye

Human eye, in humans, specialized sense organ capable of receiving visual images, which are then carried to the brain shown in Figure [2.1], from, (www.shutterstock.com) and provides the capability to see color, detect motion, identify shapes, gauge distance and speed, judge the size of faraway objects, see in three dimensions even though images fall into two dimensions (Ali Allam, 2017).

2.2.1 Structure of the Human Eye

The human eye in Figure [2.1], is a complex structure, where light passes through the cornea and a transparent crystalline lens, which assists in focusing

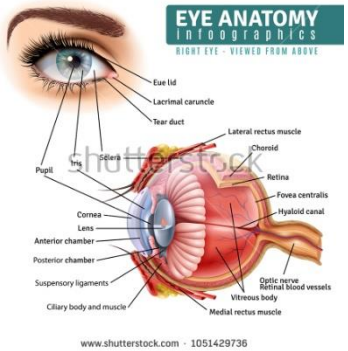

Figure [2.1]: Shows the Human Eye inside and outside structure, www.shutterstock.com

Light, onto the retina through the pupil. The amount of light which enters the eye is controlled by the iris, which has the ability to enlarge or contract, while the lens converges the incoming light rays to a sharp focusing point onto the retina by lengthening and shortening its width. The retina, situated at the back of the eye, is approximately 0.5 mm thick, figures [2.2a]. In the center of the retina is the optic nerve, an oval white area measuring about 2mm (height) ×1.5mm (width) across. At approximately (4.5-5mm), or 2.5 disc diameters away from the optic nerve, lies a blood vessel-free reddish region, known as the fovea, Figure [2.2b]. The center of the fovea is also called the macula.

The retina is a multi-layered sensory tissue that lies on the back of the eye, contains millions of photoreceptors that capture light rays and convert them into electrical impulses will convert to images in the brain. The main photoreceptors in the retina are rods and cones. Rod cells are very sensitive to changes in contrast even at low light levels, hence able to detect movement, but they are imprecise and insensitive to color located in the periphery of the retina and used for scotopic vision (night vision). Cones are high precision cells capable of detecting colors, which concentrated in the macula, the area responsible for photopic vision (day vision). The very central portion of the macula is called the fovea, which is where the human eye is able to best distinguish visual details and the loss of peripheral vision may damage to the macula and result in loss of central vision.

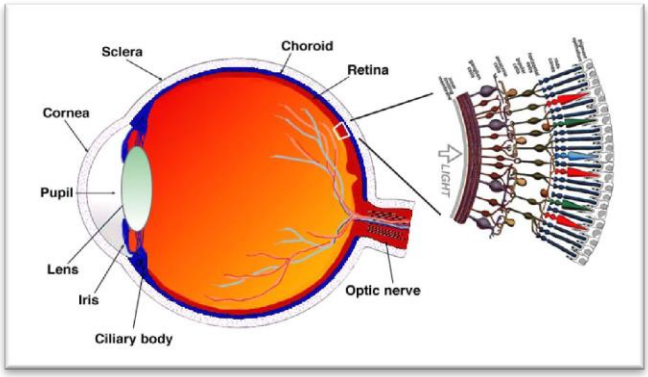

(a)

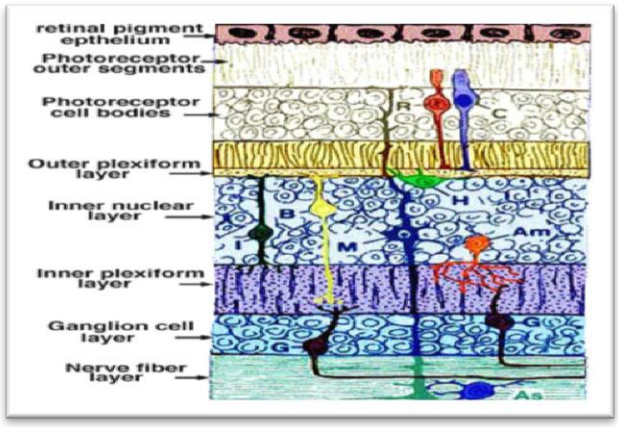

(b)

Figure [2.2]: Shows anatomy and schematic diagram of the human eye (a) Sagittal view of the human eye with a schematic enlargement of the Retina, (b) Schema of the layers of the developing retina (eye source: webvision.med.utah.edu).

The optic nerve on the retina is also called the blind spot as it is insensitive to light. Often, the fovea, optic nerve. Retina and retinal vasculature are referred to as the ocular fundus structures.

2.3 Image Acquisition of the Retina

2.3.1 Fundus Image Capture

A color digital retinal fundus camera is widely used to capture the retina. The fundus camera is wide use and complex optical imaging device with a low power microscope and an attached camera, the general working principle described below is based on the overview provided in (Tyler *et al.* 2014).

The interior surface of the eye (i.e. retina, vasculature, optic disc, and macula) is captured using a specialized low-power microscope with an attached camera. Moreover, in stereo fundus photography, image intensities represent the amount of reflected light from two or more different view angles for depth resolution.

Light is first generated from either viewing lamp or the electronic ash and is passed through a set of filters, mirrors and a series of lenses for focusing. A mask on the uppermost lens is then used to shape the light into a doughnut. Based on the Gullstrand and principle, the ring of light is projected on the cornea, through the pupil. The resulting retinal image then leaves the cornea through the unilluminated portion of the doughnut, this space within the ring allows a separation of both the incoming and outgoing illumination. The outgoing light continues through the central aperture of the mirror, through the astigmatic correction device and the diopter compensation lenses, and then back to the single lens reflex camera system.

Clinically, this camera is used by ophthalmologists $45°$ and trained medical professionals to monitor and discover evidence of ocular abnormalities for immediate feedback, diagnosis, and treatment of retinal

diseases. The fundus photographs are then kept as visual records to document the ophthalmoscope appearance of a patient's retina.

In the market, fundus cameras are described by their angle of coverage. This is derived from the optical angle of acceptance of the fundus camera lens and can range between 20°, to 140°. A 30° considered the normal angle of view, creates a film image with a magnification of $2.5x$, but wide-angle fundus cameras capture images between 45° and 140° with less retinal magnification. Capturing the retinal fundus photographs can be with a dilated or non-dilated pupil. The main advantage of dilation is to allow better view and image capture of the retina. However, even with dilation, the quality of the fundus image can still be affected by additional difficulties such as the media opacity due to cataracts. Non-mydriatic retinal fundus cameras allow digital photographs of the eye to be captured through a small pupil size (in between 2.0 to 4.0 mm) without the need and discomfort of pupil dilation.

2.3.2 Other Imaging Devices

i. Fluorescein Angiography (FA): Indo-cyanine Green Angiography (ICG): shown in Figure [2.3], a grayscale image is produced where the blood flow within both, the retina and the choroid, is captured by injecting fluorescein dye and indo-cyanine dye, respectively, in the blood vein.

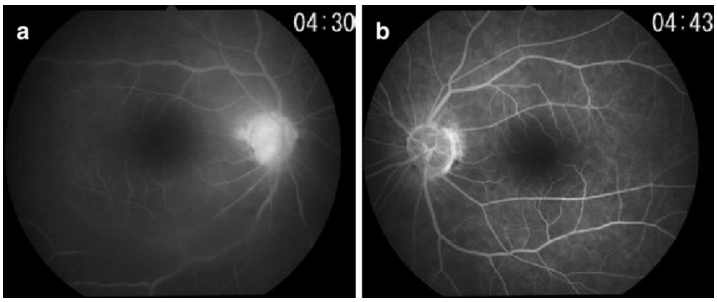

Figure [2.3]: Shows images produced via angiography as a type from the fundus image (Mauricio Maia *et al.*2017).

ii. Fundus Auto Fluorescence (FAF): Shown in Figure [2.4], the retina is illuminated with blue light which causes certain cellular components to glow without injecting any dye in the blood veins.

Figure [2.4]: Shows images produced via Fundus Auto Fluorescence device as a type from the fundus image (Retina Image Bank).

iii. Confocal Scanning Laser Ophthalmoscopy (CSLO): commercially, this imaging modality is known as Heidelberg Retina Tomography (HRT). Shown in Figure [2.5], it uses a special laser beam that is focused on the surface of the optic nerve in order to precisely capture a 3D image of the optic disc and the surrounding retina. HRT is a powerful diagnostic tool for glaucoma in particular.

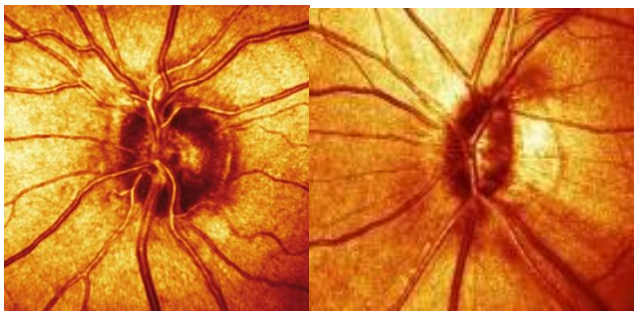

Figure [2.5]: Shows images produced via Heidelberg Retina Tomography as a type from the fundus image (Heidelberg engineering, 2017).

iv. Optical Coherence Tomography (OCT): Shown in Figure [2.6], Precisely, OCT is not literally considered a “fundus imaging” modality, as it is analogous to ultrasound except that it utilizes light instead of sound. OCT scan is used to capture the thickness of the retinal tissue by measuring the flight

time of the originated backscatter. Thereby, it is well suited to monitor pathological conditions such as macular edema which leads to the swelling or thickening of the macula, a summarized comparison table of retinal acquisition devices is shown in Table. 2.1.

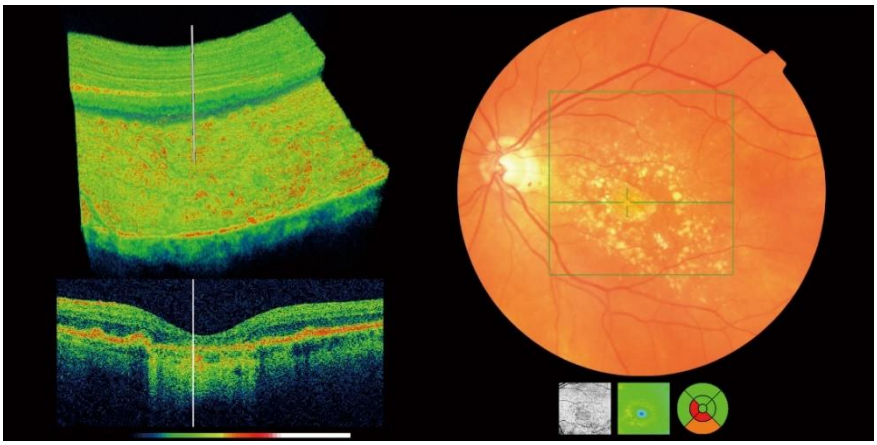

Figure [2.6]: Shows images produced via Optical Coherence Tomography, can used to detect glaucoma (OCT, 2017)

Table (2.1): Overview comparison of retinal acquisition devices, used to capture the retina and detect glaucoma to illustrate the reason to choose the digital fundus camera in this research.

Devices	Advantages	Limitations
Fundus camera	Stable technology. True color of retina. Low cost and widespread use.	Does not capture RNFL layer thickness or information.
GDx nerve fiber analyzer	Provide thickness of nerve fiber layer, which is important in glaucoma diagnosis.	Affected by existing eye condition.
Heidelberg Retinal Tomography (HRT)	Provide topographic (layer thickness) image of optic nerve.	Topographic image is an approximate representation.
Optical Coherence Tomography(OCT)	Multiple cross-sectional (A-scan) of retina. Cross-sectional Tomograph (B-scan). Sub-layer retinal tissue thickness, which is important in glaucoma diagnosis.	Results change with new generation device and do not compatible. High cost.

In addition, OCT machines are unable to provide progression analysis as there is no means to measure the same tissue during follow-up exams. Digital fundus images, on the other hand, provides the advantages of full color which helps to distinguish between cupping and pallor, has a stable technology and widespread usage for community-level screening (Cello *et al*. 2000). Furthermore, the record of a digital retinal photograph will not go out of date and is often used as a baseline for clinical evaluation and comparison. This makes it the ideal media to use for glaucoma disease screening purposes.

This section will cover an overview of the medical aspects of glaucoma and the structural changes it brings to the retina as it progresses (Bourne *et al*.2016).

2.4 The Glaucoma Disease

Glaucoma is a collection of optic neuropathies. It is a chronic disease that has various types the most common type is the open-angle glaucoma. It is differentiated from ACG by the appearance of the iridocorneal angle. In the OAG, the iridocorneal angle is open having a normal form. On the other hand, the iridocorneal angle is closed in ACG. Glaucoma is further divided into primary and secondary. Primary glaucoma is characterized by the absence of additional ocular/systemic impairments. Regardless of the common features between primary and secondary glaucoma, secondary glaucoma might proceed differently. In addition, secondary glaucoma is accompanied by ocular/systemic diseases which could lead to the initiation of glaucoma.

The number of glaucoma patients due to the two most widely spread types of glaucoma which are OAG and ACG adds up to 60.5 million people in 2010. OAG percentage is 74% (44.7) while ACG causes the remaining 26% (15.7) glaucoma

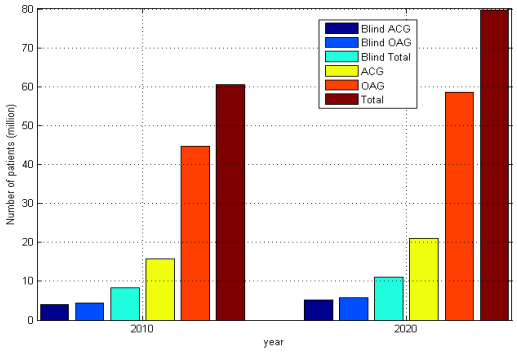

Figure [2.7]: The distribution of open angle glaucoma (OAG) and angle closure glaucoma (ACG) in the year 2010 and 2020 according to the estimation in (Quigley and Broman, 2006).

The number of people with bilateral blindness is shown for the total and the individual glaucoma types. The glaucomatous bilateral blindness is estimated to be 8.4 with 4.5 and 3.9 million people by OAG and ACG respectively. The epidemiology of glaucoma is expected to rise significantly in 2020 to 79.6 million people among the mare 11.2 million blind people. OAG contributes with 5.9 million vision loss cases (from 58.6 million) and the ACG share is increased to 5.3 vision loss cases (from 21million). The glaucoma distribution numbers are based on the work by (Quigley, 1999). The various entities of glaucoma have common characteristics that are used to identify the presence of the disease. Defects in the visual field, excavation of the optic disc, and optic nerve degeneration. IOP is a highly relevant feature of glaucoma. However, 50% of people diagnosed with OAG do not have ocular hypertension (Sommer *et al.* 1991), (Deepikaa *et al.*2016).

Moreover, another type of OAG is the NTG where the IOP of the patients is always in the normal range. Nevertheless, reducing the IOP level has shown to delay or stop the progression of glaucoma even in NTG, Despite the attempts aiming to provide a precise definition of glaucoma like the case

definition in (Foster *et al*. 2002), the mechanisms of glaucoma are not completely understood and there are many challenges ahead of the scientific community to understand the pathology of glaucoma. Furthermore, it is argued that, due to the complex nature of glaucoma, all the aforementioned characteristics do not provide a clear identification for glaucoma and still patients could be wrongly diagnosed with glaucoma or glaucoma could go undetected (Kroese and Burton, 2003).

2.4.1 Glaucoma and the Visual Pathway

The functional and morphological disorders due to glaucoma at the eye level have been extensively studied. However, the pathogenesis of glaucoma indicates the potential of extending the impairment to the rest of the visual system (Gupta and Yucel, 2007), like spreading atrophy along the visual pathway. This includes the intracranial optic nerve, lateral geniculate nucleus and visual cortex (Gupta *et al.* 2006). The rapid development of neuroimaging techniques during the last decades allowed the identification of the human visual system in-vivo and non-invasively. This was utilized in recent studies examining glaucoma. The optic radiation was examined in glaucoma patients and the neuronal density was reported to be decreased a using size attenuation compared to normal subjects (Engelhorn *et al*. 2011). A study produced glaucoma artificially in rats and found correlation between parameters indicating the cerebral optic nerve fibers disorder and glaucoma (Huajun *et al.* 2007), (Garaci *et al.* 2009) evaluated the integrity of the white matter fibers and axonal structure of the optic nerve and the optic radiation in the presence of glaucoma. The fibers were compromised and the degree of degeneration in the optic nerve was found to be in correlation to the glaucoma severity (Garaci *et al.* 2009).

2.5 Glaucoma Diagnosis

The glaucoma clinical examination has a wide variety of modalities that contribute to the identification of the disease. This variation of modalities arises from the complex nature of the glaucoma pathology where no single modality can provide a definite decision. For example, measuring the IOP as a major risk factor for glaucoma is not sufficient because its increase could be due to other diseases. The examination relies on evaluating the major glaucoma features which are the visual function and the optic disc appearance. In addition, ocular hypertension is an important indicator of the likelihood of having glaucoma and a determining factor for its progression path.

2.5.1 Optic Nerve Head:

Fundus cameras take photographs of the interior surface of the eye detailing the vessel tree and the optic disc among other structure. Digital fundus image scan be used to detect the excavation of the optic disc and the reduction of the rim area which are significant signs of glaucoma. One of the most important parameters for glaucoma diagnosis is the cup to disc ratio. Two example fundus images of normal and glaucoma subjects are shown in Figure [2.8]. The rim thinning can be observed for the glaucoma case in Figure [2.9]. Despite that fundus images are two-dimensional images, acquiring stereo images can provide three-dimensional information (Nave *et al*. 2007). Heidelberg retina Tomograph (Heidelberg Engineering, Heidelberg, Germany) utilizes the principals of confocal scanning laser ophthalmic copy to provide information about the topography of the retina surface. The topography is obtained by imaging sections of the retina which are used to reconstruct a three-dimensional view of the ONH. This allows for better representation and quantification of the optic disc. Glaucoma relevant

variables are extracted using HRT such as horizontal and vertical cup-to-disc ratio, volume of cup and rim, and average RNFL thickness. The HRT parameters were shown to be sensitive for glaucoma diagnosis (Ferreras, 2008). In Figure [2.9] an HRT acquisitions of normal and glaucoma subjects are demonstrated. Glaucomatous signs can be observed in the glaucoma patient. Optical coherence tomography relies on measuring an interference pattern from a reference light following and a light reflected from the retina. The light used can penetrate the retinal layers providing depth information. The reflected light depends on the tissue structure and, thus, the components of the retina can be separated using OCT. Two-dimensional and three-dimensional images of the retina is obtained by combining depth scans. RNFL is segmented on OCT images as shown in Figure [2.10].The thickness of the RNFL demonstrated high ability to screen glaucoma in its early stages **(**Bowd *et al*. 2001), (Nouri and Mahdavi, 2004**)**

2.5.2 Intraocular Pressure:

The instrument used for measuring the IOP is called the tonometer. Different techniques are utilized for tonometry. The main idea behind application tonometry, the most common type of tonometry, is to directly apply a force to flatten a region on the cornea. The force required is related to the ocular pressure. This method is relatively accurate and widely integrated in the clinical flow. A less precise variation of this technique is the non-contact tonometry which is usually used for screening purposes. In this procedure, the corneal curvature is reduced by the application of an air pulse and similarly the force is measured. In addition to identifying ocular hypertension risk, tonometry can be used to evaluate the glaucoma treatment and its effect on the IOP.

2.5.3 Visual Field Function

The glaucomatous vision defects are located on the periphery of the visual field in its early stages. Perimetry is a widely used technique to examine the visual field. It detects the sensitivity of the eyes to identify light spots on a back ground at various positions in the visual field, to screen early glaucoma patients and to diagnose moderate and advanced glaucoma by capturing the functional loss in vision (Cello et al. 2000). Sample suggested the incorporation of more than one functional test to enhance the glaucoma diagnosis (Sample et al. 2000). Moreover, they pointed out that the structural ONH damage as shown in Figure [2.11], Figure [2.12] and Figure [2.13]: and the functional impairment due to glaucoma have no definite precedence. i.e., in some glaucoma cases visual function loss could be detected before optic disc abnormalities and in other cases the sequence is reversed.

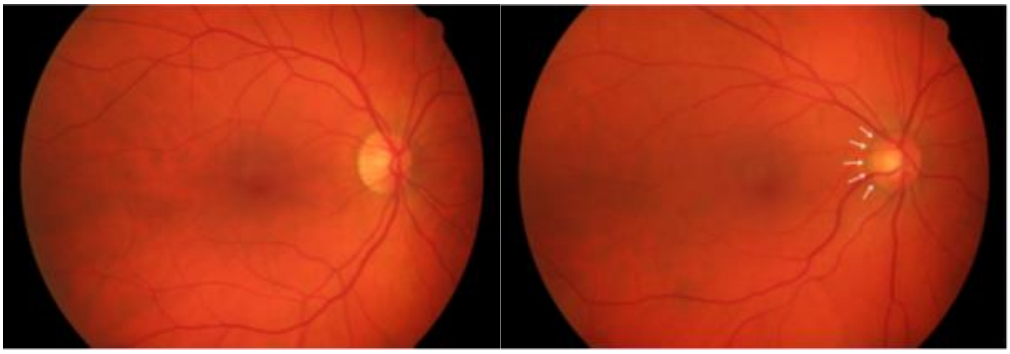

(a)Normal (b) Glaucoma

Figure [2.8]: Fundus images showing the background of the retina for a healthy subject (a) and a glaucoma (b) patient. (Nave *et al.* 2007).

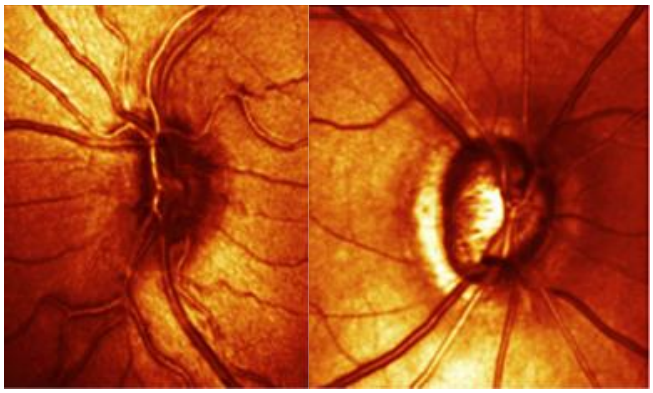

(a)Normal (b) Glaucoma

Figure [2.9]: Two sample HRT-II images for a healthy subject (a) and a glaucoma (b) patient. The glaucomatous cupping is present in the optic nerve head (Heidelberg engineering, 2017).

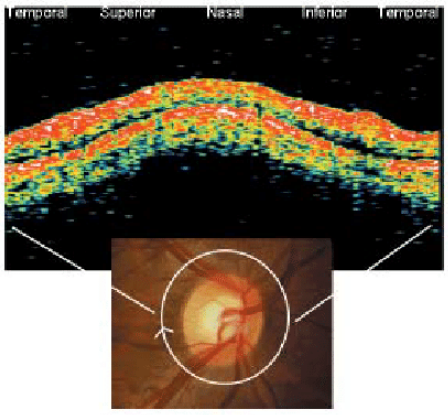

Figure [2.10]: An example of a circular optical coherence tomography (OCT) scan around the optic disc to view the RNFL (Sek-Tien Hoh, 2007).

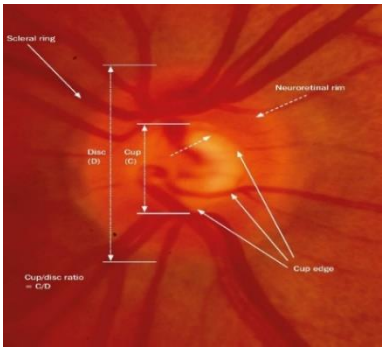

Figure [2.11]: Anatomy of the Optic Nerve Head - Clinical features of the optic nerve (Community eye health, 2017).

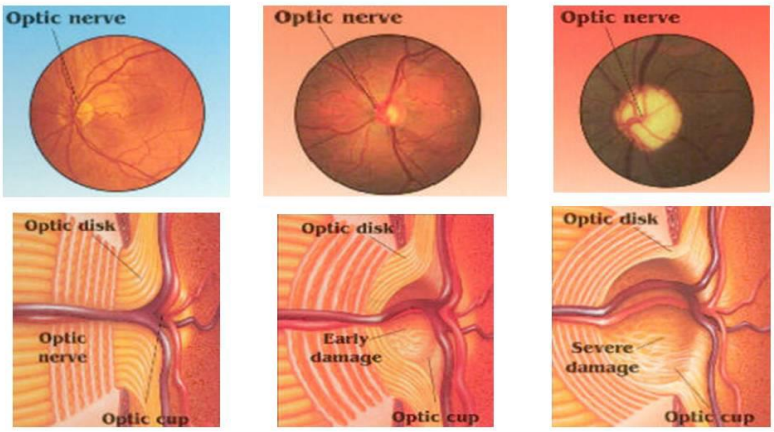

Figure [2.12]: Progression of OC Enlargement Changes in Glaucoma (Left) a normal ONH. (Centre) Early glaucoma ONH. (Right) Advanced glaucoma ONH. Image from Bay Eyes Cataract& Laser Center (Jonas and Budde, 1999).

(a) (b)

Figure [2.13]: Shows (a) Vision with normal eye (b) Vision with abnormal eye (Eye diseases, 2017).

2.5.4 Glaucoma Assessment

Eye doctors usually use several tests to detect glaucoma. These are usually categorized as functional or image-based assessment. Functional assessment includes measurement of IOP (tonometry) and visual field examination. Image-based evaluation relies on optic nerve head imaging devices to determine optic nerve head structural damage or thinning of the

retinal nerve fiber layer (RNFL). Examples of such imaging devices are Retinal Fundus Camera, Heidelberg Retinal Tomography (HRT) and Optical Coherence Tomography (OCT). Nonetheless, most of these methods have their own limitations. Measurement of IOP was reported to have the poor sensitivity of around 50% (Sommer *et al*. 1991). This is partially due to cases of normal tension glaucoma, where patients have a condition in which optic nerve damage and vision loss have developed even with a normal pressure inside the eye. The visual field examination is often time-consuming and found to be unreliable due to factors such as patient's fatigue and learning effects. Image-based evaluation using HRT and OCT are highly costly and are usually only available at tertiary hospitals, thus limiting its outreach.

On the other hand, retinal fundus cameras are commonly found and used at primary are for assessment of the retinal and optic nerve. Unlike IOP, the appearance of the optic nerve does not actuate from day to day, and unlike visual field tests, it is not dependent on patient co-operation, http://www.optic-disc.org/tutorials/glaucoma_evaluation_basics/page13.html.

In addition, compared to functional assessment, direct inspection of the optic disc seems to have the highest accuracy. The study in (Fernandez-Granero *et al*. 2017) also showed in particular that Cup-to-Disc Ratio (CDR), Figure 2.14, is an important parameter for glaucoma detection. It is an important clinical indicator of glaucoma (Damms and Dannheim, 1993), and measures the ratio between the vertical heights of the optic cup against the vertical optic disc height. Currently, CDR assessment is performed manually by the ophthalmologists to gauge and monitor optic cupping size and degeneration of the optic nerve head in glaucoma. In this thesis, the objective

is to design algorithm approaches to directly assess the optic nerve changes in retinal fundus images.

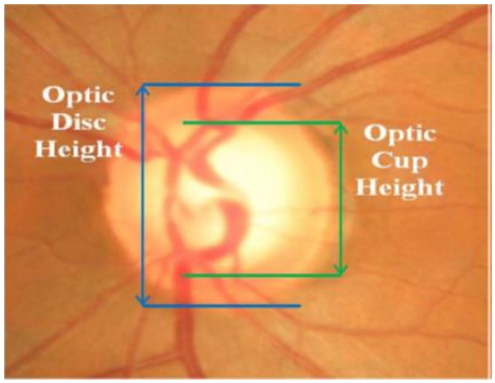

Figure [2.14]: CDR The vertical cup-to-disc ratio is used as clinical measure in assessing glaucoma (Damms and Dannheim, 1993),

2.5.5 Glaucoma ONH Evaluation

Digital color fundus images is a popular imaging modality to diagnose glaucoma. A number of features can be extracted from digital fundus images to measure the damage of the optic nerve (ONH) duo to glaucoma disease. Commonly used imaging risk factors to diagnose glaucoma include optic cup-to-disc ratio, parapapillary atrophy, disc hemorrhage, neuroretinal rim notching, neuroretinal rim thinning, inter-eye asymmetry and retinal fiber layer defect (Monica *et al*.2013).

2.5.5.1 Cup-to-Disc Ratio

Optic disc cupping is one of the most important signs of glaucoma (Damms and Dannheim, 1993). It happened due to cup enlargement and defined as the ratio of the cup diameter over the disc diameter. The optic disc (OD has an orange-pink rim with a pale center called the optic cup, which is a neural retinal tissue and normally white in color.

With more glaucoma progression more optic nerve fibers die, the OC becomes larger with respect to the OD which corresponds to an increased CDR value. For a healthy subject, the CDR value around 0.2 to 0.3. The CDR test applied on the retinal fundus images and getting the more accurate result in glaucoma diagnosis (Dnyaneshwari *et al*.2014), Figure 2.15 show measurement of CDR and the difference of a normal and a glaucomatous optic nerve. CDR can be measured manually by marking the optic disc and optic cup boundaries. However, this method is quite subjective and largely dependent on the experience and expertise of the ophthalmologists and both time consuming and depend on to inter-observer variability. Thus, an automatic CDR measurement system is highly desirable.

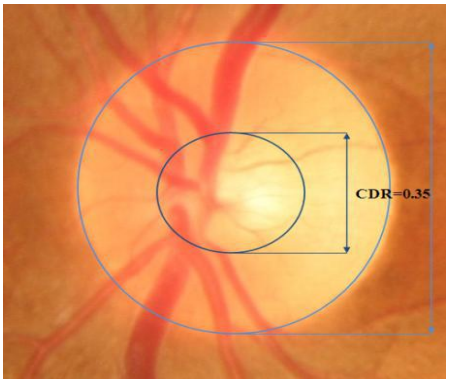

Figure [2.15]: Measurement of cup to disc ratio (CDR) on fundus image, used as indicator of glaucoma big CDR suspected of having glaucoma (Dnyaneshwari *et al*. 2014),

2.5.5.2Parapapillary Atrophy

Parapapillary atrophy (PPA) is another important risk factor that is associated with glaucoma (Jonas *et al*. 1992). PPA is the degeneration of the retinal pigment epithelial layer, photoreceptors and, in some situations, the underlying choroid capillaries in the region surrounding the optic nerve head.

PPA can be classified as an alpha type and beta type. Alpha PPA occurs within the outer or alpha zone and is characterized by hyper or hypo-pigmentation of the retinal pigment epithelium. Beta PPA occurs within the inner or beta zone, which is the area immediately adjacent to the optic disc and is characterized by visible sclera and choroid vessels. PPA occurs more frequently in glaucomatous eyes, and the extent of beta PPA correlates with the extent of glaucomatous damage, particularly in patients with normal tension glaucoma (Uchida *et al.*1998). The development of PPA can be classified into four stages: no PPA, mild PPA, moderate PPA and extensive PPA. Figure [2.16] shows how these different stages of PPA look like on fundus images.

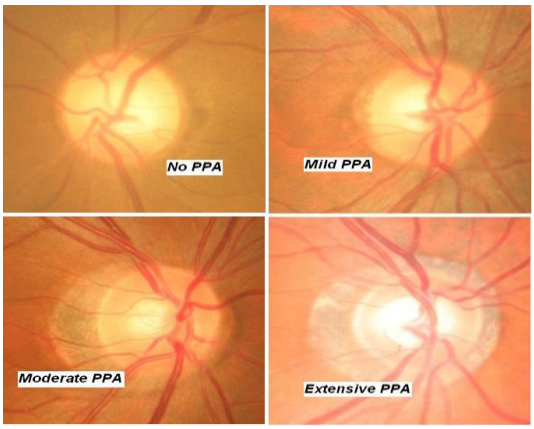

Figure [2.16]: Grading of PPA according to scale, occurs more frequently in glaucomatous eye (Uchida *et al.*1998).

2.5.5.3 Disc Hemorrhage

Disc hemorrhage is a clinical sign that is often associated with optic nerve damage. Disc hemorrhage is detected in about 4% to 7% of eyes with glaucoma and is rarely observed in normal eyes. The hemorrhage is usually dot-shaped when within the neuroretinal rim and flame-shaped when on or close to the disc margin. Flame-shaped hemorrhages within the retinal nerve

fiber layer that cross the sclera ring are highly suggestive of progressive optic nerve damage. Disc hemorrhages are most commonly found in the early stages of normal tension glaucoma, usually located in the inferior or superior temporal disc regions as shown in Figure 2.17. They are usually visible for 1 to 12 weeks after the initial bleeding. At the same time, a localized retinal nerve fiber layer defect or neuroretinal rim notch may be detected, which corresponds to a visual field defect.

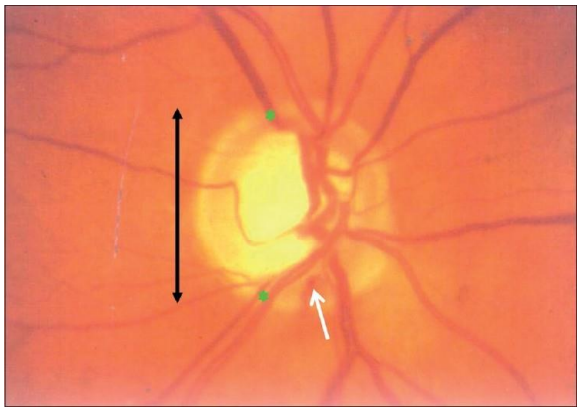

Figure [2.17]: Disc hemorrhage in the inferior temporal side indicate to glaucoma (Ravi *et al.*2011).

2.5.5.4 Notching

Neuroretinal rim notching, also known as focal enlargement of the optic cup, is focal thinning of the rim which is a structural damage of glaucomatous optic disc (Allingham, 2005). Disc hemorrhage and RNFL damage often develop at the edge of the focal notching. Thus, it is the hallmark of glaucomatous optic disc damages, and its presence is considered to be practically pathognomonic. Figure 2.18 shows the difference of subject with focal notching and a healthy optic nerve.

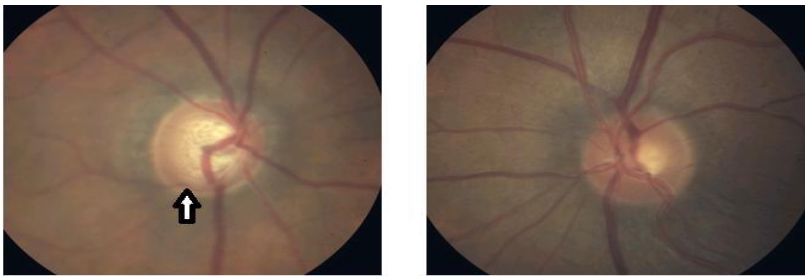

Figure [2.18]: Shows an example of focal notching of the rim, Left:the notch at 7 o'clock, which is an indicator of glaucoma, Right: healthy disc. (Allingham, 2005).

2.5.5.5 Neuroretinal Rim Thinning

The neuroretinal rim thinning associated with the loss occurs in a four sectors, firstly at the inferior temporal disc sector and the nasal superior sector as the last to be affected (Harizman *et al.* 2006), (Jonas *et al*.1993). The measurement of the neuroretinal rim loss is essential for glaucoma detection and also complement to the PPA detection as the site of the largest area of atrophy tends to correspond with the part of the disc with the most rim loss (Kotecha, 2002). Figure 2.19 shows the rim widths in different sectors of the optic disc.

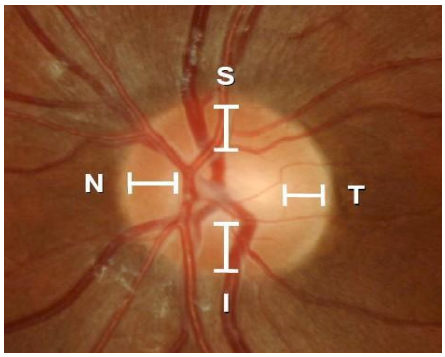

Figure [2.19]: Shows rim widths in the inferior, superior, nasal and temporal sectors, also indicators to the glaucoma disease based on ISNT rule (Kotecha, 2002).

2.5.5.6 Inter-eye Asymmetry

Inter-eye asymmetry of optic disc cupping as Figure [2.20] is useful in glaucoma detection, because one eye is usually worse than the other in glaucomatous patients. In contrast, only about 3 % of normal individuals have such asymmetry. Thus, inter-eye optic disc cupping asymmetry is a good sign of glaucoma.

Figure [2.20]: Shows an example of inter-eye asymmetry of optic disc cupping. Left: the eye with small CDR. Right: the eye with large CDR, where a big CDR usually considered to be a significant asymmetry and indicator of glaucoma.

2.5.5.7 Retinal Nerve Fiber Layer Defect

The RNFL appears as bright fiber bundle striations which are unevenly distributed in normal eyes. The fiber bundles can be most easily observed in the inferior temporal sector, followed by the superior-temporal sector, the superior-nasal sector and finally the inferior-nasal sector. They are rarely visible in the temporal and nasal regions. RNFL defects are associated with visual field defects in corresponding hemifield. When RNFL defect exists, there would be dark areas in the bright striations on the fundus image. The RNFL defects are usually wedge-shaped and are commonly seen in both hypertension and normal pressure glaucoma. Figure [2.21] shows examples of the RNFL defect.

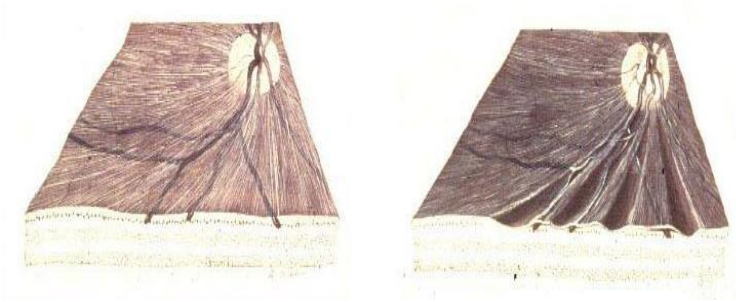

(a) (b)

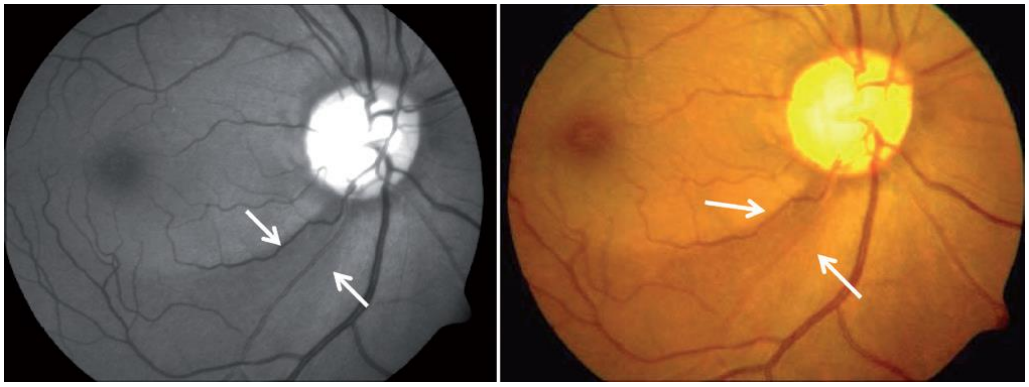

(c) (d)

Figure [2.21]: show an examples of RNFL defect. (a): cross section view of normal RNFL. (b): cross section view of RNFL defect. (c): normal RNFL in fundus image. (d): RNFL defect in fundus image, defect RNFL significant indicator for glaucoma (Ravi *et al.*2011)

2.6 Motivation of Fundus Image Processing

A color retinal fundus camera is widely used to photograph the retina, which contain the main glaucoma risk factors like CDR, rim, PPA and ISNT rule, all these factors appear at optic nerve head and it is surrounded area. In addition, fundus camera is stable technology, true color of the retina, low cost and widespread use.

2.6.1 Digital Fundus Image Processing

The mathematical background for digital fundus image processing will be explained in three main steps:

Step (1) – Preprocessing: Image Enhancement.

Step (2) – Processing: Image Segmentation.

Step (3) – Post-Processing: Features Extraction and Selection.

Software packages such as MATLAB®, provide powerful means for implementing these image processing functions. The following part overviews the main image processing functions that can be used for the enhancement and segmentation of images, which will be used later in at chapter 4 within the context of the methodology.

Step (1) – Preprocessing: Image Enhancement

Image enhancement is the basic process of changing a raw image so that the result would be more suitable than the original for a specific application or further processing (Gonzalez, 2008). Below are some of the major enhancements that can be applied to the fundus image either solely or combined together with one another.

Color image processing: since the captured digital fundus image is a full-color image, it is obvious that color image processing techniques are strongly needed. For example, color splitting can be used to view and process each of the red, green, blue channels independently from one another (Dougherty, 2009). Also, conversion between the (RGB) and (HIS, HSV) color models are very useful in many situations; unlike the RGB color space, HSI, HSV, and Lab models decouple the color (chromaticity) and gray-scale (intensity) information, HSI and HSV represent the intensity within the (I) and (V) layers, respectively, while chromaticity is represented within both the Hue (H)

and Saturation (S) layers. As for the $L * a * b$ color space, the L* represents the luminosity (intensity), while the $a * and\ b *$ layers represent the chromaticity.

2.6.2 Channel Separation:

Color digital fundus images are made of pixels are combinations of the primary colors. The separated channel is the grayscale image of the same size as a color image, made of just one of these primary colors. For instance, the colored image have a red, green and blue channel and the channel extraction is important feature to extract some information can used in the image processing (Gonzalez and Woods, 2008).

Contrast Enhancement: when the contrast of the captured image is too low, it is difficult to detect and isolate objects of interest like OD and OC in fundus image case. Therefore, brightening or darkening a low-contrast image can be achieved by stretching (spreading) the histogram of that image through approaches such as histogram equalization and histogram specification. Moreover, in order to stretch the contrast of a full-color image, it is logical to spread the color intensities uniformly, leaving the colors themselves unchanged; therefore, as mentioned in the previous paragraph, the HSI color space is ideally suitable for color histogram processing (Gonzalez and Woods, 2008).

2.6.3 Histogram Equalization:

The Histogram Equalization technique used for adjusting image intensities to enhance contrast. Let f be a given image represented as amr by mc matrix of integer pixel intensities ranging from 0 to $L - 1$. L is the number of intensity level equal 256. Let p denote the normalized histogram with a bin for each possible intensity.

$$\mathcal{P}_n = \frac{number\ of\ pixels\ with\ intensity\ n}{total\ number\ of\ pixels} \quad n = 0,1, \ldots L-1. \tag{2.1}$$

The image after histogram equalization g will be defined by

$$g_{i,j} = floor\left((L-1)\sum_{n=0}^{f_{i,j}} p_n\right) \tag{2.2}$$

Where floor () rounds down to the nearest integer. This is equivalent to transforming the pixel intensities, k off by the function

$$T(k) = floor\left((L-1)\sum_{n=0}^{k} p_n\right) \tag{2.3}$$

The motivation for this transformation comes from thinking of the intensities of f and g as continuous random variables X, Yon [0,$L\ -\ 1$] with Y defined by

$$Y = T(X) = (L-1)\int_o^x px\ (x)dx \tag{2.4}$$

Where px defined as probability density of f and T is the cumulative distributive of X multiplied by ($L\ -\ 1$). Assume for simplicity that T is differentiable and invertible. It can then be shown that Y defined by $T(X)$ is uniformly distributed on [0, $L\ -1$], namely that (Mandar and Meghana, 2015)

$$py(\mathcal{Y}) = \frac{1}{L-1} \tag{2.5}$$

$$\begin{aligned}\int_0^y py(z)dz = probability\ that\ 0 \le Y \le y \\ = probability\ that\ 0 \le X \le T^{-1}(y) \\ = \int_0^{T-1} px(y)dy\end{aligned} \tag{2.6}$$

$$\frac{\mathrm{d}}{\mathrm{dy}}\left(\int_0^{\mathrm{y}} \mathrm{py(z)dz}\right) - \mathrm{pY(y)} = \mathrm{px}\left(\mathrm{T}^{-1}(\mathrm{y})\right)\frac{\mathrm{d}}{\mathrm{dy}}\left(\mathrm{T}^{-1}(\mathrm{y})\right) \tag{2.7}$$

2.6.4 Filtering

Spatial linear filters (e.g. mean filter), as well as non-linear filters (e.g. median filter) are used for image smoothing and noise removal. Conversely, first derivative filters (e.g. Prewitt and Sobel filters), as well as second derivative filters (e.g. Laplacian filter) are used for image sharpening (i.e. deblurring) as well as the detection of edges, lines, and points. Moreover, an image can be also filtered in the frequency domain in order to smoothen and sharpen it by using low-pass filters and high-pass filters, respectively (Gonzalez and Woods, 2008).

For common noises like salt and pepper noise, Gaussian noise and speckle noise can all be cleaned by using spatial filtering techniques.

a. Median filtering**:** The Median filter almost used to removal the salt and pepper noise using that the median value. If there are an even number of values, the median is the mean of the middle two. A median filter is an example of a non-linear spatial filter, by the equation:

$$f(x,y) = median\{g(s,t)\}\ , s,t \in Sxy \qquad (2.8)$$

Let Sxy represents a set of rectangular sub-image with window size $(m\ x\ n)$ centered at (x,y).

Median Filtering Algorithm:

$$Allocate\ output\ Pixel\ Value\ [image\ width]\ [image\ height]$$
$$Allocate\ window\ [window\ width\ *\ window\ height]$$
$$edgex :=\ (window\ width\ /\ 2)\ rounded\ down$$
$$edgey :=\ (window\ height\ /\ 2)\ rounded\ down$$
$$for\ x\ from\ edgex\ to\ image\ width\ -\ edgex$$
$$for\ y\ from\ edgey\ to\ image\ height\ -\ edgey$$

$$i = 0$$

$$for fx\ from\ 0\ to\ window\ width$$

$$for fy\ from\ 0\ to\ window\ height$$

$$window[i] := inputPixelValue[x + fx - edgex][y + fy - edgey]$$

$$i := i + 1$$

$$sort\ entries\ in\ window$$

$$outputPixelValue[x][y] :$$

$$= window[window\ width * window\ height / 2]$$

b. Adaptive filtering**:** Adaptive filters are a class of filters which change their characteristics according to the values of the greyscales under the mask, is implemented by applying a function to the grey values under the mask.

c. Mean filter: The mean filter is a simple sliding-window spatial filter that replaces the center value in the window with the average (mean) of all the pixel values in the window. The window, or kernel, is usually square but can be any shape as mentioned in https://www .markschulze .net/java/meanmed.html, the filter can represent by the equation:

$$F(x, y) = \frac{1}{mn} £\, g(s, t) \qquad (2.9)$$

d. Guided filter: The guided filter performs edge-preserving smoothing on an image, using the content of a second image, called a guidance image, to influence the filtering. The guidance image can be the image itself, a different version of the image, or a completely different image. Guided image filter takes into account the statistics of a region in the corresponding spatial neighborhood in the guidance image when calculating the value of the output pixel. If the guidance is the same as

the image to be filtered, the structures of the output image are the same as the original image and the guidance image. When the guidance image is different, the filtered image will follow it and affect in the original image structure. This effect is called structure transference.

e. Gaussian Filter: The guided filter is a well-known local filter for its edge-preserving property and low computational complexity, are ideal to start experimenting with filtering because their design can be controlled by manipulating just one variable- the variance. The function is defined as

$$G(x,y) = \frac{1}{2\pi\sigma^{2^e}} - \frac{x^2+2_y}{2\sigma^2}$$

(2.10)

The value of the sigma (the variance) corresponds inversely to the amount of filtering, smaller values of sigma means more frequencies are suppressed and vice versa (Kou *et al.*2015).

2.6.5 Morphological Processing:

This technique can be applied as an image enhancement technique as well as an image segmentation technique. The two fundamental operations of morphological processing are dilation and erosion; in which dilation leads to thickening the original object, whereas erosion is an inverse procedure in which an object is thinned. Moreover, erosion and dilation can be applied together after one another and in a reversed order as well, in order to achieve opening and closing, respectively. Opening generally removes small objects from an image while preserving the shape and size of large objects in the image; whereas closing generally merges narrow breaks or gaps and eliminates small holes in the image (Dougherty, 2009),(Gonzalez and Woods,

2008), in segmentation the morphological operation can use for boundary smoothing and can use for blood vessel removing.

The boundary smoothing by morphological operations which are:

a. **Opening**: The opening of an image f by a structuring element s (denoted by $f \circ s$) is an erosion (erosion denoted by $\ominus$), followed by a dilation (dilation denoted by $\oplus$), then opening $f \circ s = (f \ominus s) \oplus s$. The opening operation used to open up a gap between objects connected by a thin bridge of pixels and the regions survived will be restored to their original size by dilation. The benefit of opening with a disc structuring element is that it smoothens corners from the inside and, by doing the entire operation it removes further noise, round corners from inside and abridges the image (Ravi *et al*.2013).

b. **Closing**: The closing of an image f by a structuring element s (denoted by $f \bullet s$) is a dilation, followed by erosion $f \bullet s = (f \oplus s) \ominus s$, in morphological operations, closing is used to fill holes and keeping the initial region sizes unchanged. This closing operation is the opposite of the opening operation used to smoothen corners. The main objective of this operation is to smoothen the contour and maintains the shape and size of the object. A combination of both of these operations we are able to get better results for detecting edges in-depth image (Ravi *et al*.2013), to improve the segmentation process vessel remove are applied to the digital fundus image as a preprocessing step.

Vessel removes by opening morphological operation where it is of an image f by a structuring element s (denoted by $f \circ s$) is an erosion followed by a dilation: $f \circ s = (f \ominus s) \oplus s$. It used for it can open up a gap between objects connected by a thin bridge of pixels. Any regions that have survived the

erosion are restored to their original size by the dilation, and that makes the blood vessel dilated with it is surrounded pixel and disappeared. Opening morphological techniques probe an image with a small shape or template called a structuring element it is positioned at all possible locations in the image and it is compared with the corresponding neighborhood of pixels there for the optic disc is a circle shape the structuring element choose was a disk with corresponding neighborhood of pixels 8 to get good and fast result in vessel removing from https:/ /www.cs.auckland. ac.nz/ courses/ comp sci 773 s1c/lectures/ImageProcessing-html/topic4.htm.

Step (2) – Processing: Image Segmentation

Image segmentation is technique used for dividing an image into multiple parts to identify specific object or other relevant information in digital images. There are many different ways to perform image segmentation, including Thresholding methods (global, Otsu's method), Color-based Segmentation such as K-means clustering, Transform methods such as watershed segmentation, Texture methods such as texture filters, here the color retinal image has segmented https ://www .mathworks. com/discovery /image-segmentation.html.

The main objective of processing the fundus image typically aims to the segmentation of the OD and OC within an image. Segmentation is an essential step prior to feature extraction and classification in a fundus image. The example methods of image segmentation are:

a. **Region-Based Methods:** the objective of such methods is to produce connected regions, based on similarity, that are as large as possible (i.e. produce as few regions as possible) allowing some flexibility within each region (Dougherty, 2009) For

example, region-growing, as its name implies, groups the seed pixels or sub-regions into larger similar regions based on predefined criteria of growth such as specific ranges of color (Gonzalez and Woods, 2008).

b. **Boundary-Based Methods:** the objective of such methods is to determine a closed boundary, based on differences and discontinuities, such that an inside object (e.g. optic disc) and an outside boundary (edge) can be defined (Dougherty, 2009), some of the methods Gradient operators (e.g. Prewitt and Sobel kernels), the Laplacian, Laplacian of Gaussian (LOG), Difference of Gaussians (DOG) and the canny edge detector are detecting image boundaries (edges) methods (Gonzalez and Woods, 2008).

c. **Color-Based Methods:** in order to segment an image based on color, the segmentation technique can be carried out on either the HSI color space or the RGB color space. It is intuitive to use the HSI space because color is conveniently represented in the hue plane (H), and saturation (S) is typically used as a masking image in order to isolate further regions of interest in the hue image, while the intensity (I) is used less frequently for segmentation of color images because it carries no color information. However, better results can be obtained using the RGB color vectors by measuring and comparing the Euclidean distance between an RGB pixel and a specified color range (Gonzalez and Woods, 2008).

d. **Active Contour (Snakes):** the main aim of active contour models or snakes is to evolve a curve in order to detect objects in

an image. For instance, starting with an initial curve around the object to be segmented within an image, the curve (i.e. snake) is pulled toward nearby features (i.e. local minima) such as lines and edges, locating them accurately (Kass, *et al*. 1988) ,(Chan,2001).

e. **Matched segmentation:** a matched filter describes the expected appearance of a desired object or region of interest for purposes of comparative modeling. Thus, the segmentation process is carried out by isolating the region (pixels) having the least accumulated difference compared to the matched filter (Youssif, *et al*. 2008).

f. **Thresholding:** an image is easily and speedily segmented by selecting a threshold which partitions images directly into regions based on intensity values and/or properties of these values. Global thresholding and local thresholding are two types of thresholding that may be applied to an image; global thresholding is a segmentation technique that uses a constant threshold over the entire image, whereas local (variable) thresholding uses a variable threshold that changes over an image based on the properties of a neighborhood (e.g. average intensities of a neighborhood) (Gonzalez and Woods, 2008).

The thresholding segmentation assumes that the intensity values are different in different regions, and similar to represents the corresponding object, in fixed thresholding, the threshold value is held constant throughout the image and treating each pixel independently of its neighborhood.

Fixed thresholding is of the form: $g(x,y) = \sum_{1}^{0} \begin{matrix} f(x,y) < t \\ f(x,y) >= t \end{matrix}$ (2.11)

Where t is thresholding level.

The global thresholding algorithm used for disc and cup segmentation is

1) Select an initial estimate for T

2) Segment the image using T. This will produce two groups of pixels. G1 consisting of all pixels with gray level values >T and G2 consisting of pixels with values ≤T.

Where the threshold level (T) can be chosen manually or by using automated techniques, manual threshold level selection is normally done by trial and error, using a histogram as a guide (Prasantha *et al.* 2010).

After disc segmentation step is to smooth the disc boundary by erosion and dilation operation, where it is operation expands or thickens foreground objects in an image are applied to segmented disc and border cleared to suppresses structures that are lighter than their surroundings and that are connected to the disc border. For segmented disc the algorithm tends to reduce the overall intensity level in addition to suppressing border structures (Soille, 1999),binarization image that to convert an intensity image to a binary image with global threshold level, function uses Otsu's method, which chooses the threshold to minimize the interclass variance of the black and white pixels (Otsu,1979).

g. **Morphological Watershed:** the watershed transform is a powerful segmentation tool that aims to isolate and separate the touching objects within an image. Segmenting an image via watershed is a two-step process; first, finding the markers and the segmentation criterion used to split the regions which are most often the contrast or gradient. Second, performing a marker-

controlled watershed with these two elements in order to control over-segmentation (Gonzalez and Woods, 2008), (Math Works).

In this research, a digital fundus image used is a projection of retinal structures on two-dimensional color plane where the OD appears as a bright circular or elliptic region partially occluded by blood vessels. OD segmentation is a challenging task mainly due to blood vessel occlusions, ill-defined boundaries, and image variations near the disc boundaries due to pathological changes. Specifically, the occurrence of similar characteristics regions (atrophy) near disc boundary, a sample image is shown in Figure [2.22] to illustrate the above conditions.

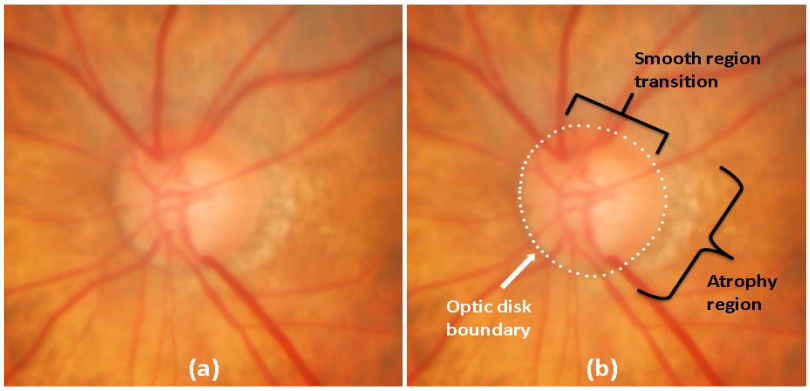

Figure [2.22]: a) Original color retinal image, b) Highlighting ill-defined boundary region and image variation near OD boundary due to atrophy (a pathological change).

Step (3) – Post-Processing: Features Extraction and Selection

After the eye fundus image has been preprocessed and segmented, features extracted from the internal skeleton of the recognized region, the results classified to distinguish or annotated the glaucoma disease with the appropriate description, automatically compared to the ground truth in order to evaluate the accuracy of experimental work, as explained in the following section.

2.7 Feature Extraction Background

The primary task of feature extraction is to take an input pattern and correctly assign it as one of the possible output classes to recognize the image as glaucoma or healthy. This process can be divided into three general stages:

Feature extraction, selection, and Classification. Features extraction is to collect information from the specific part of the image, then feature selection is important to the whole process since the classifier will not be able to recognize from wrong features. Definition to choose the powerful features given by Lippman are: “Features should contain the information required to distinguish between classes, be insensitive to irrelevant variability in the input, and also be limited in number, to permit, efficient computation of discriminant functions and to limit the amount of training data required”.

In glaucoma detection feature extraction and selection are very important steps in the construction of the CAD system. In this process, relevant features are extracted from the cup, disc, and RNFL to form glaucoma features. These features are then used by classifiers to recognize the input image compared with the background image. Thus, feature extraction is the process to extract a set of features from the raw data to maximize the recognition rate with the least amount of elements and to generate the similar feature set for recognition new images (Gaurav *et al*. 2014).

In digital fundus images, feature extraction is classified based on the type of features. The type of feature is divided into two groups are: morphological and non-morphological (Anindita Septiarini *et al*.2015). The morphological features are geometric parameters extracted from the image after segmentation process like RNFL, PPA, and CDR, disc and cup area, CDR and neuro-retinal rim area. The non-Morphological are whole image

features that mean extracted from the existing image (Image-based featured). Color, shape, and texture are the type of the features that extracted from the whole image to represent the characteristic of glaucoma disease. The Color feature can be used to recognize the cup, neuro-retinal rim, PPA features. The blood vessels, neuro-retinal rim and PPA can be extracted using shape feature, while RNFL can be extracted by texture feature.

(Anum *et al*. 2016) proposed method introduces a suspect class in automated diagnosis based on structural and non-structural features and evaluates this algorithm using a local database containing 100 fundus images. This system is designed to classify glaucoma cases from non-glaucoma and the motivation behind introducing suspect class is to ensure high sensitivity of the proposed system. The system results achieved average sensitivity and specificity 100 and 87 % respectively.

An example of the non-morphological feature presented by (Rama *et al.* 2012), which discuss a system for the automated detection of normal and glaucoma cases using higher order spectra (HOS), trace transform (TT), and discrete wavelet transform (DWT) features from the whole fundus image. Then the extracted features are classified using the support vector machine (SVM). In this work, the SVM classifier achieved an accuracy of 91.67%, and sensitivity and specificity of 90% and 93.33%, respectively. Furthermore, their proposed algorithm called Glaucoma Risk Index (GRI) which is composed of HOS, TT, and DWT features to aid the clinicians to make a faster glaucoma diagnosis during the mass screening of normal/glaucoma images

An example of a morphological feature in the study by (Xu *et al.* 2007) the disc and cup was segmented using free-form deformable model (snake)

technique, Then boundary was extracted based on the combination of information from the smoothness, gradient, depth as a modification to the original snake technique. The method is tested in 100 retinal fundus images having both normal and glaucoma from the National University Hospital. The results accuracy for boundary detection was 94%.

The features used in this research in combined the morphological and non-morphological features by extracted the shape, color and texture features from the segmented OD and OC and RNFL parts.

2.8 Shape Features

Shape features are features used to describe an object, using its most important characteristics and can be described by many parameters like: center of Gravity/centroid, the axis of least inertia, digital bending energy, eccentricity, circularity ratios, elliptic variance, rectangularity, convexity, solidity, Euler number, profiles, and whole area ratio. In this research measures, several properties describe shape for each disc and cup within an image via Matlab built-in function (region prop) from https://octave.sourceforge.io/image/function/regionprops.html.

Region props compute Area, Euler Number, Centroid, Filled Area, Filled Image, Extent, Major Axis Length, Minor Axis Length, Solidity and Perimeter, these measurements applied for disc and cup masks. For measuring these features a binary image obtained the view as a binary function

$$f(x,y) = \begin{cases} 1 \; if(x,y) \in D \\ 0 \; otherwise \end{cases} \quad (2.12)$$

2.8.1 The Centroid

The centroid determine the object center points, which illustrate by this formula:

Centroid$(\vartheta x, \vartheta y)$ is:

$$\begin{cases} \vartheta x = \frac{1}{N} \sum_{i}^{N} = 1xi & (2.13) \\ \vartheta y = \frac{1}{N} \sum_{i}^{N} = 1yi & (2.14) \end{cases}$$

Where N represent the number of point in the shape.

2.8.2 Eccentricity

Eccentricity is the measure of aspect ratio, it's ratio of the length of the major axis to the minor axis which calculated by principal axes method or minimum bounding rectangular box.

2.8.3 Solidity

The ratio of the pixels in the convex hull and found in the region returned as a scalar. Computed as Area/Convex Area.

Solidity describes the extent to which the shape is convex or concave (Annesha, 2013) and it is defined

$$Solidity = A_s / H \quad (2.15)$$

Where, As is represent the shape area and H is the convex hull area of the shape, therefore the solidity of a convex shape is equal 1.

2.8.4 Area

The actual number of pixels in the region, can calculate as the equivalent diameter of a circle with the same area as the region returned using the formula:

$$\text{Area} = (4 * Area/pi) \quad (2.16)$$

2.8.5 Major Axes

The length of the major axis of the ellipse that has the same normalized second central moments as the specific region in pixels.

2.8.6 Minor Axes

The length of the minor axis of the ellipse that has the same normalized second central moments as the specific region in pixels.

2.8.7 Extent

The extent is ratio of pixels in the segmented region to pixels in the total bounding box. Computed as the Area divided by the area of the bounding box.

2.8.8 Perimeter

The perimeter is the length of the entire outside boundary of the segmented region, by calculating the distance between each adjoining pair of pixels around the boundary of the region.

2.9 Color Features

Are measures that characterize color distribution in an image in order to compare how similar two images are based on color, Since color moments encode both shape and color information they are a good feature to use under changing lighting conditions, The greatest advantage of using color moments comes from the fact that there is no need to store the complete color distribution (Stricker and Orengo, 2015).

These color features extracts not only the color distribution but also extracts the spatial information of pixels in the images. In addition, as used in

many research like (Annesha and Joydeep, 2013). Their paper propose a new multi-feature image clustering technique with high accuracy level using color moments feature from an image, and combine them with the histogram analysis features. Finally, they used a canny edge detection technique to combine all features in a matrix and perform clustering algorithm to cluster data and achieved accuracy 90.5%.

(Stricker and Orengo, 2009) use three central moments of an image's color distribution. They are Mean, Standard deviation and Skewness, which calculated to the 3 channels (Red, Green, and Blue), therefore, is characterized by 9 moments 3 moments for each 3 color channels. We will define the $i-th$ color channel at the $j-th$ image pixel as Pij. The three color moments can defined as:

2.9.1 Mean

The first color feature can be explained as the average color in the image, and it can be calculated by the formula:

$$E\boldsymbol{i} = \sum_{j}^{N} 1\frac{1}{N}p_{ij} \qquad (2.17)$$

Where N is the number of pixels in the image pij and is the value of the $j-th$ pixel of the image at the $i-th$ color channel.

2.9.2 Standard Deviation

The second color feature, which is calculating by taking the square root of the variance of the color distribution.

$$\sigma i = \sqrt{\left(\frac{1}{N}\sum_{j=1}^{N}\left(\mathrm{p_{ij}} - E_i\right)^2\right)} \qquad (2.18)$$

Where E_i represent the mean value, for the $i-th$ color channel of the image.

2.9.3 Skewness

The third color feature is the skewness using to measure how asymmetric the color distribution is, and give information about the shape of the color distribution. Skewness can be computed by the following formula:

$$S_i = \sqrt[3]{\left(\frac{1}{N}\sum_{j=1}^{N}\left(p_{ij} - E_i\right)^3\right)} \quad (2.19)$$

2.10 Texture Feature

There are many methods can be used to describe the main features of the textures such as directionality, smoothness, coarseness, and regularity. Gray-Level Co-occurrence matrices measure is one of the most important measures that can be used to describe the texture, in this research two techniques used to describe the RNFL texture.

GLCM feature method: It is a method to calculate spatial relationship of pixels is the gray-level also known as the gray-level spatial dependence matrix by characterizing the texture of an image by calculating how often pairs of pixel with specific values and in a specified spatial relationship occur in an image, creating a GLCM, and then extracting statistical measures which are:

Autocorrelation, Contrast, Correlation, Cluster Prominence, Homogeneity, Cluster Shade, Difference variance, Dissimilarity, Energy, Entropy, Maximum probability, Sum of squares, Sum average, Sum variance, Sum entropy, Difference entropy, Information measure of correlation1, Inverse difference, Inverse difference normalized, Inverse difference moment normalized, some formula examples: GLCM texture features emphasize spatial relationship between pixels, rather than one single pixel intensities. The Gray-Level Co-occurrence Matrix represent the relationship of combinations of the pixel intensities and provides second-order statistical information. Features generated GLCM are also known as Haralick features,

where extracted from the RGB images after converted into grayscale images, and here twenty-two features are extracted from this GLCM.

2.10.1 GLCM Algorithm

The feature calculate after quantize the image, each sample is treated as a single image pixel and the value of the sample is the intensity of that pixel, then further quantized into a specified number of discrete gray levels.

1. Create the GLCM as square matrix with size N x N ,where N is the number of levels specified under quantization using this steps:

a. The sample under consideration for the calculation equal s.

b. Let W be the set of samples surrounding the s and within a window centered by s of the size specified under window size.

c. Considering only the samples in the set W, define each element i, j of the GLCM as the number of times two samples of intensities i and j occur in specified a spatial relationship (where i and j are intensities between 0 and Number of levels-1). The sum of all the elements i, j of the GLCM will be the total number of times the specified spatial relationship occurs in W. Make the GLCM symmetric:

i. Make a transposed copy of the GLCM

ii. Add this copy to the GLCM itself. This produces a symmetric matrix in which the relationship i to j is indistinguishable for the relationship $j\ to\ i$ (for any two intensities$i\ and\ j$). As a consequence the sum of all the elements i, j of the GLCM will now be twice the total number of times the specified spatial relationship occurs in W (once where the sample with intensity i is the reference sample and once where the sample with intensity j is the reference sample), and for any given i, the sum of all the

elements i, j with the given i will be the total number of times a sample of intensity i appears in the specified spatial relationship with another sample (https:/ /support.echoview .com/ WebHelp/Windows_and_ Dialog_ Boxes /Dialog_ Boxes/Variable _properties_dialog_box/Operator_pages/GLCM_Texture_Features.htm).

2. Normalize the GLCM: Divide each element by the sum of all elements the elements of the GLCM may now be considered probabilities of finding the relationship i, j $(or\ j, i)$ in W.
3. Calculate the selected Feature. This calculation uses only the values in the GLCM. After GLCM matrix extracted 22 features used to describe these relations, an example of these equations are:

Energy feature

$$Energy = \sum_{i,j=0}^{N-1} (p_{ij})^2$$

Entropy feature

$$Entropy = \sum_{i,j=0}^{N-1} -In(p_{ij})\,(p_{ij})$$

Contrast feature

$$contrast = \sum_{i,j=0}^{N-1} p_{ij}\,(i-j)^2$$

Homogeneity feature

$$Homgeneity = \sum_{i,j=0}^{N-1} \frac{p_{ij}}{1(i-j2)}$$

Correlation feature

$$correlation = \sum_{i,j=0}^{N-1} p_{ij}\,\frac{(i-\mu)(j-\mu)}{\sigma^2}$$

Shade feature

$$\text{Shade} = \text{sgn}(A)\lceil A \rceil\, {}^{1}/_{3}$$

Prominence feature

$$\text{Prominence} = \text{sgn}(\text{B})\lceil \text{B} \rceil\, {}^{1}/_{4}$$

Where:

$P\ ij = \ Element\ i, j$ Of the normalized symmetrical GLCM

N= Number of gray levels in the image as specified by Number of levels in under Quantization on the GLCM texture page of the Variable Properties dialog box

μ = the GLCM mean (being an estimate of the intensity of all pixels in the relationships that contributed to the GLCM), calculated as:

$$\mu = \sum_{i,j-0}^{N-1} ip_{ij} \quad (2.20)$$

Note: The mean of all the pixels in the data window W, σ 2 Is the variance of all pixels contributed to the GLCM, calculated as:

$$\sigma^2 = \sum_{i,j-0}^{N-1} p_{ij} (i - \mu)^2 \quad (2.21)$$

Note: the variance of the intensities of all the pixels in the data window *W* https://support.Echoview.Com

$$A = \sum_{i,j=o}^{N-1} \frac{(i+j-2_{\mu})^3 p_{ij}}{\sigma 3\left(\sqrt{2(1+\mathcal{C})}\right)^3} \quad (2.22)$$

2.11 Tamara Method

This method to calculate Coarseness, Contrast, and Directionality features for fundus image where:

2.11.1 Coarseness

The most important texture feature which it aims to identify the largest size at which a texture exists, and even a smaller micro texture exists. It calculates by takes averages at every point over neighborhoods the linear size of which are powers of 2. And for average over the neighborhood of size 2k ×2k at the point (x, y) calculated using:

$$A_k (x, y) = \sum_{i=x-2^{k-1}-1}^{x+2^{k-1}-1} \sum_{j=y\ 2^{k-1}}^{y+2^{k-1}-1} f(i,j)/2^{2k} \quad (2.23)$$

To take difference between pairs of averages at each point, based on non-overlapping neighborhoods on opposite sides of the point in both horizontal and vertical orientations. In the horizontal case, this is

$$E_{k,h}(x, y) = \left|A_K(x + 2^{k-1}, y) - (x - 2^{k-1}, y)\right| \quad (2.24)$$

At each point, one then picks the best size which gives the highest output value, where k maximizes E in either direction. The coarseness measure is then the average of S opt (x, y) =2k opt over the picture.

2.11.2 Contrast

It is a statistical distribution of the pixel intensity defined as α4 = μ4/σ4 where μ4 represent the fourth moment and σ2 is the variance. Contrast is measured by the following formula:

$$F_{con} = \frac{\sigma}{\alpha^{1/}_{4}4} \tag{2.25}$$

2.11.3 Direction Degrees

To calculate the direction of the gradient vector at each pixel, the direction of the vector mode is defined as:

$$|\Delta G| = (|\Delta_H| + |\Delta_v|)/2$$

$$\theta = \tan^{-1}(\Delta_v/\Delta_H) + \pi/2 \tag{2.26}$$

Where in ΔH and ΔV are the following two 4x4 operator variation resulting in horizontal and vertical directions by the image convolution.

$$\begin{matrix} -1 & 0 & 1 \\ -1 & 0 & 1 \\ -1 & 0 & 1 \end{matrix} \qquad \begin{matrix} 1 & 1 & 1 \\ 0 & 0 & 0 \\ -1 & -1 & -1 \end{matrix} \tag{2.27}$$

Using this steps:

1. The gradient vector of all the pixels is calculated.
2. Histogram is built for the expression of HD θ value.

3. The first range of values θ histograms was discrete, then the corresponding statistics for each bin of | ΔG | is greater than the number of pixels in a given threshold.

4. The histogram of an image for a clear directional exhibit a peak, for no apparent direction of the image is relatively flat performance.

5. The final image can be calculated by the directional sharpness of peaks in the histogram obtained is defined as follows:

$$F_{dir} = \sum_{p}^{n_P} \sum_{\emptyset \in \omega\rho} (\theta - \theta\rho)\, 2\, H_D\, (\emptyset) \qquad (2.28)$$

Where, np is the histogram of all the peaks, p, Wp represents all peaks included in the bin, and the bin having the highest φp value (Swati and Yadav, 2015).

2.12 Feature Selection

It is the process to select the most relevant features (variables, predictors) to be used in the CAD system reconstruction, for four main reasons:

a) simplification of the system for researchers and users, (Gaurav *et al*. 2014),
b) Shorter training and prediction time.
c) To avoid and minimize the curse of dimensionality.
d) Enhanced accuracy by reducing over-fitting and reduction of variance (Gareth *et al*. 2013).

The important of feature selection technique is remove the *redundant* or *irrelevant* data without incurring much loss of information. (Bermingham *et al*. 2015). Redundant or irrelevant features are decrease the system accuracy

since one relevant feature may be redundant in the presence of another relevant feature with which it is strongly correlated (Guyon *et al*. 2003). Feature selection techniques used there are too much features and comparatively few samples. In this research 2 types of feature selection are used:

1. Sequential feature selection
2. T-test feature selection.

2.12.1 Sequential Feature Selector

Sequential feature selection algorithms are used to reduce an initial *d*-dimensional feature space to a *k*-dimensional feature subspace where $k < d$. A approach such as sequential feature selection is wrapper technique useful if embedded feature selection like LASSO.

This method remove or add one feature at the time based on the classifier performance until a feature subset of the desired size *k* is reached. There are four different types of the Sequential Feature Selector:

1. Sequential Forward Selection (SFS)
2. Sequential Backward Selection (SBS)
3. Sequential Forward Floating Selection (SFFS)
4. Sequential Backward Floating Selection (SBFS)

The SFFS and SBFS selectors are extensions to the simpler SFS and SBS algorithms, where these floating algorithms have an additional exclusion or inclusion step to remove features once they were included (or excluded) so that a larger number of feature subset combinations can be sampled if the

resulting feature subset is assessed as "better" by the criterion function after removal (or addition) of a particular feature.

2.12.2 Sequential Forward Selection (SFS)

Input: $Y = \{y1, y2, \ldots, yd\}$ (2.29)

a. The ***SFS*** algorithm takes the whole *d* dimensional feature set as input.

Output: $Xk = \{xj | j = 1, 2, \ldots, k; xj \in Y\}$ (2.30)

Where$k = (0, 1, 2 \ldots d)$

b. SFS returns a subset of features; the number of selected features *k*, where $k < d$ has to be specified *a priori*.

Initialization: $X0 = \emptyset, k = 0$ (2.31)

- The algorithm with an empty set ("null set") so that *k*=0 (where *k* is the size of the subset).

Step 1 (Inclusion):

$$x+ = argmax\, J(xk + x),\ where\ xY - Xk \quad (2.32)$$

$Xk + 1 = Xk + x +$

$k = k + 1$

Go Step 1

An additional feature, $x +$ added to the feature subset $Xkx +$ is the feature that maximizes our criterion function, that is, the feature that is associated with the best classifier performance if it is added to *Xk*. This final step repeated until the termination criterion is satisfied.

Termination: $k=p$

then features from the feature subset Xk added until the feature subset of size k contains the number of desired features p as priori (Ferri *et al*. 1994), (Pudil *et al*. 1994).

2.13 Classification

The selected features of image representation that are generated from feature selection, are used in glaucoma detecting using knowledge-based model and classification methods (Dhawan and Dai, 2008). Feature and image classification techniques namely:

2.13.1 Statistical Classification Methods

The categories of these methods are an unsupervised and supervised approach. The unsupervised method cluster the data based on their separation in the feature space, include K-means and fuzzy clustering. On the other hand, a supervised approach needs training data, test data, and class label to classify the data, include probabilistic methods like the nearest neighbor and Bayesian classifier (Dhawan and Dai, 2008).

2.13.2 Rule-Based Systems

The system analyzes the feature vector using multiple sets of rules that are designed to test specific conditions in the feature vector database to set off an action. The rules consist of two parts: condition premises and actions, which are generated based on an expert knowledge to decide the action when the conditions are satisfied. The action which part of the rule could change the database state or label of a feature vector based on a specific state of analysis. Usually, a rule-based system consists of three sets of rules: supervisory or strategy rules, a focus of attention rules, and knowledge rules. The supervisory

or strategy rules control the analysis process and provide the control actions include starting and stopping action.

The strategy rules determine which rules would be tested during the analysis process. The focus-of-attention rules provide specific features within analysis process by accessing and extracting the information or features from the database. Subsequently, the rules convey the information from the input (database) into the activity center where the implementations of knowledge rules are scheduled. Finally, the knowledge rules analyze the information related to the required conditions then execute an action that changes the output database (Dhawan and Dai, 2008).

2.13.3 Support Vector Machine (SVM)

The SVM is a supervised machine learning algorithm used for both classification and regression problems, but mostly at classification. The SVM plots each feature value as a point in n-dimensional space. Then, classification performed by finding the hyper-plane that differentiate between the two classes.

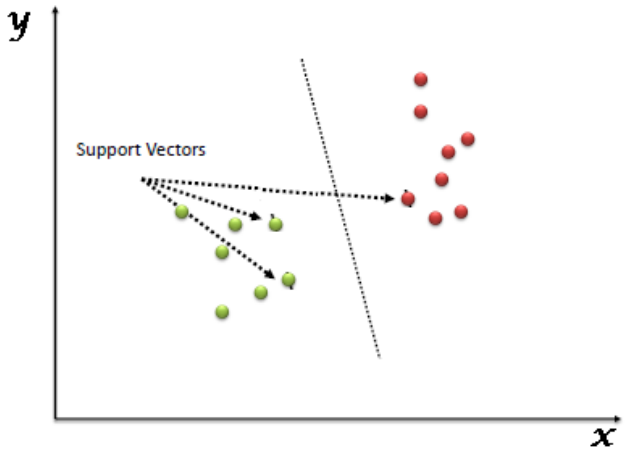

Figure [2.23]: Show Support Vector Machines

Support Vector Machines are very powerful classification algorithm, used in conjunction with random forest and other machine learning tools become very high predictive power. You will find these algorithm very useful to solve some of the medical imaging classification. In addition to performing linear classification, SVMs can efficiently perform a non-linear classification using what is called the kernel trick, implicitly mapping their inputs into high-dimensional feature spaces (https://www.analyticsvidhya.com/blog/2017/09/understaing-support-vector-machine-example-code/).

2.13.4 k-Nearest Neighbors Algorithm (*k*-NN)

The *k*-nearest neighbor's algorithm (*k*-NN) is a non-parametric method used for classification in the input consists of the *k* closest training examples in the feature space. The *k*-NN can be used for classification or regression:

1. In *k-NN classification*, the output is classified by a majority vote of its neighbors, as assigned to the class most common among its *k* nearest neighbors (*k* is a positive integer, typically small), when $k = 1$, the object is simply assigned to the class of that single nearest neighbor.
2. Where, *k* is a user-defined constant, and an unlabeled vector (test point) is classified by assigning the label which is most frequent among the *k* training samples nearest to that test point.

3. The used distance metric for continuous variables is Euclidean distance, and for discrete variables the overlap metric (or hamming distance). For gene expression microarray data, the *k*-NN can employed with correlation coefficients like Pearson and Spearman (Jaskowiak, 2011). The classification accuracy of *k*-NN can be improved if the distance metric is learned with specialized algorithms such as Large Margin Nearest Neighbor or Neighborhood components analysis.

Distance Functions

$$Euclidean\ \sqrt{\sum_{i=1}^{k}(x_i - y_i)^2} \quad (2.\ 33)$$

$$Manhattan\ |x_i - y_i| \quad (2.34)$$

$$Minkowski\left(\sum_{i=1}^{k}(|x_i - y_i|)^q\right)^{1/q} \quad (2.35)$$

Note: the three distance measures are only valid for continuous variables, for categorical variables the Hamming distance must be used and also when there is a mixture of numerical and categorical variables in the dataset.

Hamming Distance

$$D_H = \sum_{i-1}^{k}\lceil x_i - y_i \rceil \quad (2.36)$$

$$x = y \Longrightarrow D = 0$$

$$x \neq y \Longrightarrow D = 1$$

The KNN algorithm (Adi Bronshtein, 2017) steps are:

1. A test point *k* is specified, along with a new sample.
2. The k entries selected in the database which are closest to the new sample.
3. The most common classification found of these entries, is the classification we give to the new sample

KNN features:

i. KNN stores the training dataset, and does not learn any model.
ii. KNN makes predictions by comparing the similarity between an input sample and each training instance.

2.13.5 Some Advantages and Dis-Advantages of KNN

2.13.5.1 Advantages

1. For nonlinear data no assumptions about data that good.
2. Simple, easy algorithm to understand.
3. High accuracy, but not competitive in comparison to better supervised learning classifier.
4. It useful for classification and regression.

2.13.5.2 Disadvantages

1. High memory requirement for saving the results.
2. Stores all the training data for that it computationally expensive.
3. Prediction stage might be slow (with big N) and take time.
4. Sensitive to irrelevant features and the scale of the data, that reduce the accuracy.

2.13.6 Ensemble Learning

Zhi-Hua Zhou definition" Ensemble learning is a machine learning paradigm where multiple learners are trained to solve the same problem. In contrast to ordinary machine learning approaches which try to learn *one* hypothesis from training data, ensemble methods try to construct a *set* of hypotheses and combine them to use".

Ensemble algorithms used to obtain better predictive performance than could be obtained from any classifier alone. Unlike a statistical ensemble which is concrete by finite set of alternative models, but allow for some flexible structure to exist among those alternatives.

2.13.6.1 Bootstrap Aggregating (Bagging)

Bootstrap aggregating known as bagging, is designed to improve the stability and accuracy of machine learning algorithms used in statistical classification/regression. It useful for reduces variance, avoid over fitting, and applied to decision tree methods, and used with any type of method.

The Bootstrap Aggregating working Technique via generate a training set of size n, bagging m new training sets, each of size n', by sampling from D uniformly and with replacement. If $n'=n$, then for large n the set to have a fraction $(1 - 1/e)$ (≈63.2%) of the unique examples of D, the rest being duplicates (Aslam *et al.* 2007). This type of sample is known as a bootstrap sample. The m models are fitted using the above m bootstrap samples and merge with averaging the output for regression or voting for classification (Shinde *et al*. 2014).

On the other hand, it can mildly improve the performance using methods such as K-nearest neighbors (Breiman, 1996).

2.13.6.2 Boosting

Boosting technique working based on training each new model instance to emphasize the training instances that previous models misclassified. Sometimes, boosting has been shown better accuracy than bagging, but it also tends to be over-fit the training data. Therefore, the most common implementation of Boosting is AdaBoost, now days some newer algorithms are reported to achieve better results.

2.14 Classification Imbalanced

Imbalanced features are the problem where one class outnumbers other class by a large proportion, it found more frequently in binary classification problems than multi-level classification problems. Thus, a data set that exhibits an unequal distribution between its classes is considered to be imbalanced and this problem affects in the classifier performance, these are some methods used to solve the problem:

1. Under sampling
2. Oversampling
3. Synthetic Data Generation
4. Cost Sensitive Learning

- **Under Sampling:** This method used with majority class, to reduce the number of observations from majority class and make the data set balanced, and best to use huge data set to reducing the number of training samples and helps to improve run time and storage troubles.

- **Oversampling:** This method works with minority class, to replicates the observations from minority class and balance the data, called as up-sampling.
- **Synthetic Data Generation:** This method instead of adding the observations from the minority class, it solves the problem by generates artificial data, kind of oversampling technique.

The synthetic minority oversampling technique (SMOTE) is a powerful and widely used method (Manohar, 2011), creates artificial data based on feature space as a random set of minority class observations to shift the classifier bias for the minority class, by generating artificial data using bootstrapping and k-nearest neighbors by this way:

1. Take the difference between the feature vector and its nearest neighbor.
2. Multiply the difference between the feature vector and its nearest neighbor by a random number between 0 and 1.
3. Add the multiplication result to the feature vector under consideration.
4. This causes the selection of a random point along the line segment between two specific features.

- **Cost-Sensitive Learning (CSL):** Commonly used technique to solve the classification problems with imbalanced data by evaluates the cost associated with misclassifying observations.

This method highlights the imbalanced learning problem by using cost matrices which describes the cost for misclassification scenario but does not create balanced data distribution. Thus, researches have shown that cost-sensitive learning have many times outperformed sampling methods, this

method provides likely alternative to sampling methods. (https://www.analyticsvidhya.com/blog/2016/03/practical-guide-deal-imbalanced-classification-problems/).

2.15 Theoretical Conclusion

The glaucomatous impairment progresses slowly due to delaying the patients' untreated of the disease. Early glaucoma detection is essential to manage the irreversible damage to the vision and the blindness. In addition, glaucoma comes in various forms and is highly complicated, but availability and development of various eye imaging instruments and CAD systems facilitated the identification of the glaucomatous structural changes and early diagnosis. From discussed studies CAD system based on fundus images could help to save the vision of millions of people by adopting the therapy procedures to the new findings faster, cheap and accurate, which is the method followed in this research.

CHAPTER THREE
RELATED WORKS

In this chapter, a review of the influential and exciting works that are related to this research based on glaucoma risk factors mentioned in (chapter two), optic disc and optic cup segmentation methods and the existing computerized approaches in literature.

3.1 OD and OC Segmentation

In this section an overview of several methods for OD and OC segmentation that have been evaluated by their authors on publicly available datasets with both images and ground truth provided.

Huazhu *et al*. (2018) a deep learning method, named M-Net, which, used in OD and OC segmentation jointly in a one-stage multi label system. It consists of multi-scale input layer, U-shape convolutional network, side-output layer, and multi-label loss function. For improving the segmentation performance further, they also introduce the polar transformation, which provides the representation of the original image in the polar coordinate system, the proposed method also obtains the glaucoma detection performances with calculated CDR value on both ORIGA and SCES datasets.

Artem, (2017) this work presents universal approach for automatic optic disc and cup segmentation, which is based on deep learning, namely, modification of U-Net convolutional neural network. Their experiments include comparison with the best known methods on publicly available databases DRIONS-DB, RIM-ONE v.3, DRISHTI-GS the results show 96% dice coefficient for disc segmentation in rim-one database and 85% dice coefficient for disc segmentation in DRISHTI-GS.

Vaishnavi Kamat *et al*. (2017) this paper present a method to detect Glaucoma using Enhanced K-Strange Points Clustering algorithm to obtain cup, disc and the blood vessels. And elliptical fitting method is used to compute CDR and ISNT, which are used as inputs to the Naïve Bayes classifier.

Kartik *et al*. (2017) detected the Glaucoma from Retinal Fundus Images by analyzing ISNT measurement and features of optic cup and blood vessels algorithm uses four different features of ONH used to detect glaucoma, there algorithm works effectively because it uses four features of ONH together and use the results in grouping the image into glaucomatous, healthy or unresolved, other research can be done by analyzing textural changes of RNFL.

Almazroa *et al.* (2017) presenting a novel OD segmentation algorithm based on applying a level set method on a localized OD image, and prevent the blood vessels from interfering with the level set process, an in painting technique was applied, the accuracy of the algorithm in marking the optic disc area and centroid was 83.9%, and the best agreement was observed between the results of the algorithm has been test using 379 images.

As Maureen at (2017) assess the impact of manual and default threshold selection on the reliability and accuracy of skull STL models using different CT technologies tested using female and male human cadaver head were imaged by multi-detector row CT, dual-energy CT, and two cone-beam CT scanners. Four medical engineers manually thresholded the bony structures on all CT images.

The skull STL models generated by the lowest and highest selected mean threshold values, and the geometric variations between all manually thresholded were calculated. Furthermore, in order to calculate the accuracy of the manually and default thresholded STL models, all STL models were superimposed on an optical scan of the dry female and male skulls ("gold standard"). They found intra- and inter-observer variability of the manual threshold selection was good (intra-class correlation coefficients >0.9**)**.

Jen *et al.* (2017) developed and trained a convolutional neural network to automatically segment optic disc, fovea and blood vessels, In average, segmentation correctly classified 92.68% of the ground truths (on the testing set from Drive database). Where highest accuracy achieved on a single image was 94.54% and lowest 88.85%. And found the convolutional neural network can be used to segment blood vessels, but also optic disc and fovea with high accuracy.

Sirshad *et al*. (2016) which segmented disc using of gradient extracted from line profiles that pass through optic disk margin and results of performance evaluation for OD boundary segmentation as average values achieved for jaccard coefficient, dice coefficient and distance between OD centers are 0.8331, 0.9078 and 6.44, respectively.

Abdullah *et al*. (2016) presented a robust methodology for optic disc detection and boundary segmentation, which is preliminary step in the development CAD system for glaucoma in retinal images. The proposed method is based on morphological operations, circular Hough transform and the grow-cut algorithm. The method is quantitatively evaluated on five publicly available retinal image databases DRIVE, DIARETDB1, CHASE_DB1, DRIONS-DB, Messidor and one local Shifa Hospital Database

and achieves an optic disc segmentation success rate of 100% for the above databases with 99.09% and 99.25% accuracy for the DRIONS-DB, and ONHSD databases, respectively. The OD boundary detection results obtained an average spatial overlap of 78.6%, 85.12%, 83.23%, 85.1%, 87.93%, 80.1%, and 86.1%, respectively, for these databases.

Prasad *et al*. (2015) presented optic disc and optic cup segmentation based on superpixel classification, before that adaptive histogram equalization and Gabor filter are used basically for classifying each superpixel as disc or non-disc and Cup to disc ratio CDR is evaluated and compared with threshold value for detection of glaucoma.

Satish *et al.*(2015) proposes segmentation of optic disc and optic cup using superpixel classification, and for optic disc segmentation, clustering algorithms are used to classify superpixels as a disc or non-disc. But for optic cup segmentation the Gabor filter and Thresholding added to the clustering algorithms.

Medha *et al*.(2014) investigate and compare performance of five methods used for Optic disc segmentation. These five methods are based on use of algorithms namely; distance regularized level set, Otsu Thresholding, region growing, particle Swarm optimization, generalized regression neural network, which tested on a single database. The method using generalized regression neural network best suits application due to highest region agreement, lowest non-overlap ratio, lowest relative absolute area difference and low execution time.

For optic cup segmentation task, authors of Ingle and Mishra, (2013) use 2-layer multi-scale convolutional neural network trained with boosting. Training process pipeline is multi-stage and includes patches preparation and

neural network training. For pre-processing, entropy filtering, in L*a*b* color space is performed for extracting the most important points of an image, 4 followed by contrast normalization and standardization of patches. Gentle AdaBoost algorithm is then used to train convolutional filters, which are represented as linear repressors for small patches. At the test time, image propagation through the network is followed by unsupervised graph cut, The method was evaluated on DRISHTI-GS database, and it outperformed all other existing methods in terms of Intersection-over-Union score and Dice score However, it is necessary to note that this method crops images by area of their optic disc (cup) before performing segmentation of the optic disc (cup). It makes the method not applicable to new, unseen images of full eye fundus, since it requires a bounding box of optic disc and cup to be available in advance.

Ingle and Mishra, (2013) discuss the cup segmentation based on gradient method as the gradient is the variation in the intensity or color of an image. The gradient images convolved with a filter. Two methods were used to find the gradient:

(1) linear gradient,

(2) Radial gradient. The contrast was improved for all image components (red, blue, and green) by Contrast Limited Adaptive Histogram Equalization, (Zuiderveld, 1994)**.**

The initial threshold was set for red (R), blue (B), and G (green) components after much iteration to detect the region where R less than 60 and B and G more than 100, where other pixels were eliminated by setting their values to zero. The intensities were computed and linearly transformed to the range of (0-1). They found that G and B channels were more effective for OC

segmentation. The circular structural elements were used to fill the blood vessels region in order to obtain a continuous region. The algorithm was evaluated based on the accuracy of the cup and disc area in all directions as well as CDR, instead of relying on the accuracy only in one direction. The algorithm can be extended to distinguish between the glaucomatous and normal images.

The Jun *et al*. (2013**)** proposes optic disc and optic cup segmentation using superpixel classification for glaucoma detection. In optic disc segmentation they use histograms, and center surround statistics to classify each superpixel as disc or non-disc. For optic cup segmentation, they use the histograms, center surround statistics, and the location information used as feature space to improve the performance. The proposed segmentation methods have been tested on 650 images with optic disc and optic cup boundaries manually marked as a ground truth. Experimental results obtained an overlapping error 9.5% and 24.1% in optic disc and optic cup segmentation, respectively. The segmented optic disc and optic cup are then used to compute the cup to disc ratio for glaucoma detection and achieved areas under curve of 0.800 and 0.822 in two data sets. Thus, this methods can be used for segmentation and glaucoma detection and the self-assessment can use as an indicator of cases with large errors and enhance the clinical deployment of the automatic segmentation and detection.

Lalonde *et al.* (2001) Gagnon propose an OD localization scheme using Hausdorff based template matching and pyramidal decomposition. A similar method is proposed in (Pallawala, 2004) with an improved morphological based pre-processing step.

From the above studies concluded that OD is a challenging task mainly due to blood vessel occlusions, ill-defined boundaries, image variations near disc boundaries due to pathological changes and variable imaging conditions. Specifically, occurrence of similar characteristics regions (atrophy) near disc boundary, irregular disc shape and boundary are the most essential aspects to be addressed by an OD segmentation method, see chapter two. Due to the high density of blood vessels in the OC, segmentation in this region is more difficult than OD segmentation. Furthermore, the gradual intensity change between the cup and neuro-retinal rim causes extra complications for cup segmentation. In addition, glaucoma changes the shape of the cup region for these difficulties there is a need to found and modify new segmentation technique to get high segmentation accuracy, in this research a modify thresholding segmentation method for OD segmentation are applied and vessel removed to overcome these difficulties .

3.2 Disc to Cup Ratio (CDR)

In this section, a detailed review the OD and OC segmentation methodologies that automatically detect OD and OC boundaries. These segmentation techniques help doctors with diagnosing and monitoring glaucoma by providing them with clear and accurate information regarding the ONH structure and detect glaucoma based on CDR.

Sharanagouda *et al*. (2017) proposed a method unlike past works which relies on a single color channel for extracting the Optic Disk (OD) and Optic Cup (OC) used in CDR calculation, they propose a novel combined color channel and ISNT rule based automated glaucoma detection, and find that the proposed method betters single channel based giving an overall efficiency 97%.

Ranjith *et al.* (2015). The technique used here is a core component of ARGALI (Automatic cup-to-disc Ratio measurement system for Glaucoma detection and Analysis), a system for automated glaucoma risk assessment. The algorithm's effectiveness is tested on segmented retina fundus images, by comparing the automatic cup height using ARGALI with the ground truth, the result was the algorithm accurately detected neuro-retinal cup height. This work will improve the efficiency of glaucoma detection using fundus images of the eye.

Prasad *et al*. (2015) here optic cup and optic disc segmentation is used for assessment of optic nerve head. Segmentation is based on superpixel classification for both optic disc and optic cup segmentation. Firstly, for optic disc and optic cup segmentation adaptive histogram equalization and Gabor filter are applied basically for classifying each superpixel as disc or non-disc. Finally cup to disc ratio CDR is calculated and compared with threshold value for detection of glaucoma.

Kavitha *et al*.(2014) they describe a process to automatically locate the optic nerve in a retinal image. The optic nerve is one of the most important organs in the human retina can used to locate the OD position in fundus image, which is important for many reasons like glaucoma detection. The method is based on detection of the main retinal vessels, thus, the retinal vessels start from the OD and their path follows a similar directional pattern in all images. Glaucoma detection basically using the medical history, intra-ocular pressure and visual field loss tests of a patient together with a manual assessment of the OD, through ophthalmic. Since enlargement of the cup with respect to OD is an important indicator of glaucoma called CDR, various parameters are estimated and recorded to assess the glaucoma stage. The

results obtained smaller CDR errors and higher AUC in glaucoma detection by the proposed method, compared with previous methods. The proposed disc and cup segmentation tested at SCES dataset and achieved an AUC of 0.800, 0.039 lower than AUC of 0.839 of the manual CDR computed from manual disc and manual cup, and glaucoma detection result AUC 0.822 which is much higher than 0.660 by the currently used IOP measurement. They found the accuracy is good enough for a large-scale glaucoma, it is important to know how different partition affects the performance.

Mahalakshmi, (2014) proposed method to segment optic disc and optic cup using Simple Linear Iterative Clustering (SLIC) algorithm, K-Means clustering for glaucoma detection to obtain accurate boundary delineation. In optic disc and cup segmentation, histograms and center surround statistics are used to classify each super pixel as disc or non-disc, the location information is also included into the feature space to boost the performance. The segmented optic disc and optic cup are then used to compute the Cup to Disc Ratio (CDR) to confirm glaucoma for a patient.

Eleesa Jacob, (2014). In this project, an optic disc and optic cup segmentation is used for diagnosing glaucoma. The optic disc and optic cup segmentation using the super pixel classification technique. In optic disc segmentation, histograms and center surround statistics are used, the quality of the optic disc segmentation using self-assessment method. For optic cup segmentation, the location information is also included into the feature space to improve the performance in addition to the histograms and center surround statistics. Then segmented optic cup and optic disc used to compute the CDR to identify whether the given fundus image is glaucomatous or not.

The segmentation can be analyzed using the Matlab, as SobiaNaz *et al*.(2014) were calculate the CDR automatically. Using preprocessing methods such as anisotropic filtering have been performed and automatic disc extraction is done using 3 techniques 1) Edge detection method, 2) Optimal thresholding method, and 3) Manual threshold analysis. Threshold level-set method is used for the cup segmentation and tested on the DRIVE database.

Cheng, (2013) proposed the optic disc and optic cup segmentation for glaucoma detection. Using this method the optic disc segmentation, histograms, and center surround statistics are used for OD and OC segmentation, then calculating the cup to disc ratio value (CDR) for glaucoma detection. This method limitation was it had poor visual quality, Morphological operations were used to improve the algorithm and for locating the optic disc in retinal images as used by Angel Suero *et al.* (2013).

Achanta, (2012) proposed to improve the segmentation performance by using a super pixel algorithm, simple linear iterative clustering (SLIC) method. It empirically compares five state-of-the-art super pixel algorithms for their ability to adhere to image boundaries, speed, memory efficiency, and their impact on segmentation performance. However this method increased the computations.

Joshi,(2011) proposed an approach for an automatic OD parameterization technique based on segmented disc and cup regions obtained from monocular retinal images. The OD segmented using an active contour model, and by enhancing Chan- vese (C-V) model by including image information at the support domain around each contour point. The limitation of this method was that it does not provide better quality.

Babu (2011) proposed algorithm for the measurement of CDR. Thus, It considered as a parameter for the diagnosis of glaucoma. The result achieved 90% accuracy.

Muramatsu *et al.*(2011) again extended their previous work by presenting a technique for detecting the peripapillary atrophy (PPA) which is the other peripapillary feature of glaucoma. The objective of their procedure was to detect the PPA by using a texture analysis based on the gray-level co-occurrence matrix. In a dataset of 26 images, the sensitivity and specificity for detecting moderate to severe PPA regions was 73% and 95%, respectively.

Wong *et al.* (2010) Developed SVM-based model optic cup detection for glaucoma detection using the cup to disc ratio in retinal fundus images. Joshi G.D. *et al*. (2010) developed vessel bend-based cup segmentation in retinal images, Shijian Lu *et al*. (2010) proposed a background elimination method for the automatic detection of OD.

Gopal *et al*. (2010), developed a deformable model guided by regional statistics to detect the OD boundary and OC boundary detected based on Lab color space and the expected cup symmetry. This method uses sector wise information and give rise to fewer false positives and hence better specificity. In final results error value computed is less for a normal image than for a glaucomatous image.

Zhuo Zhang *et al.*(2009) designed a convex hull based neuro-retinal optic cup ellipse optimization technique, Hussain *et al*.(2008) proposed a method for optic nerve head segmentation using genetic active contours Huajun *et al*.(2007) designed a fractal-based automatic localization and segmentation of optic disc in retinal images.

The Active Shape Model (ASM) based optical disc detection is implemented by Huiqi *et al*.(2003). The parameters for this model is selected using Principal Component Analysis technique. The faster convergence rate and the robustness of the technique are proved by experimental results.

Comprehensive review provided of the algorithms used for OD and OC detection and that lead to diagnosis is of glaucoma by CDR. Many algorithms were limited due to the complexities of ONH structure appear in segmentation results which is very variable among people and among imaging devices and affected by papillary atrophy and disc drusen cause some difficulties for disc segmentation due to its similarity in intensity to disc boundaries, but there are some algorithms segmented the optic disc with PPA perfectly. On the other hand, disc drusen cause greater difficulty for segmenting since it covers boundary especially, in advanced cases.

Other difficulties are blood vessels, which affect localizing OD and OC and play an important role in the accurate segmentation of cup boundaries and represent a challenge facing many researchers. The algorithms performed differently depending on the datasets of images. Some approaches used a small dataset, while some used large datasets to train and test the algorithm. Also, the severity of the disease was different among the datasets used in different techniques; therefore, the corresponding algorithms cannot be compared with each other. Most of the OD segmentation was based on the circular Hough transform along with other detection techniques.

In conclusion segmentation of the optic disc and optic cup has been very important because it is from the basics of glaucoma diagnosis. Although there are still chances for improvement in segmentation techniques. Only a few of the existing methodologies, whether for optic disc or for optic cup

segmentation, can be applied for glaucomatous retinal images. Also, most of the current methods have been tested on a limited number of datasets, which do not provide images with many different characteristics. Furthermore, the generally low resolution of the images has made the segmentation process even more challenging. This can handled by advanced camera capable of taking high volumes of high-resolution retinal images. In order to achieve good outcomes for the images captured by different systems, robust and fast segmentation methods are required. Most of the retinal images used to evaluate segmentation methods have been taken from adults.

The glaucoma screening system complements but does not replace the work of ophthalmologists and optometrists in diagnosis; routine examinations have to be conducted in addition to the fundus image analysis. However, the system facilitates diagnosis by calculating the disc and cup structural parameters and showing greater details of ONH, such as the disc and cup areas, the vertical and horizontal cup-to-disc ratios, and cup to disc area ratio, and also checking the ISNT arrangement. This is a shareable opinion that could associate the worlds of consultant ophthalmologists, optometrists, orthoptists, and engineers.

This research contribution in optic disc and cup segmentations are used simple, fast, inexpensive technique for segmentation (global thresholding), and modified to solve PPA and drusen problems in disc segmentation, then tests in two databases to provide many different characteristics and achieve good outcomes, and the main contributions are the features, obtained from the OD and OC parts, which are color and shape features ,considered to be new features not the common CDR,ISNT and rim area mentioned in previous studies.

3.3 RNFL Review

Oh, *et al*. (2015) they propose an automatic detection method for RNFL defects on digital fundus images to detect glaucomatous from non-glaucomatous cases. The RNFL defects here detected based on the vertical dark bands, firstly the non-uniform illumination of the fundus image was corrected, secondly, the blood vessels were removed, and then images converted to polar coordinates using the center of the optic disc. Finally, false positives (FPs) were reduced by using knowledge-based rules. The results obtained were the sensitivity of 90% and a 0.67 FP rate per image for the 98 fundus images with 140 RNFL defects and 100 fundus images of healthy subjects. The RNFL defects with variable depths and widths, with uniformly high detection rates regardless of the angular widths of the RNFL defects. The overall accuracy was 0.94, 86% sensitivity, and 75% specificity.

The proposed CAD system successfully detected RNFL defects in digital fundus images. Thus, the proposed algorithm is useful for the detection of glaucoma. Imran Qureshi,(2015) introduce a survey paper, various image processing techniques as well as different computer-based systems involved particularly in the detection and diagnosis of glaucoma, are discussed in detail. This paper was to highlight the severity of glaucoma across the world as and survey the research work done so far on this disease. The future directions regarding detection of glaucoma can be an evaluation of various algorithms discussed in this paper by implementing and testing them on a large amount of data. Similarly, various arguments like the neuro-retinal rim area, width and vertical cup to disc ratio can be calculated which indicate the development of glaucoma. Thus, intensity of glaucoma can be determined by using 3D reconstruction image. Then the execution of optic cup segmentation

approaches can be improved by using vessel observing and vessel in painting also machine learning method will be used for the finding the best arguments in many patterns like threshold level set and edge detection. In future, more efforts are required for improvement of classification method and accuracy rate. There is a system required which accomplishes high execution by promoting a large number of data for making class and blending various detection approaches for the diagnosis of glaucoma.

Syed Hussain, (2015) introduce a survey paper depicts many works related to automated glaucoma detection, lowering eye pressure in glaucoma's based on early glaucoma diagnosis at early stages slows down the progression of the disease and helps save vision. Through the extensive literature review carried out it has been observed that there are various methods for detection of glaucoma with good results, but there is still a need to develop a Computer Aided System which can not only help diagnose glaucoma at early stage, but would also help in checking the progression of the disease to be prevented. A lot of recent research is being carried for detection of Glaucoma using fundus images, but still, detection of progression of Glaucoma inpatient remains to be researched. In the future, we need to develop more accurate, robust as well as affordable automated techniques for glaucoma detection. Once glaucoma is early and correctly diagnosed then they can treated right and avoid total blindness.

In Oh JE *et al*. (2015) they proposed a fully automatic method for detecting various forms and widths of RNFL defects in color fundus images. Fundus photography is the most common screening tool to detect RNFL defects in various optic neuropathies. However, the detection of RNFL defects by using fundus photographs depends on the experience of the examiner, and

early defects may be missed because of the low contrast of the RNFL. Therefore, they developed a simple and efficient algorithm to assist the ophthalmologist for the detection of RNFL defects the strength of the proposed algorithm is that it can detect very narrow defects in early stage glaucoma to non-glaucomatous optic neuropathy involving the papilla macular bundle accurately. Thus, no previous studies described specific methods for detecting RNFL defects with various forms and widths in fundus images. Their results showed that the proposed algorithm was successful, with a sensitivity of 90% for glaucoma and 100% for papilla macular bundle defects in non-glaucomatous optic neuropathies.

Siddeeqa *et al*. (2015) propose a method to compare retinal nerve fiber layer (RNFL) thickness in black and Indian myopic students at the University of KwaZulu-Natal. By Eighty (40 black and 40 Indian) participants of both genders and aged between 19 and 24 years (mean and standard deviation: 21 ± 1.7 years) were included in the study. Refractive errors were assessed with the Nidek AR-310A auto-refractor and via subjective refraction. RNFL thicknesses were then measured using the iVue-100 optical coherence tomography device.

Axial lengths were measured using the ultrasound device (Nidek US-500 A-scan). Data were analyzed by descriptive statistics, t-tests, Pearson's correlation coefficients, and regression analysis and they find the mean myopic spherical equivalent was significantly more negative in the Indian people (-2.42 D ± 2.22 D) than in the black people (-1.48 D ± 1.13 D) ($p = 0.02$). The mean axial length was bigger in the black people (23.35 $mm \pm 0.74\, mm$) than in the Indian people (23.18 $mm \pm 0.87 mm$) but the difference was not significant. The sample used (n = 80), and the average global RNFL

thickness ranged from 87 μm to 123 μm (105 μm $\pm 9\,\mu m$). Mean global RNFL thickness was slightly greater amongst black (108 μm ± 7μm) than amongst Indian (102μm ± 9μm) (p = 0.00) participants. Mean global RNFL thickness was similar for male (106 μm ± 7μm) and female (105 μm ± 10μm) (p = 0.79) participants. A positive and significant association between myopic spherical equivalent and global RNFL thickness was found for the total sample (r = 0.36, p = 0.00) and for Indians (r = 0.33, p = 0.04) but not for the black (r = 0.25, p = 0.13) participants. The results obtained a negative and significant correlation between axial length and global RNFL thickness between the Indian participants (r = -0.34, p = 0.03) but not between the total sample (r = -0.12, p = 0.30) or the black (r = 0.06, p = 0.73) participants.

The findings suggest that racial differences in RNFL thickness need to be considered in the clinical examination and screening for glaucoma and other optic nerve pathologies amongst black and Indian people. Additionally, the possible influences of refractive error and axial length should be considered when evaluating RNFL thickness.

Jan Odstrcilika *et al*. (2014) here introduce a novel approach to capture these variations using computer-aided analysis of the RNFL textural appearance in standard and easily available color fundus images. The proposed algorithm built based on the Gaussian Markov random fields and local binary patterns features, together with various regression models for prediction of the RNFL thickness. The algorithm describe the changes in RNFL texture, by reflecting variations in the RNFL thickness. The method tested on 16 healthy and 8 glaucomatous eyes. The results achieved significant correlation (normal s: = 0.72 ± 0.14; p-0.05, glaucomatous: = 0.58 ± 0.10; p 0.05) between the results of the predicted output and the RNFL thickness

measured by optical coherence tomography, which is the standard glaucoma assessment device. The evaluation achieved good results to measure possible RNFL thinning.

Iyyanarappan, (2014) in this paper, a wavelet-based texture feature set has been used. The texture feature used is the energy of sub-images. Wavelet transform is very efficient tools for feature extraction and they are very successfully used in biomedical image processing. Then the classification technique is developed to automatically detect the glaucoma from non-glaucoma cases. Texture Features by DWT achieved classification accuracy 95% and the system, easy to operate, non-invasive and inexpensive. They have carried out the classification by Probabilistic Neural Network for the purpose of examining the efficiency of the features extracted. Future work, to use more powerful classifiers used, classification accuracy may further be improved.

Kumar, (2014) Introduce review paper, we have studied many works related to automated glaucoma detection. Glaucoma is one of the vital factors contributing to most of blindness worldwide. So, there is a need to develop an inexpensive automated technique for accurate diagnosis of different stages and types of glaucoma. These techniques will help in less developed countries where there is an acute shortage of ophthalmologists. In the future, to develop more accurate, robust as well un-expensive automated techniques for glaucoma diagnosis, so they can be useful to the poor people. Thus, once glaucoma is correctly diagnosed then they can take proper medicine or undergo surgery in a timely manner to avoid total blindness.

Koprowski *et al*. (2014) the authors proposed a new method for automatic determination of the RNFL (retinal nerve fiber layer) and other

parameters using: mathematical morphology and profiled segmentation based on morphometric information of the eye fundus. A quantitative ratio of the quality of the optic disc and RNFL – BGA (bio morphological glaucoma advancement) was also proposed. The obtained results were compared with the results obtained from optic disc static perimetry were. The result achieved a correlation with the static perimetry 0.78 for the existed method of image analysis and 0.86 for the proposed method. The practical usefulness of the proposed ratio BGA and the impact of the three most important features on the result were assessed. The following results of correlation for the three proposed classes were obtained: cup/disc diameter 0.84, disc diameter 0.97 and the RNFL 1.0. Thus, analysis of the supposed visual field results in the case of glaucoma is possible based only on OCT images of the eye fundus. The calculations and analyses performed with the proposed algorithm and BGA ratio confirm that it is possible to calculate the supposed mean defect (MD) of the visual field test based on OCT images of the eye fundus.

Pachiyappan *et al.* (2012) proposed a technique for Glaucoma diagnosis utilizing fundus images of the eye and the optical coherence tomography (OCT). The Retinal Nerve Fiber Layer (RNFL) can be classified into anterior boundary which is top layer of RNFL, the posterior boundaries (bottom layer of RNFL) and also the distance in between the two boundaries. Glaucomatous and Non-Glaucomatous classification done depend on the thickness of the nerve fiber layer which is nearly $105\mu m$. This approach provided optical disc detection with 97.75% accuracy.

Jan *et al.* (2012), automatic method to RNFL texture analysis based on the combination of intensity, edge representation, and Fourier spectral analysis. DCFI with the size of 3504×2336 pixels (8 normal, 4

glaucomatous). The ability of proposed features to classify RNFL defects has been proven via comparison with OCT.

Prageeth *et al.* (2011) automatic method to texture analysis using only intensity information about RNFL presence. DCFI with the size of 768 × 576 pixels (300 normal, 529 glaucomatous) Intensity criteria were used for detection of the substantial RNFL atrophy.

Prageeth *et al*. (2011) in the ophthalmologic clinical practice, glaucoma diagnosis is based on evidence from multiple sources. Glaucoma doctors consider signs like patient's demographic data, medical history, vision measurement, IOP (Intra Ocular Pressure) as well as the assessment from various types of imaging equipment. Following the clinical decision-making process, it is natural for us to design an automatic classifier being able to combine inputs from multiple data sources. However, the limitations of the black-box manner in the supervised learning classifiers offer little insight to the clinicians of how the classifier works, thus hinder the deployment of such systems.

Acharya *et al*. (2011) automatic analysis of RNFL texture using higher order spectra, run length, and co-occurrence matrices. DCFI with the size of 560 × 720 pixels (30 normal, 30 glaucomatous). Specificity to detect glaucoma and obtained accuracy of over 91%.The article does not explain thoroughly how the features were extracted and in which area of the image was computed.

Many algorithms have been proposed for detecting RNFL defects. Prageeth *et al*. (2011) used texture analysis by utilizing only intensity information about the RNFL around the optic disc in the red-free fundus

image. Muramatsu *et al*. (2011) applied three sizes of Gabor filters to detect RNFL defects in the fundus image. The detection rates were 89% ~ 91% at 1.0 FPs per image. However, because determining the filter width for detecting RNFL defects with various forms and widths is difficult with these methods, they applied the Hough transformation to detect RNFL defect candidates with straight continuous lines. In addition, these previous studies confined their study subjects to those with glaucoma with localized RNFL defects, which would be apparently visible and found on OCT, however these studies did not include early stage pre-parametric glaucoma, other non-glaucomatous optic neuropathies, and papilla macular bundle defects.

Odstrcilik *et al*. (2010) proposed the use of texture analysis by utilizing Gaussian Markov random fields (GMRF) for classification of healthy and glaucomatous RNFL tissue in fundus images, their results were compared with the OCT images as a gold standard, using DCFI with size of 3504 × 2336 pixels (18 normal, 10 glaucomatous) the features ability to differentiate between healthy and glaucoma cases is validated using OCT RNFL thickness measurement.

Bock, *et al*. (2010) his contribution provides a competitive, reliable and probabilistic glaucoma risk index (GRI) from images as its performance is comparable to medical relevant glaucoma parameters. This proves, data-driven is able to extract relevant glaucoma features. In the future, it will be low-cost glaucoma detection that can help to route the patients to do not more elaborate clinical test.

The defects of the RNFL were most commonly located in the inferior temporal and superior temporal regions. These locations are the most frequently affected in the early stage of glaucoma. Additionally, the detection

rate of the proposed algorithm was almost consistent, regardless of the angular widths of RNFL defects. However, among the total defects, the proposed algorithm performed worse in cases with shallow defects (i.e., in early-stage glaucoma or in images with poor resolution). This study had several limitations. First, the number of images used in this study was not large; thus, a larger database should be used in the future. Second, they did not consider structural changes of the optic disc, such as cupping, notching, or pallor of the rim.

The change in the optic disc is an important indicator of the severity of glaucoma, and the detection of optic disc parameters can provide a significant differential clue regarding glaucomatous and non-glaucomatous optic neuropathies. Therefore, future work should be focused on the detection of optic disc changes, and combining these findings with RNFL defects. Further, regarding the high rate of false positives per image, modification of the FP reduction method may improve the reliability of the current algorithm for early detection of various optic neuropathies. In conclusion, the proposed algorithm showed a reliable diagnostic accuracy for automatically detecting RNFL defects in fundus photographs of various optic neuropathies.

Delia *et al*. (2006), presents segmentation of retinal layers from OCT images is fundamental to diagnose the progress of glaucoma disease. This study has shown that the retinal layers can be automatically and/or interactively located with high accuracy with the aid of local coherence information of the retinal structure. OCT images are processed using the texture features analysis by means of the structure tensor with the complex diffusion filtering. Experimental results indicate that our proposed novel

approach has good performance in speckle noise removal, enhancement, and RNFL lyre segmentation.

In conclusion a survey many works related to automated glaucoma detection by RNFL texture features, where has been observed that through various methods for detection of glaucoma have been carried out there is still a need to develop a Computer Aided System which can not only help diagnose glaucoma but would also help in checking the progression of the disease and prevent permanent blindness. Many of recent research using fundus images for Glaucoma detection, but still, the detection of Glaucoma progression remains to be researched. For these reasons, there is a need to develop more accurate, robust as well as affordable automated techniques for glaucoma detection.

Table (3.1): Comparison between different segmentation methods

Author	Year	Segmented part	Segmentation method	Data base	Results
Jun	2013	OD & OC	Superpixel	650 images	OD overlapping error 9.5%. OC overlapping error 24.1%
Abdullah	2016	OD	Morphological operation	4 Databases DRIVE DIARET_DB1 CHASE_DB1 DRIONS_DN	Spatial overlap 78.6% 85.1% 83.2% 85.1%
Sirshad	2017	OD	Line profile gradient	-	Jaccard 0.83 DSC 90%
Jen	2017	OD	Convolutional neural network	DRIVE	Accuracy 92.7%

Maureen	2017	Skull CT images	Manual threshold level	-	Correlation coefficient >.9
Almazroa	2017	OD	Level set	379 images	Accuracy 92.7%
Artem	2017	OD &OC	Deep learning U_NET	-	OD (DSC 96%) OC (DSC 85%)
Proposed method	2018	OD & OC RNFL	Modified thresholding by circle reconstruction	RIM_ONE v1. RIM_ONEv2. DRISHTI_GS DB database	**OD** (SSIM 83%,DSC 90%,Jaccard 82%). **OC** (SSIM 93%,DSC 73%, Jaccard 60%). Overall accuracy97%

Table (3.2): Comparison between different features types used to detect glaucoma from digital fundus images.

Authors	Year	Features
Proposed system	**2018**	**Color, shape and texture features**
R. Geetha Ramani	2017	Statistical features
Mohd Nasiruddin	2017	CDR, blood vessel ratio, disc to center distance
Sharanagouda	2017	CDR+ISNT
Claro M.	2016	Disc segmentation, texture feature
Salem	2016	CDR, texture and intensity based features
Swapna’	2016	Fractal Dimension +LBP
Oh, Yang	2015	RNFL defects
Abir	2015	Grid Color Moment
Morris T.	2015	BRIEF
Karthikeyan	2015	LBP + Daugman's algorithm
Iyyanarappan	2014	DWT
Eleesa Jacob	2014	CDR
Geetha Ramani	2014	color spaces, channel extraction, statistical, histogram
Guerre, A.,	2014	CDR
Jan	2014	RNFL
Maya	2014	Local Binary Patterns
Mahalakshmi	2014	CDR
Ganesh Babu	2014	CDR+ISNT
Kavitha	2014	CDR
Preethi	2014	CDR
Fauzia	2013	CDR,ISNT
Cheng	2013	CDR

Rama	2012	HOS,TT and DWT
Achanta	2012	CDR
Pachiyappen	2012	RNFL
Babu	2011	CDR
Muramatsu	2011	PPA
Wong	2010	CDR

The research contribution is OD segmentation by the new modification method based on global thresholding and reconstruct the segmented optic disc to be a full circle based on the truth the optic disc is circle part, which increases the segmentation accuracy and extracts the RNFL part in simple and accurate method by subtracting the ROI image from the optic disc part, because the RNFL is the layer surrounded the disc part and then used new color, shape and texture features to detect the glaucoma disease.

CHAPTER FOUR
RESEARCH METHODOLGY

4.1 Introduction

This chapter illustrates the introduction to the material and methods used in this research, the RIM-ONE database is employed and considered precise gold standards of the ONH. Figure [4.1] shows normal and abnormal glaucomatous images taken from the RIM-ONE database. Even if the images are clear, using the naked eye only can't distinguish between the normal (healthy) images and the abnormal (glaucoma) images, which necessities the automated system development.

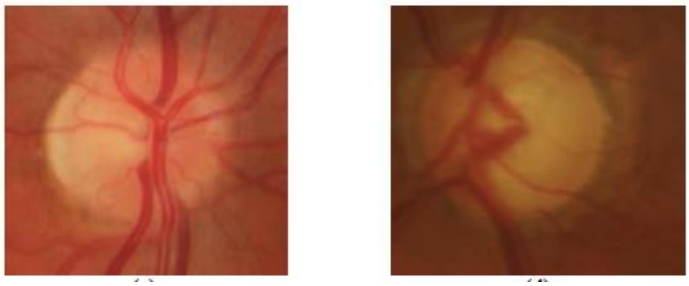

(a) (d)

Figure [4.1]: Shows RIM-ONE database images: (a) Normal image, (d) Glaucoma image (abnormal), an example of images used in the research.

4.2 Digital fundus Image Datasets

The fundus images are considered the raw material to be enhanced, segmented and evaluated. The image datasets are normally accompanied by a ground truth which acts as a benchmark for comparing and evaluating the achieved experimental results using the true results of that image set.

4.2.1 RIM- ONE Database (version two)

To assess the performance of the proposed glaucoma detection system digital retinal Image database for Optic Nerve Evaluation (RIM_ONE) database are used, totally 158 fundus images: 118 images for normal case and 40 images for glaucomatous cases, the camera used to capture these images is a fundus camera Nidek AFC-210 with a body of a Canon EOS 5D Mark II of 21.1 megapixels. This database designed as a part of a research project developed in collaboration with three Spanish hospitals: Hospital Universitario de Canarias, Hospital Clínico San Carlos, and Hospital Universitario Miguel Servet. The main differences among all the other databases and the RIM-ONE are the following: RIM-ONE is exclusively focused on ONH segmentation, it has a relatively large amount of high-resolution images (158) and manual reference segmentations of each image in collaboration with 5 glaucoma domain experts of these hospitals: 4 ophthalmologists and 1 optometrist to create of reliable gold standards for decreasing the variability between experts segmentations and the development of highly accurate segmentation algorithms. (Fumero *et al,* 2011). Figures [4.2] and [4.3] shows the normal and abnormal fundus images in the database respectively.

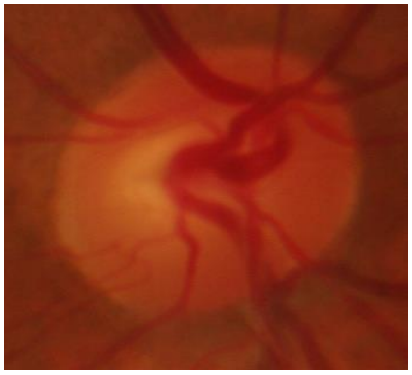

Figures [4.2]: Shows examples of normal fundus images from RIM-ONE database, where the cup is too small as indicator for healthy.

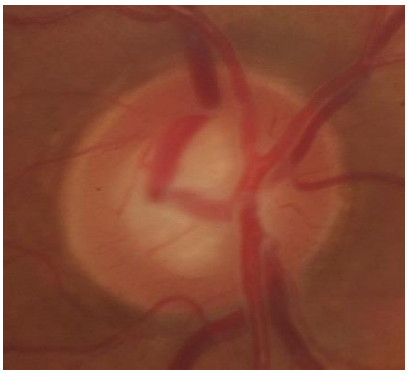

Figures [4.3]: Shows examples of abnormal fundus images from RIM-ONE database, where the cup enlargement are visible as the indicator for glaucoma.

4.2.2 Drishti –GS Database

Drishti _GS database: A comprehensive dataset of retinal images which include both normal and glaucomatous eyes and manual segmentations from multiple human experts. Both area and boundary-based evaluation measures are presented to evaluate a method on various aspects relevant to the problem of glaucoma assessment, which contains 101 images, 70 glaucoma and 31 healthy (Sivaswamy, 2014), The optic cup segmentation methodology and final features are evaluated on the Drishti –GS database, as it is the only public dataset, to our knowledge, that consists of the manual demarcation of the optic disc and cup boundaries by clinical experts, figure [4.4] and [4.5] examples of the database images.

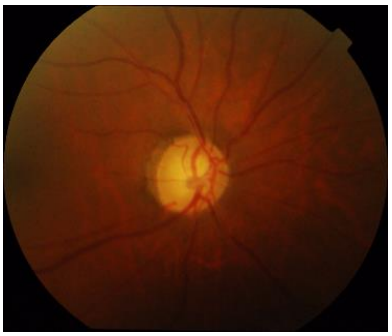

Figures [4.4]: Shows an examples the original fundus images from Drishti _GS database.

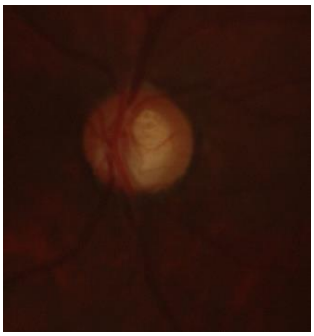

Figures [4.5]: Shows an examples the ROI fundus images from Drishti _GS database after crop the ONH part, which affected by glaucoma.

4.2.3 RIM- ONE Database (version one)

Which is the first version of the RIM-ONE database series, contain 455 images (200 glaucoma image and 255 glaucoma and glaucoma suspect images) with the same ground truth mentioned at (section 4.2.1).

4.3 Programming Environment

MATLAB is a high-level language used for visualization, numerical computation, and programming with a widespread. It can be used in various applications such as image and video processing, signal processing, control systems, bioinformatics, and communications. The simulation of the system proposed for glaucoma detection is done in MATLAB R2016, http://cimss.ssec.wisc.edu/wxwise/class/aos340/spr00/whatismatlab.htm.

Proposed algorithm provides an automated glaucoma detection based on CAD system that enables the ophthalmologists in early diagnosis of glaucoma patients with high accuracy, algorithm takes a preprocessed digital fundus image and segment the optic cup, optic disc and RNFL followed by a combined features (Arwa *et al.*2018) extracted from segmented parts to train the classifier and test the system, results used to classify the image as glaucoma or healthy.

4.4 Methodology

Figure [4.6]: Depicts the methodology used and clarify the flowing steps.

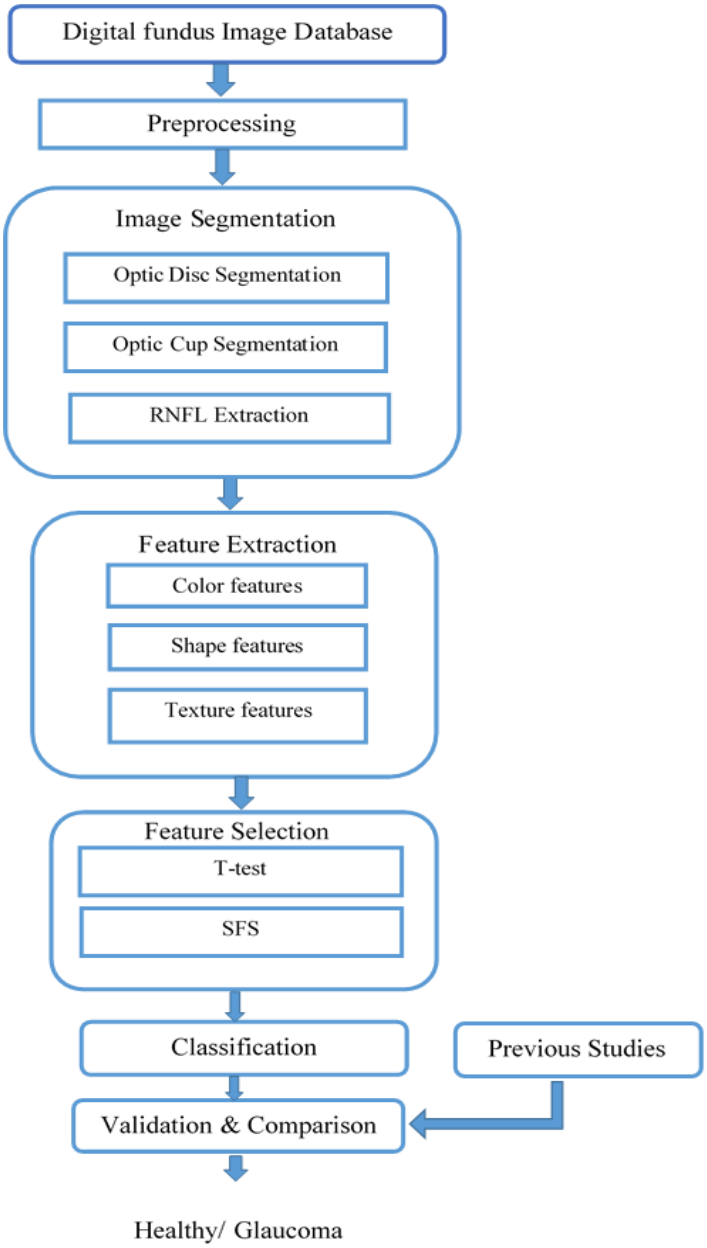

Figure [4.6]: Proposed Methodology used to diagnose glaucoma disease.

4.4.1 Image Preprocessing and Enhancement

Image pre-processing processes involved are, resizing the image to 256 X 256 pixels so that it has the specified number of rows and column to reduce

computational time, de noising stage by median filters (5× 5) (Arwa *et al*.2018) using the formula:

$$f(x,y) = median\{g(s,t)\}, s,t \in Sxy \quad (4.1)$$

Then contrast enhancement using histogram equalization to enhance image: $$g_{i,j} = floor\left((L-1)\sum_{n=0}^{f_{i,j}} p_n\right) \quad (4.2)$$

Before any procedures made, red channel has been extracted because it appear good boundary and less blood vessel ,which is affecting segmentation accuracy as to facilitate intensity analysis.

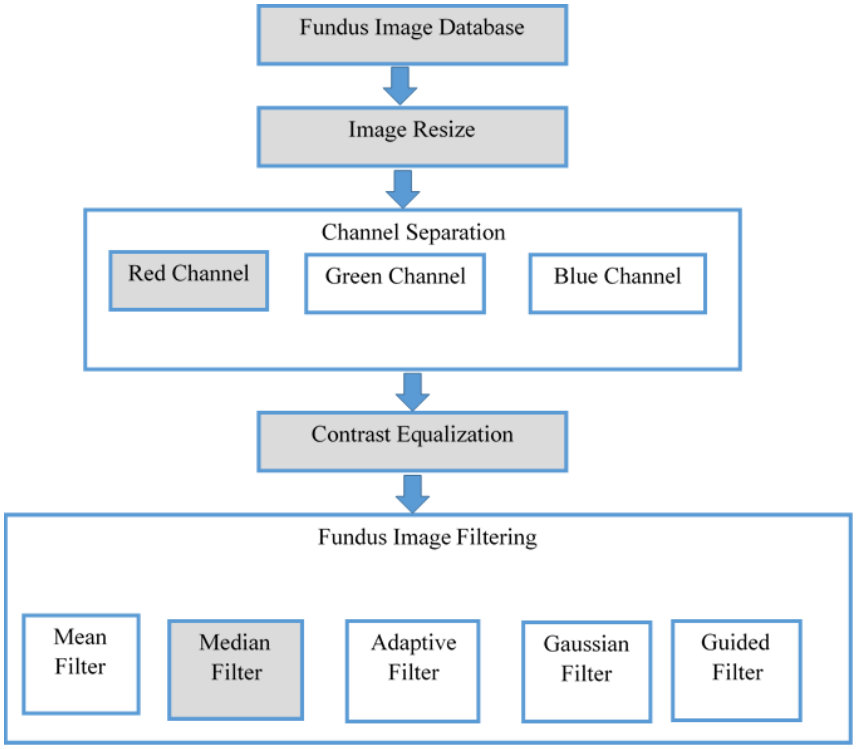

Figure [4.7]: Shows the preprocessing steps, the gray box was the selected methods.

4.4.2 Segmentation

The task of OD and OC segmentation is an important step to relatively quantify the changes in the OD and OC regions for evaluating glaucoma in the digital fundus image.

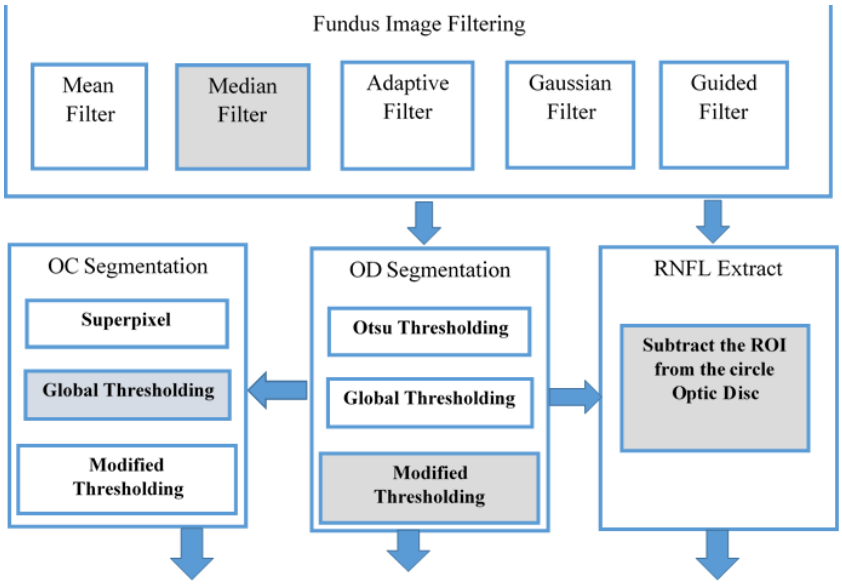

Figure [4.8]: Shows the segmentation steps, the gray box was the selected methods.

4.4.2.1 Optic Disc Segmentation

The Optic Disc Segmentation algorithm developed and tested in rim-one public database. The proposed method (Arwa *et al.*2018) can be divided into 4 steps, **first step** is vessel remove to get accurate segmentation, and it done by morphological operation, Opening: $f \circ s = (f \ominus s) \oplus s$ (4.3)

Closing operation: $f \bullet s = (f \oplus s) \ominus s$ (4.4)

Second step is applying thresholding level 180 to segment disc region from the red channel which appear best contrast to the disc region,

Fixed thresholding is of the form: $g(x,y) = \sum_{1}^{0} \begin{matrix} f(x,y) < t \\ f(x,y) >= t \end{matrix}$ (4.5)

Where t is thresholding level= 180.

after that in the **third step** is the boundary was smoothed and cleared from unconnected object and binary image obtained at the **final step** circle image was construct based on the radius and center of the detected region to minimize segmentation errors resulting from the main blood vessels and PPA surrounded the optic disc, using the formula

$$(x - h)2 + (y - k)2 = r2 \quad (4.6)$$

Where r= the radius from segmented object, h, k = the center from segmented object, figure [4.7] illustrate the proposed method steps.

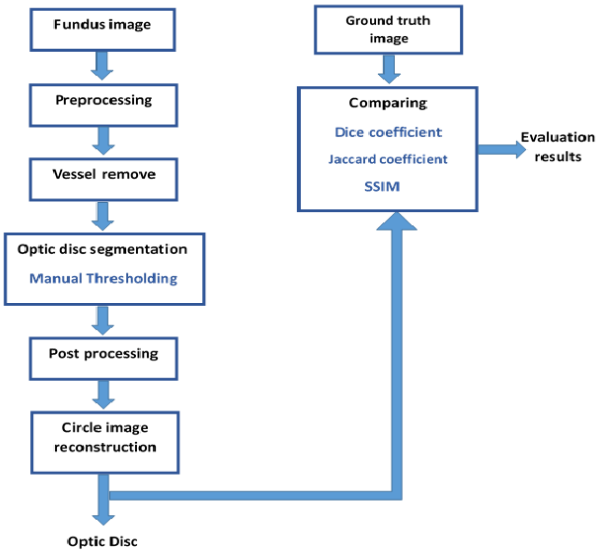

Figure [4.9]: Proposed method for optic disc segmentation algorithm.

Vessel removed by opening morphological operation, then threshold level are chosen manually using a histogram as a guide to get more accurate segmentation.

The post processing step is to smooth the boundary by erosion and dilation operation as mentioned in chapter two page 40, where it is operation expands or thickens foreground objects in an image are applied to segmented

disc and border cleared to suppresses structures that are lighter than their surroundings and that are connected to the disc border. For segmented disc the algorithm tends to reduce the overall intensity level in addition to suppressing border, binarization image that to convert an intensity image to a binary image with global threshold level, to obtain more accurate segmentation and based on the truth of the optic disc and optic cup are circular shape, logical circle image was constructed using the center point and the axis from the segmented object.

4.4.3 Optic Cup Segmentation

The enlargement of the cup region is an important indicator of the progression of glaucoma in an eye. The detection of cup boundary from a retinal image is the most challenging task as depth is the best marker for the cup which is lost in the two dimensional projection. In absence of three dimensional information, glaucoma experts use two dimensional visual images for determining the cup boundary.

4.4.3.1 Cup Proposed Method

The optic cup segmentation method proposed (Arwa *et al.*2018), depend on optic disc thresholding at level 240, which is the best level differentiate between the disc and cup parts then clear border, smoothing boundary and binaries the final image,

Fixed thresholding is of the form: $\mathrm{OC}(x,y) = \sum_{1}^{0} \begin{matrix} f(x,y) < t \\ f(x,y) >= t \end{matrix}$ (4.7)

Where t is thresholding level= 240, the proposed method illustrate in figure [4.8].

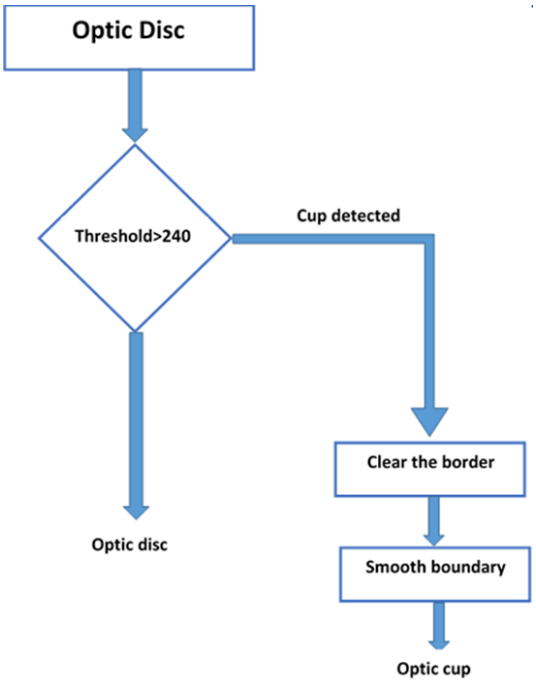

Figure [4.10]: Cup segmentation proposed algorithm based on thresholding technique from optic disc region.

The ROI was selected to be the optic disc because the optic cup is circular yellowish part inside the disc ,and this minimize segmentation error can happened due to PPA , Blood vessels and disc boundary itself. Where thresholding is the most common method of segmenting images into particle regions and background regions. A typical processing procedure would start with filtering or other enhancements to sharpen the boundaries between objects and their background. Then, the objects are separated from the background using Thresholding here the ROI was the entire optic disc, which already filtered and blood vessel removed in previous step (section 4.4).

Basic Global Thresholding includes:

1) Select an initial estimate for T

2) Segment the image using T. This will produce two groups of pixels. G1 consisting of all pixels with gray level values >T and G2 consisting of pixels with values ≤T.

Where the threshold level (T=240) can be chosen manually or by using automated techniques, manual threshold level selection is normally done by trial and error, using a histogram as a guide.

4.4.4 RNFL ROI Extraction

The RNFL (retinal nerve fiber layer) is the area surrounded the disc for that the ROI determines based on mathematical method to subtract the whole image form disc area, to measure it is thickness, which affect by the glaucoma disease.

$$RNFL = ROI\ region - OD \quad (4.8)$$

4.4.5 Feature Extraction Step

Depend on ophthalmologist observation Glaucoma is diagnosed by examination of size, structure, shape and color of optic nerve head and RNFL surrounded the optic nerve .Based on this theory a combination of texture, color and shape feature were applied to disc, cup and RNFL to classify glaucoma from healthy cases, this features are:

1. Shape features, 13 features applied for OD and OC.
2. Color features, 3 features applied for OD, OC and RNFL for each channels.
3. Texture features, 25 features applied for RNFL.

Shape features: In this research measures several properties describe shape for each disc and cup within an image via matlab built in function (region prop), which computes *Area, Euler Number, Centroid, Filled Area, Filled*

Image, Extent, Major Axis Length, Minor Axis Length, Solidity, Equivalent diameter and Perimeter, these measurements applied for disc and cup masks. For measuring these features (Arwa *et al*.2018) a binary image obtained, an examples of equations used are, for more detail (see section 2.7):

Centroid$(\vartheta x, \vartheta y)$ is:

$$\begin{cases} \vartheta x = \frac{1}{N} \sum_{i}^{N} = 1xi & (4.9) \\ \vartheta y = \frac{1}{N} \sum_{i}^{N} = 1yi & (4.10) \end{cases}$$

N is the number of point in the shape

$$\boldsymbol{Solidity} = A_s / H \quad (4.11)$$

$$\textbf{Area} = (4 * Area/pi) \quad (4.12)$$

Color features: are measures that characterize color distribution in an image in the same way that central moments uniquely describe a probability distribution. Color moments are mainly used for color indexing purposes as features in image retrieval applications in order to compare how similar two images are based on color. Three color moments are computed per channel, 9color feature are computed for each disc, cup and RNFL, and these features are mean, standard deviation and skewness.

Mean: The first color moment can be interpreted as the average color in the image.

$$E\boldsymbol{i} = \sum_{j}^{N} 1 \frac{1}{N} p_{ij} \quad (4.13)$$

Standard Deviation: The second color moment is the standard deviation, which is obtained by taking the square root of the variance of the color distribution.

$$\sigma i = \sqrt{\left(\frac{1}{N} \sum_{j=1}^{N} \left(\mathrm{p_{ij}} - E_i\right)^2\right)} \quad (4.14)$$

Skewness: The third color moment is the skewness. It measures how asymmetric the color distribution is, and thus it gives information about the shape of the color distribution (see section 2.8).

$$S_i = \sqrt[3]{\left(\frac{1}{N}\sum_{j=1}^{N}\left(p_{ij} - E_i\right)^3\right)} \quad (4.15)$$

Texture features: Many methods can be used to describe the main features of the textures such as directionality, smoothness, coarseness and regularity. Gray-Level Co-occurrence matrices measure is one of the most important measures that can be used to describe the texture, in this research two techniques are used to describe the RNFL.

GLCM method: A method used to calculate spatial relationship of pixels is the gray-level also known as the gray-level spatial dependence matrix by characterize the texture of an image by calculating how often pairs of pixel with specific values and in a specified spatial relationship occur in an image, creating a GLCM, and then extracting statistical measures which are:

Autocorrelation, Contrast, Correlation, Cluster Prominence, Homogeneity, Cluster Shade, Difference variance, Dissimilarity, Energy, Entropy, Maximum probability, Sum of squares, Sum average, Sum variance, Sum entropy, Difference entropy, Information measure of correlation1, Inverse difference, Inverse difference normalized , Inverse difference moment normalized, below are an examples of GLCM features equations see section (2.10.1).

Energy feature

$$Energy = \sum_{i,j=0}^{N-1}\left(p_{ij}\right)^2$$

Entropy feature

$$Entropy = \sum_{i,j=0}^{N-1} -In\left(p_{ij}\right)\left(p_{ij}\right)$$

Contrast feature

$$contrast = \sum_{i,j=0}^{N-1} p_{ij}\,(i-j)^2$$

Homogeneity feature

$$Homgeneity = \sum_{i,j=0}^{N-1} \frac{p_{ij}}{1(i-j2)}$$

Correlation feature ***Shade feature***

$$correlation = \sum_{i,j=0}^{N-1} p_{ij} \frac{(i-\mu)(j-\mu)}{\sigma^2}$$

$$\text{Shade} = \text{sgn}(A)\lceil A \rceil^{1}/_{3}$$

Prominence feature

$$\text{Prominence} = \text{sgn}(\text{B})\lceil \text{B} \rceil^{1}/_{4} \quad (4.16)$$

Tamara method: A method used to calculate Coarseness, Contrast, and Directionality features for digital fundus image:

Coarseness: The most fundamental texture feature which, a direct relationship to scale and repetition rates, it aims to identify the largest size at which a texture exists, even a smaller micro texture exists.

$$A_k(x,y) = \sum_{i=x-2^{k-1}-1}^{x+2^{k-1}-1} \sum_{j=y\,2^{k-1}}^{y+2^{k-1}-1} f(i,j)/2^{2k} \quad (4.17)$$

Contrast: is a statistical distribution of the pixel intensity obtained.

$$F_{con} = \frac{\sigma}{\alpha^{1}/_{4}4}$$

Direction: degrees we need to calculate the direction of the gradient vector is calculated at each pixel (see section 2.11).

$$F_{dir} = \sum_{p}^{n_P} \sum_{\emptyset \in \omega\rho} (\theta - \theta\rho)\, 2\, H_D(\emptyset) \quad (4.18)$$

4.4.6 Features Selection

It is the process of selecting a subset of relevant features (variables, predictors) for use in model construction, in this research 2 type of feature selection are used:

A. Sequential feature selection

B. T-test feature selection.

SFS: remove or add one feature at the time based on the classifier performance until a feature subset of the desired size is reached.

T-test: the t-test is any statistical hypothesis test in which the test statistic follows a Student's t-distribution under the null hypothesis, used to determine

if two sets of data are significantly different from each other. By assess whether the means of two groups are statistically different from each other. Here 78 features applied to OD, OC and RNFL, then the relevant features chosen by these two selection methods and resultant into eight features were used in final glaucoma classification.

4.4.7 Classification

The selected features of image represent they are generated from feature selection, are used in glaucoma detecting using classification methods. In this research SVM, KNN and ensembles classifiers were applied to choose the best accuracy like.

4.4.8 Validation and Comparison

The proposed algorithm evaluated using the classifier accuracy, sensitivity and specificity compared by the ground truth attached with the databases, the final validation of the system extract based on classifier outputs, run times and comparison with previous studies at each step: filtering, segmentation and classification via many parameters.

4.4.8.1 Evaluation Parameters

I. **Filters Evaluation Parameters**

To evaluate the performance of these filters 4 parameter applied the original image and filtered image, these parameters are:

- **Mean-Squared Error (*MSE*)**

$$MSE(x,y) = \frac{1}{N}\sum_{i=1}^{N}(x_i - y_i)^2 \qquad (4.19)$$

The error signal $ei = xi - yi$ is the difference between the original and distorted image.

- **Peak Signal to Noise Ratio (PSNR)**

$$\mathrm{PSNR} = 10\log_{10}\ \frac{\mathrm{L}^2}{\mathrm{MSE}} \tag{4.20}$$

Where L is the dynamic range of allowable pixel intensities. For example, for an 8-bit per pixel image, L = 2^8 −1 = 255. L is the dynamic range of allowable image pixel intensities

- **Structural Similarity Index(SSIM)**

$$\mathrm{SSIM(x,y)} = [\mathrm{l(x,y)}]^{\alpha}\,.\,[\mathrm{c(x,y)}]^{\beta}.\,[\mathrm{s(x,y)}]^{\gamma} \tag{4.21}$$

Where it combination of the luminance, contrast and structure similarity functions.

Luminance function: $l(x,y) = \frac{2_{\mu x \mu y} + c_1}{\mu 2_x + \mu 2_y + c_1}$ (4.22)

Contrast function: $c(x,) = \frac{2\sigma_x\,\sigma_y + c_2}{\sigma_x^2 + \sigma_y^2 + c_2}$ (4.23)

Structure function: $s(x,y) = \frac{2\sigma_{xy} + c_3}{\sigma_x \sigma_y + c_3}$ (4.24)

Standard deviation: $\sigma_x = \left(\frac{1}{N-1}\sum_{i-1}^{N}(x_i - \mu_x)^2\right)^{\frac{1}{2}}$ (4.25)

Mean intensity: $\mu_x = \bar{x} = \frac{1}{N}\sum_{i=1}^{N} x_i$ (4.26)

- **Signal-to-Noise Ratio (SNR)**

$$SNR = \frac{P_s}{P_N} = \frac{(Asignal)^2}{(Anoise)^2} \tag{4.27}$$

Where *Asignal* is the signal amplitude and *Anoise* the noise amplitude, (Peter *et al*, 2011).

II. Segmentation Evaluation Parameters

- The Dice similarity coefficient (DSC) was used as a statistical validation metric to evaluate the segmentation and the spatial overlap accuracy, A and B target regions, and is defined as DSC:

  DSC = 2(A∩B)/ (A+B) where ∩ is the intersection (4.28)

- Jaccard similarity coefficient is the Intersection over Union and is a statistic used for comparing the similarity and diversity of images sets with a range of 0% to 100%. The higher the percentage, the more similar in the two image sets, its formula is:

  $$J(A, B) = |A \cap B| / |A \cup B| \quad (4.29)$$

- Structural Similarity (SSIM) Index. The SSIM metric is a combination of local image structure, luminance, and contrast into a single local quality metric. Where, structures represent the patterns of pixel intensities among neighboring pixels, after normalizing for luminance and contrast. The SSIM metric is too close to the human visual system because of the human eye good at perceiving structure.

- $$SSIM(x,y) = [l(x,y)]^{\alpha} . [c(x,y)]^{\beta} . [s(x,y)]^{\gamma} \quad (4.30)$$

$$l(x,y) = \frac{2(1+R)}{1+(1+R)^2+\frac{C_1}{\mu_x^2}} \quad (4.31)$$

$$c(x,y) = \frac{2_{\sigma_x\sigma_y+C_2}}{\sigma_x^2+\sigma_y^2+c_2} \quad (4.32)$$

$$s(x,y) = \frac{\boldsymbol{\sigma_{xy}+C_3}}{\boldsymbol{\sigma_x\sigma_y+C_3}} \quad (4.33)$$

Where $\mu x, \mu y, \sigma x, \sigma y, and\ \sigma xy$ are the local means, standard deviations, and cross-covariance for images x, y. If $\alpha = \beta = \gamma = 1$ (the default for Exponents), and $C_3 = C_2/2$ (default selection of C_3) the index simplifies to:

$$\mathrm{SSIM}(x, y) = \frac{(2\mu_x \mu_y + C_1)(2\sigma_{xy} + C_2)}{(\mu_x^2 + \mu_y^2 + C_1)(\sigma_x^2 + \sigma_y^2 + C_2)} \quad (4.34)$$

III. Classification Evaluation Parameters

The classification are evaluated by two parameters: confusion matrix and ROC curve.

1. Confusion matrix: a plot to understand how the selected classifier performed in each class. The confusion matrix helps you identify the areas where the classifier has performed poorly, the rows show the true class, and the columns show the predicted class. The diagonal cells show where the true class and predicted class match (TP, TN, FP, and FN). If these cells are green and display high percentages, the classifier has performed well and classified, which used to calculate the classifier accuracy, sensitivity, and specificity by the equations:

$$SENSITIVITY = TP/(TP + FN) \quad (4.35)$$

$$SPECIFITY = TN/(FP + TN) \quad (4.36)$$

$$ACCURACY = (TN + TP)/(TN + TP + FN + FP) \quad (4.37)$$

2. ROC Curve: The receiver operating characteristic (ROC) shows the true positive rate (TPR) versus false positive rate (FPR) for the currently selected classifier.

4.4.9 Graphical User Interface

After the algorithm compared with the previous study and confirm the detection algorithm validation the GUI was built to help the doctors to deal with the software and see the final decision and diagnosing steps. A major advantage of the Glaucoma CAD GUI is that they make diagnosis more intuitive, and easier to learn and use.

The graphical user interface show the glaucoma diagnosing decision supported with the image of the optic disc and optic cup segmented part, and selected features values.

CHAPTER FIVE

RESULTS AND DISCUSSIONS

5.1 Introduction

In this chapter the experimental results of the proposed glaucoma detection system discussed and their evaluations are explained in three sections: The **first section** for preprocessing and segmentation, the **second section** for glaucoma detection and the **third section** for glaucoma classification. The key characteristic features used in the research system is color, shape and texture features are the quantitative measure for diagnosing glaucoma. The quantitative evaluation of the proposed system is performed using the computed features compared with the gold standard database diagnosing based on standard parameters discussed in section (2.14). The performance of the OC and OD segmentation is analyzed using the thresholding algorithm. A comparison is also made using the Ensembles and SVM classification approaches. The performance of the glaucoma classification system is evaluated using receiver operating characteristic and area under ROC curve (AUC) for it is the diagnostic ability of binary classifier.

5.2 Section one: Image preparing

5.2.1 Image Preprocessing and Enhancement step

The aim of image enhancement is to improve the interpretability or perception of information included in the image for human viewers and to provide better input for pattern recognition stage, as in Figure [5.1] and Figure [5.2].

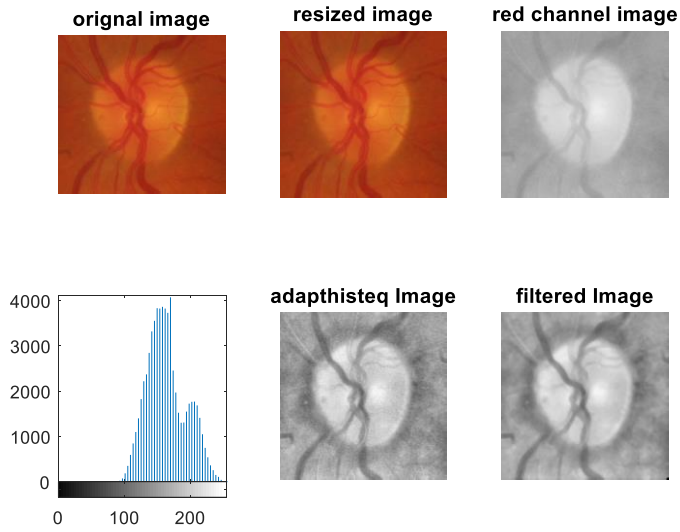

Figure [5.1]: Shows the steps of an image enhancement for healthy image show the original image, image after resized, the channel selected, image histogram (x-axis to show intensity levels and y-axis intensity values), image after histogram equalization and filtered image.

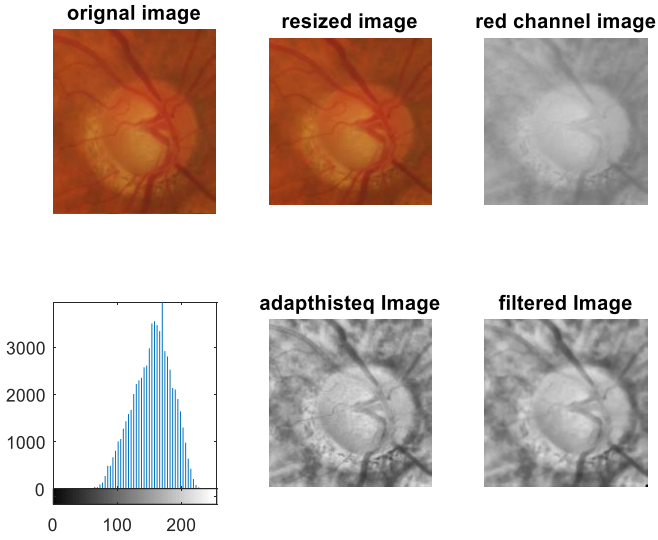

Figure [5.2]: Shows the steps of image enhancement for glaucoma image show the original image, image after resized, the channel selected, image histogram (x-axis to show intensity levels and y-axis intensity values), image after histogram equalization and filtered image.

5.2.2 Channel Separation Results

After the 3 channel extracted (red, green, blue), the best channel was the red channel because it appear good boundary and less blood vessel, which is affecting segmentation accuracy, it used at (Claro M. *et al*.2016) and (Thresiamma *et al*.2015) figure[5.3] shows examples of RGB channels for healthy and glaucoma images.

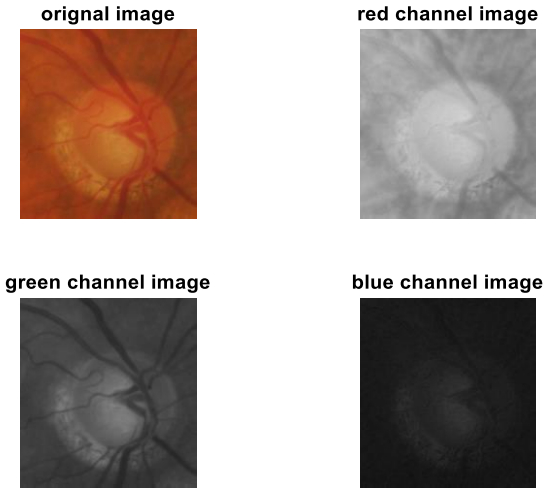

Figure [5.3]: Shows digital fundus image color channels extraction as the red, green and blue channel to select the best one suitable for the segmentation.

5.2.3 Image Noise Filtration Results

To remove the noises from digital fundus images like Gaussian and impulse (salt& papers) noises five filters were applied to the whole database and the output compared based on four parameters, see chapter two page71 after experiments and based on previous studies median filter was the best performance (see section 2.4.6), then the median filter applied to the final algorithm as in Figure [5.4], and the results shows at Figure [5.5], Figure [5.6].

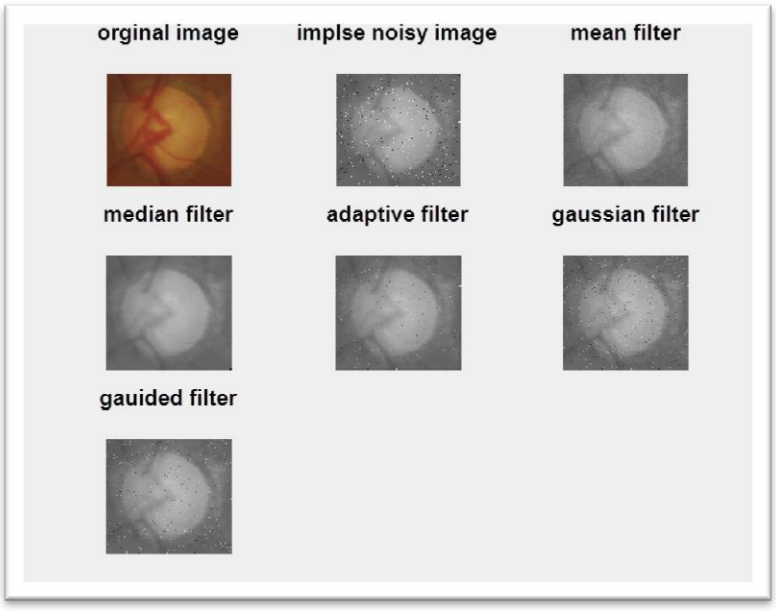

Figure [5.4]: Shows an example of different filters applied in (salt& paper) noisy glaucoma image: the original image, mean, median, adaptive, Gaussian and guided filters.

Table (5.1): Mean value of comparison of PSNR, SNR, SSIM and MSE, parameters to 158 images for Adaptive, Guided, Gaussian, Mean and Median filters in the original image corrupted by Gaussian noise (0.05)

Filters name	**MSE**	**PSNR**	**SNR**	**SSIM**
Mean filter	0.00058	32.38	27.65	0.70
Median filter	0.00040	33.96	29.23	0.81
Adaptive filter	0.00026	36.16	31.42	0.90
Gaussian filter	0.0021	26.87	22.13	0.36
Guided filter	0.00073	31.36	26.62	0.62

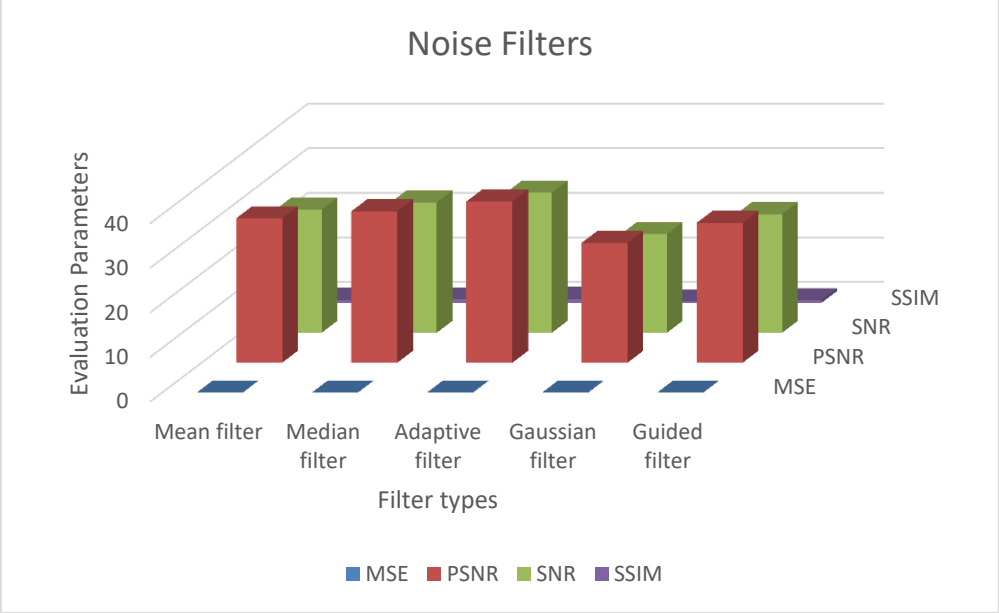

Figure [5.5]: Bar chart show the comparison between the different filters types applied to image corrupted by Gaussian noise.

Table (5.2): Comparison of PSNR, SNR, SSIM and MSE, values for Adaptive, Guided, Gaussian, Mean and Median filters in the original image corrupted by salt& paper noise (0.02).

Filters name	MSE	PSNR	SNR	SSIM
Adaptive filter	0.00093	30.36	25.63	0.80
Guided filter	0.0024	26.24	21.51	0.61
Gaussian filter	0.0023	26.35	21.62	0.59
Mean filter	0.00066	31.84	27.11	0.75
Median filter	**4.96E-05**	**43.48**	**38.75**	**0.97**

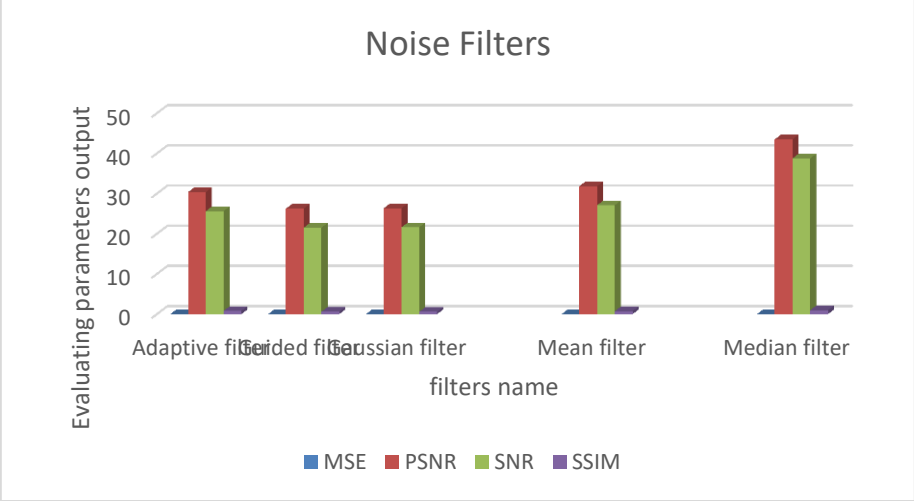

Figure [5.6]: Bar chart show the comparison between the different filters types applied to the original image corrupted by salt &paper noise.

From the evaluation parameters above noticed that, the best performance to impulse noise is median filter and the best for Gaussian noise is an adaptive filter, to get more accurate results the performance of the five filtering methods tested with different noises level, because the noise levels differentiate from one image to others and affected by many factors like patient movement and the results shown in table (5.3), table (5.4), Figure [5.7] and Figure [5.8].

Table (5.3): PSNR evaluating parameter results for different filters applied to Salt & Pepper Noise images at different noise levels.

Salt & pepper Noise%	10 Noise level	20 Noise level	30 Noise level	40 Noise level	50 Noise level
adaptive filter	26.57	24.50	22.86	21.42	20.14
Guided Filter	17.70	13.87	11.73	10.26	9.150
Gaussian filter	19.32	16.25	14.43	13.12	12.10
Mean filter	24.70	21.40	19.37	17.85	16.64
Median Filter	**39.51**	**34.16**	**31.08**	**28.52**	**24.55**

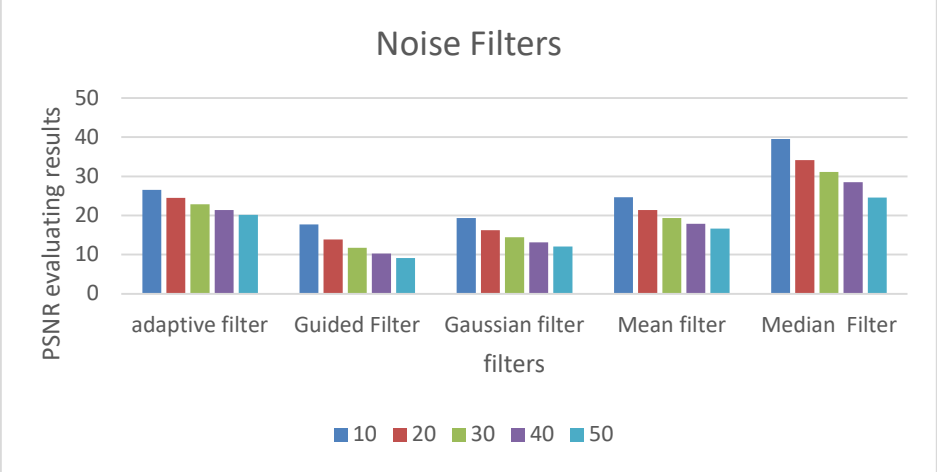

Figure [5.7]: Bar chart shows results of filtration applied to the original image at different level of Salt & Pepper Noise.

Table (5.4): PSNR evaluating parameter results for different filters applied to Gaussian Noise images at different noise levels.

Gaussian noise%	10 Noise level	20 Noise level	30 Noise level	40 Noise level	50 Noise level
Adaptive filter	20.08	14.36	11.23	9.34	8.22
Guided filter	19.17	14.13	11.15	9.30	8.21
Gaussian filter	18.71	13.99	11.08	9.27	8.19
Mean filter	19.73	14.27	11.19	9.32	8.21
Median filter	19.79	14.13	10.98	9.07	7.99

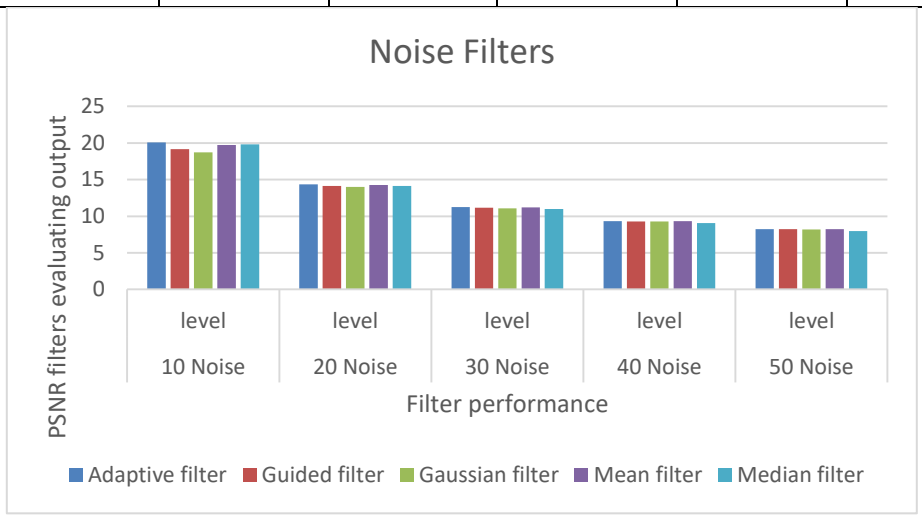

Figure [5.8]: Bar chart shows results of filtration applied to the original image at different level of Gaussian Noise.

Various filtering techniques like linear (Gaussian), nonlinear filtering (mean, median) and adaptive median filtering have been applied. The two main types of noises which includes Gaussian noise and Salt & Pepper noise has been tested, the result was the median filter has the best performance in salt& paper noise at each noise level from 10% until 50% as shown in table (5.3) and in Gaussian noise the median filter and the adaptive filter performance were too close as shown in table (5.4), guided by other studies as (Geetha *et al.* 2017), (Priyadharshini *et al*. 2014), (Anindita Septiarini *et al*. 2018) (Sundari.B *et al.* 2017) (Claro M. *et al.* 2016), and the done experiments median filter has a better performance than other filters in digital fundus images in noise removing and boundary preserve.

5.2.4 Optic Disc Segmentation Step

Optic disc is the pallor circular region located at the position where optic nerve leaves the eye, where Optic cup is the central bright yellowish circular region in optic disc. Optic disc segmentation: The proposed method can be divided into 3 steps, **first step** is vessel remove to get accurate segmentation, and it done by morphological operation, **second step** is thresholding and binarization, and the given image will convert to binary image. From this image optic disc boundary can easily extracted.

The morphological operations are used to smooth the obtained disc and cup boundary, then labeling as binary image to get the disc and cup boundary, **third step** is a disc reconstruction as a circle using center and radius from the detecting region as discussed in chapter three.

Following section describes relevant result to proposed algorithm for segmenting OD structure, Figure [5.9], Figure [5.10] shows the OD segmentation algorithm performance.

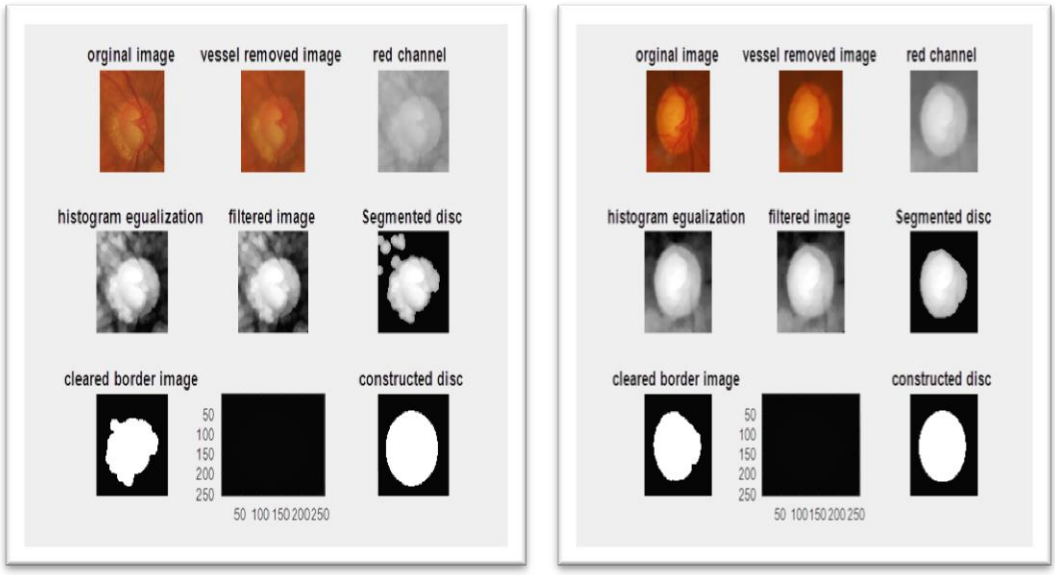

(A) (B)

Figure [5.9]: Show glaucoma image OD segmentation steps as vessel remove, thresholding, post processing and circle reconstruction (A) wrong OD segmentation duo to PPA affect (B) right OD segmentation.

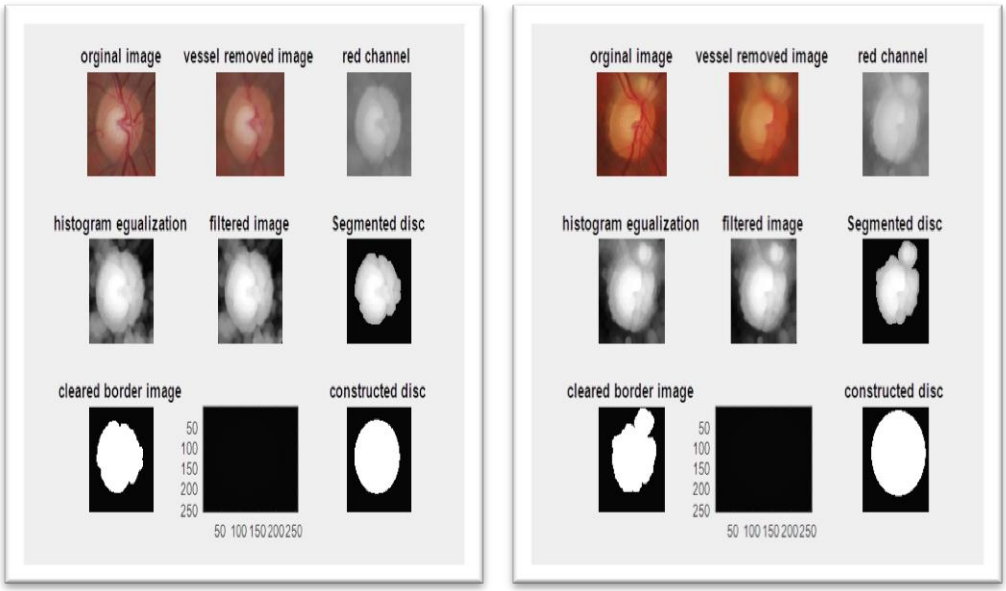

(C) (D)

Figure [5.10]: Shows healthy image OD segmentation steps as vessel remove, thresholding, post processing and circle reconstruction (C) right OD segmentation (D) wrong OD segmentation.

To choose the best OD segmentation methods three segmentation method has been tested and the results are compared with each other, as in Figure [5.11].

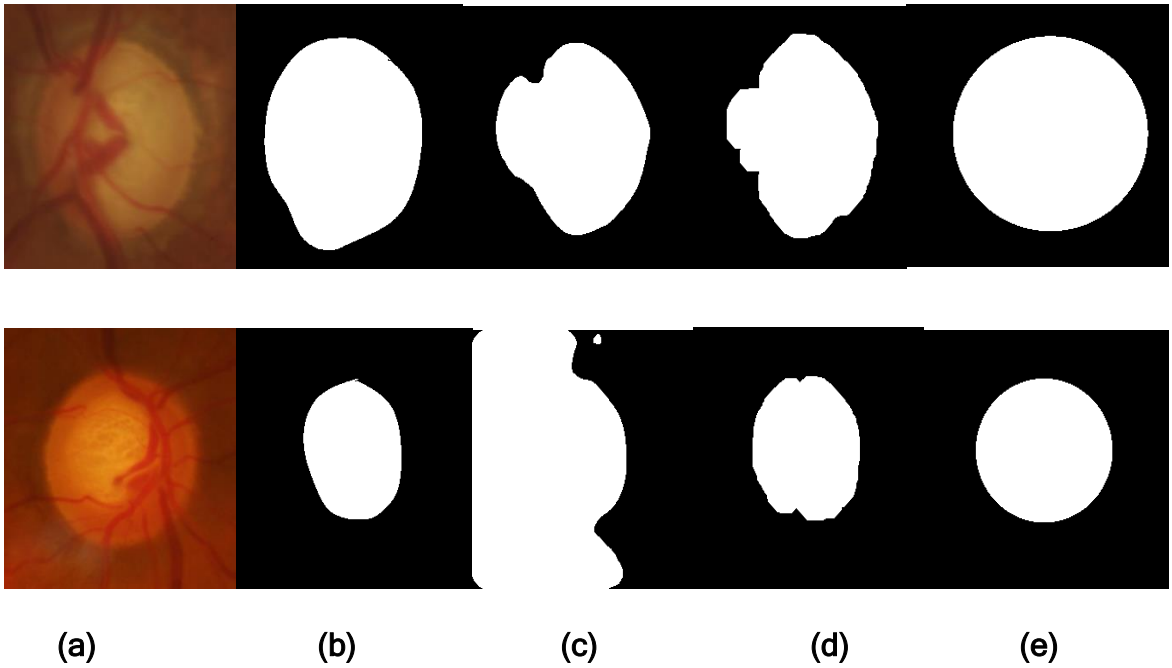

Figure [5.11]: Shows comparison results of different segmentation algorithms (a) Original image (b) ground truth image (c) Otsu Thresholding (d) Global Thresholding (e) Proposed method.

The proposed algorithm evaluated based on many parameters:

The three parameters are: Dice similarity coefficient (DSC), Jaccard coefficient and Structural Similarity (SSIM)), where these parameters are common and accurate in evaluating the segmentation and used in (F. Fumero *et al*.2015) applied to compare the results of the proposed algorithm with the five expert's see section (4.2.1) ground truth segmentation, the results show in table (5.5), and then compared with other segmentation method to evaluate the segmentation algorithm performance, the results shown in table (5.6) and figure [5.12].

Table (5.5): The mean value of the DSC, jaccard coefficient and SSIM acquired using 158 images segmented by proposed method and compared with the five ground truth in the database.

Performance parameters %	Ground truth1	Ground truth 2	Ground truth 3	Ground truth 4	Ground truth 5
DSC	84	88	**90**	87	89
Jaccard coefficient	73	79	**82**	82	81
SSIM	81	83	**83**	82	82

Table (5.6): Comparison of the proposed method against other segmentation methods (Otsu Thresholding, global Thresholding) by same database and same evaluation parameters.

Segmentation Method	DSC%	Jaccard coefficient%	SSIM%
Otsu Thresholding	87	79	82
Global Thresholding	85	75	82
Proposed Method	**90**	**82**	**83**

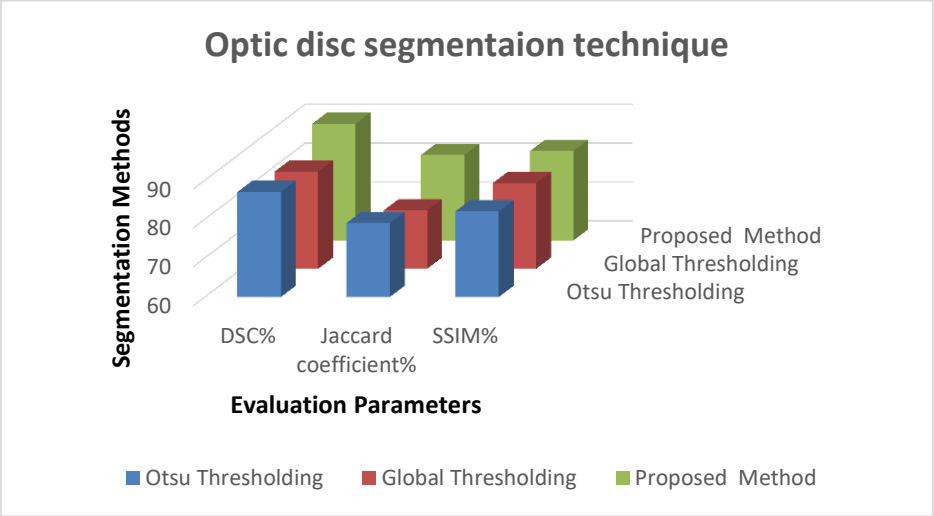

Figure [5.12]: Bar chart show comparison between 3 different types of segmentation applied for disc segmentation to the same database.

Blow some example show the absolute difference between the same segmented images by the proposed method and the ground truth in figure: [5.13] and figure: [5.14].

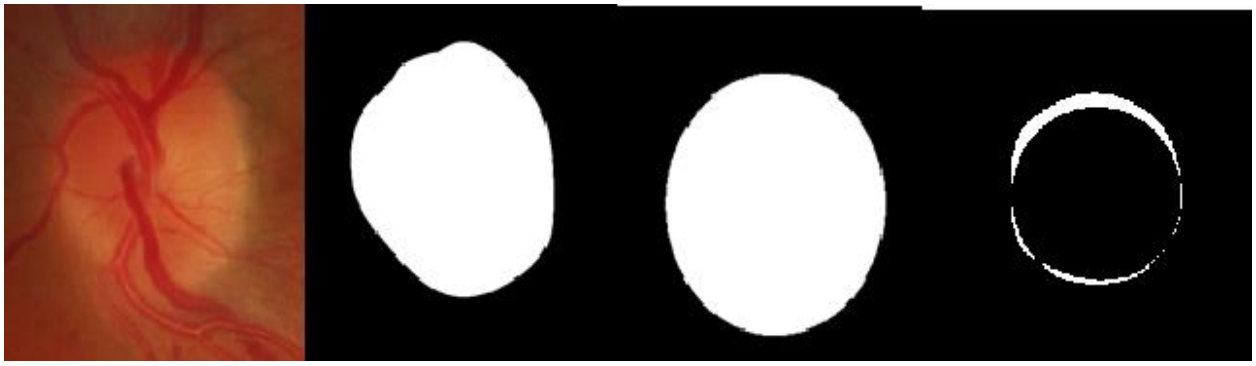

(a) (b) (c) (d)

Figure [5.13]: Shows accurate segmentation (a) the original image (b) ground truth OD (c) proposed OD (d) absolute difference between the two images too small.

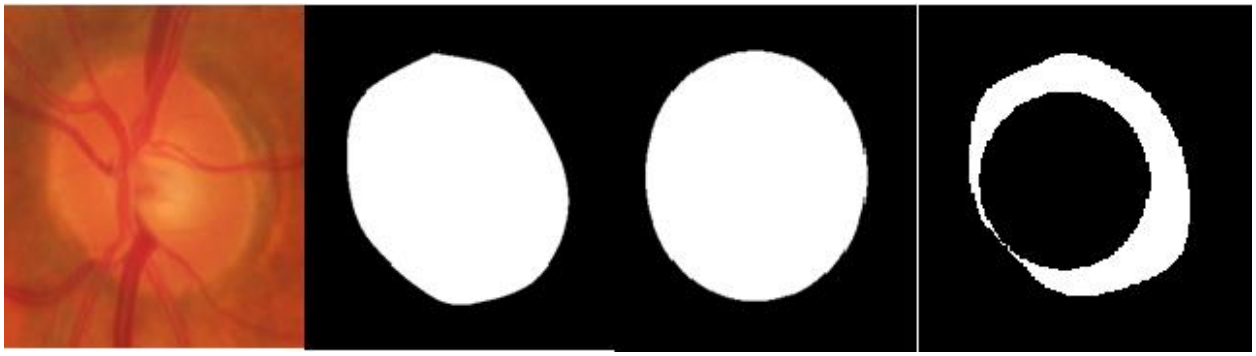

(e) (f) (g) (h)

Figure [5.14]: Shows inaccurate segmentation (e) the original image (f) ground truth OD (g) proposed OD (h) absolute difference between the two images too big.

5.2.4.1 OD discussion

An automatic algorithm for optic disc segmentation are tested before at (Fauzia *et al.* 2013)(Mohd *et al.*2017) , here applied in 185 healthy and glaucoma image 148 image are segmented correctly, the rest 10 are not

segmented duo to non-uniform illumination, main blood vessel and big size of PPA which affect in disc boundary as figure: [5.15].

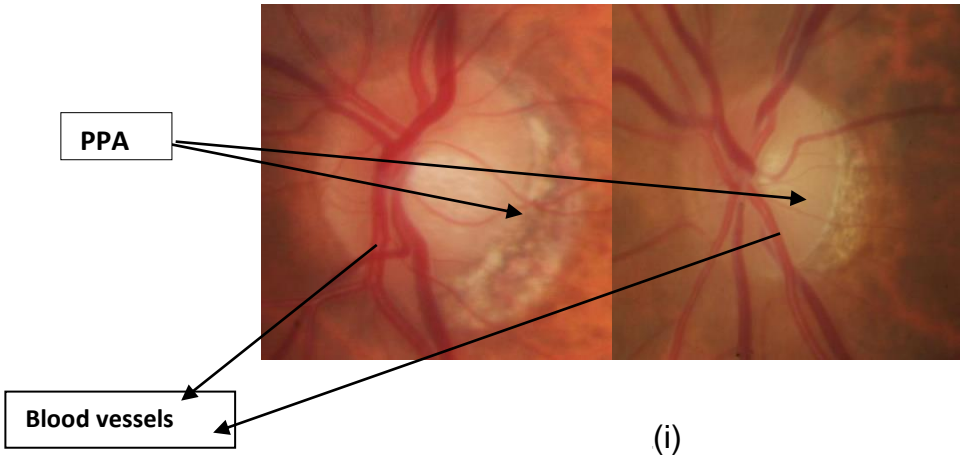

(i) (j)

Figure [5.15]: Shows an example of non-segmented images duo to some reasons like (i) big size PPA (j) non-uniform illumination.

The reason of circle OD reconstruction to remove the affect resultant from main blood vessel, like in Figure [5.16], which appear the segmentations result before the circle step.

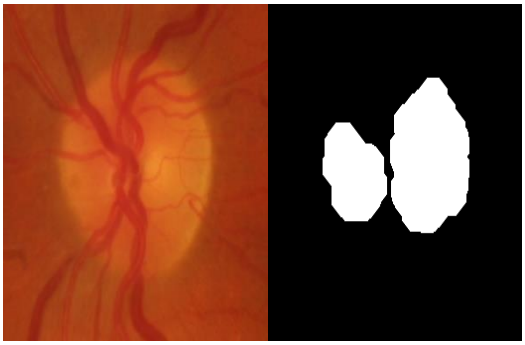

(a) (b)

Figure [5.16]: Shows an example of segmented disc images with main blood vessels (a): original image, (b) segmentation output before circle construction.

The only limitation on this method that each type of image need different thresholding level, in compare with (Sirshad *et al*.2016) which

segmented disc using of gradient extracted from line profiles that pass through optic disc margin the proposed method get good results. In future work other segmentation method will tested to get more accuracy.

In conclusion a new OD segmentation algorithm for digital fundus image has been developed based on rim_one dataset. The ground truth of five ophthalmologists were considered to evaluate the new algorithm. The DSC, jaccard coefficient and SSIM parameters were chosen to evaluate the new system in this paper and founded that the best DSC was 90%, jaccard 82% and SSIM 83%.

5.2.5 Optic Cup Segmentation Step

Cup detection from digital fundus image is one of the challenging tasks as is interfered with the blood vessels based on previous studies the segmentation method are suggested, thresholding from the disc area to get more segmentation accuracy, The optic cup segmentation method proposed, depend on optic disc thresholding at level 240, clear border, smoothing boundary and binaries the final image, the proposed method algorithm shown in chapter four.

In this section, a cup boundary detection algorithm presented and the segmentation results from the digital fundus images evaluated in drishti _GS database an example of the segmentations shown in figure [5.17].

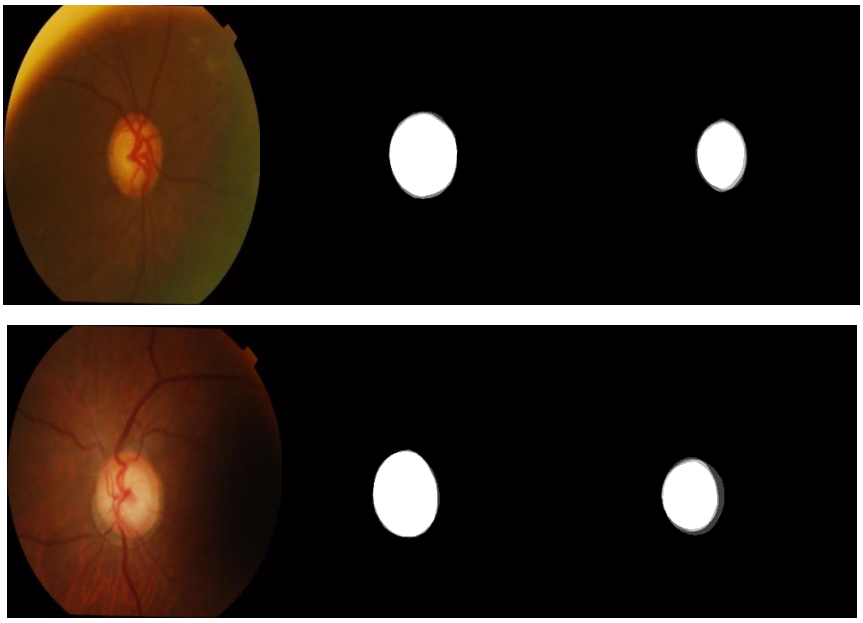

Figure [5.17]: Sample Images and Ground-Truth in Drishti_GS dataset - (From Left to Right) Original image (2047x1751) in the dataset, Ground-truth Optic Disc Mask, proposed segmented Optic Cup Mask.

5.2.5.1 Experimental Results

The proposed cup segmentation method evaluate by 3 parameters, which are: Dice coefficient, jaccard coefficient and SSIM mentioned in section (3.3) and the results were compared with other methods like super pixel segmentation method, modified super pixel, modified thresholding and the best results obtained by global thresholding technique as shown in Figure [5.18] and Figure [5.19].

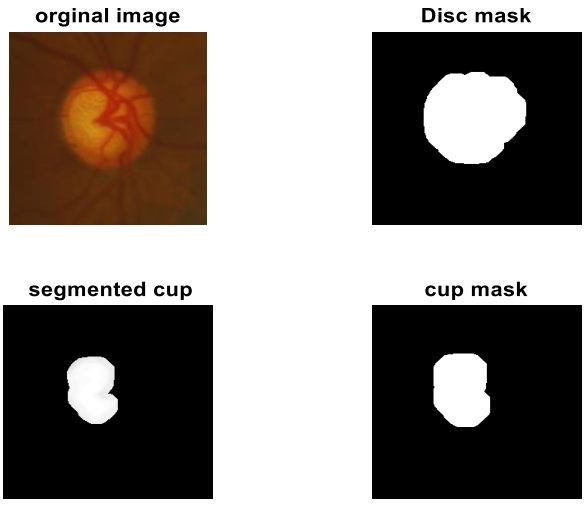

Figure [5.18]: Shows a cup segmentation and binarization from the disc part for glaucoma image using global thresholding technique.

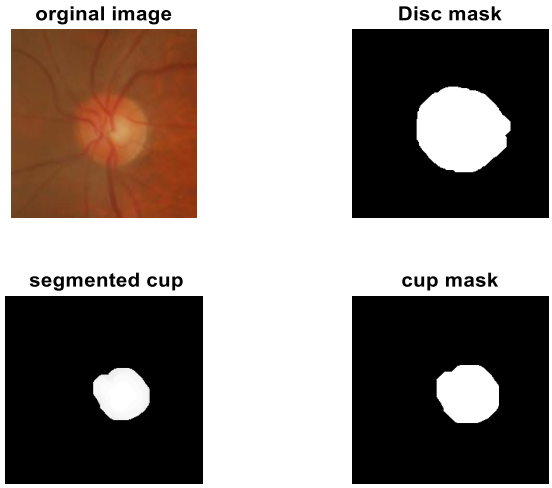

Figure [5.19]: Shows a cup segmentation and binarization from the disc part for healthy image using global thresholding technique.

The cup segmentation using global thresholding technique applied and compared with other segmentation techniques, the results evaluated based on standard parameters and shown in Figure [5.19] and Figure [5.21].

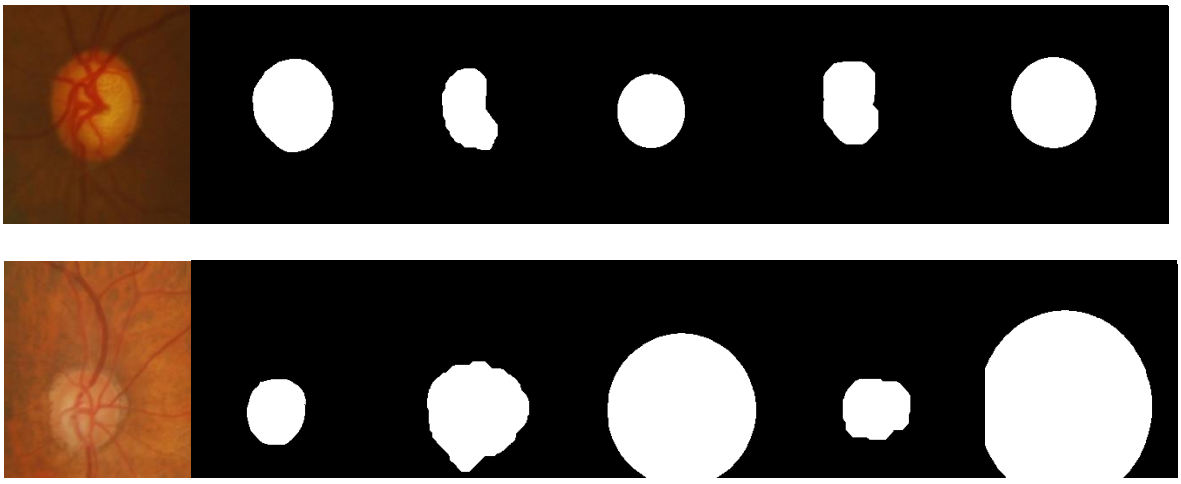

(a) (b) (c) (d) (e) (f)

Figure [5.20]: Shows (a) the original image (b) ground truth image (c) super pixel segmentation (d) super pixel segmentation with circle construction (e) global thresholding (f) global Thresholding segmentation with circle construction.

Table (5.7): Comparison of the proposed method against other segmentation methods (Super pixel segmentation, global Thresholding, Super pixel with circle construction and Global with circle construction) by same database and same evaluation parameters.

Segmentation method	**DSC%**	**Jaccard coefficient%**	**SSIM%**
Super pixel segmentation	66	52	90
Super pixel with circle construction	58	45	83
Global Thresholding (proposed)	**73**	**60**	**93**
Global with circle construction	53	39	80

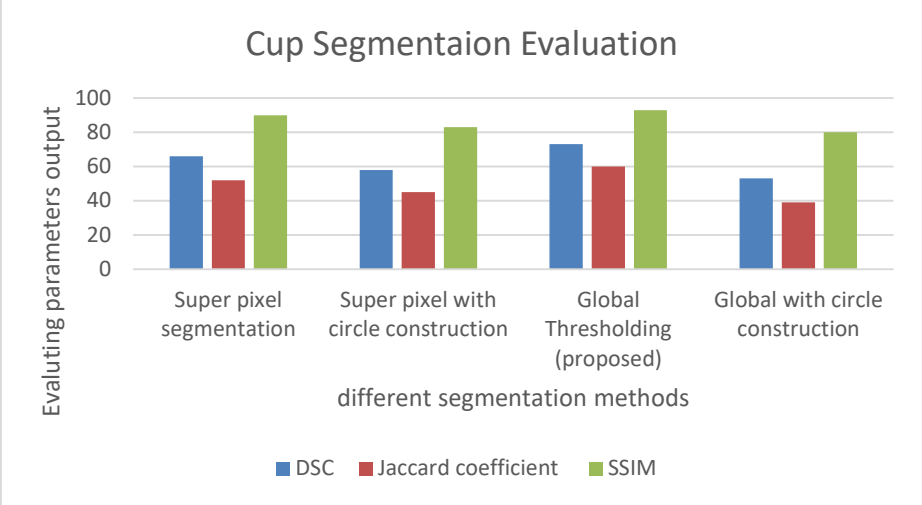

Figure [5.21]: Bar chart illustrates the comparison between different segmentation techniques.

5.2.5.2 OC Discussion

Although experimentally, it was demonstrated that the use of global thresholding can help improve the optic cup detection, however, it should be noted that there are some limitations and considerations for the effective use of global thresholding for cup boundary detection. Like the thresholding level differentiate from one data base to another. Even for images in one database, there were several instances of detection failure can be attributed to an accurate detection of the optic disc as a form of initialization for the optic cup detection. Figure [5.22] is an example of un-segmented images due to bad localization of the ROI region.

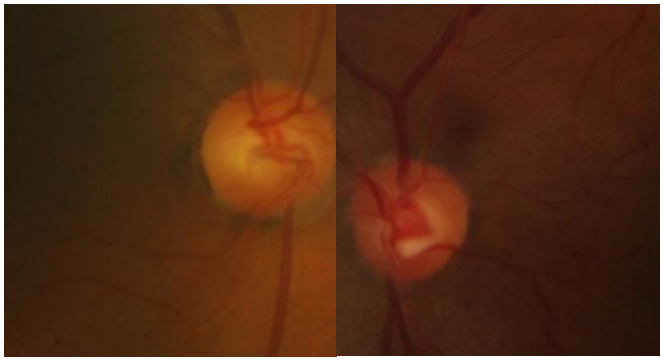

Figure [5.22]:An examples of un segmented image duo to ROIbad localization

In conclusion this section has presented model to localize the optic cup in retinal images. The framework provides two major contributions. Firstly, robust and stable optic cup localization is presented. Secondly, the accuracy, simplicity and inexpensive computation mothod proposed. Experimentally, it was demonstrated that this method is able to produce optic cup localization with high accuracy.

5.2.6 RNFL ROI Extraction Step

The RNFL (retinal nerve fiber layer) is the area surrounded the disc for the ROI determines based on mathematical method to subtract the whole image form disc area, by the formula:

$$RNFL = ROI\ image - OD \quad (5.1)$$

Where the ROI image represent the ONH part, OD is the optic disc after circle reconstruction step, the results shown Figure [5.23] and Figure [5.24].

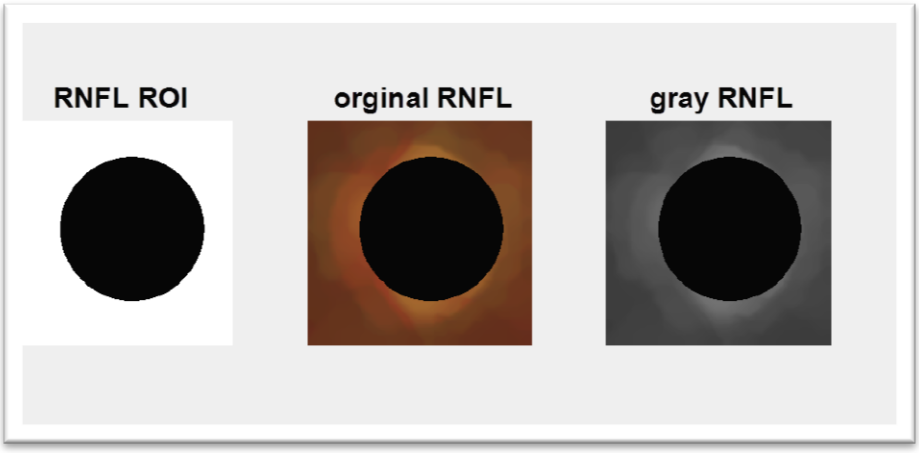

Figure[5.23]: Shows RNFL for glaucoma image,which is apart surrounded the disc.

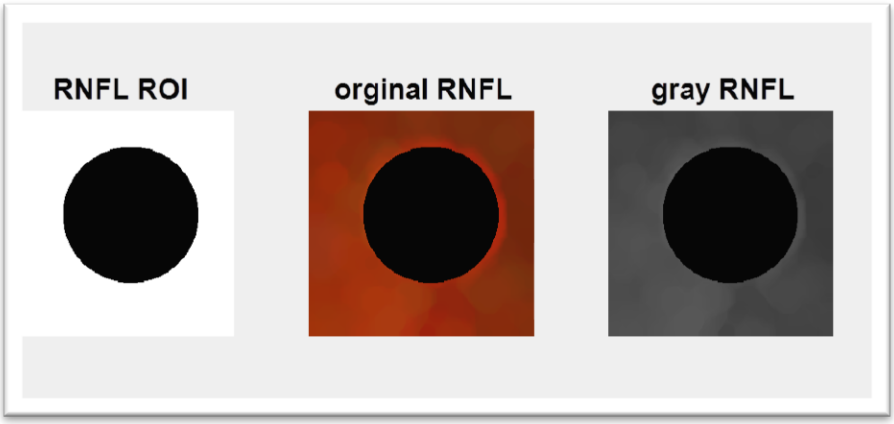

Figure[5.24]: Shows RNFL for healthy image, extracted by substract the optic nerve head from the segmented optic disc.

The OD, OC and RNFL are used for the third step, which is feature extraction, selection and the final step is the classifications.

5.3 Section two: Glaucoma detection

5.3.1 Feature Extraction Step

Depend on ophthalmologist observation glaucoma is diagnosed by examination of size, structure, shape and color of optic nerve head and RNFL. Based on this theory a combination of size, structure, shape features are applied to disc, cup and RNFL to classify glaucoma from non-glaucoma cases, this feature are:

5.3.1.1 Shape Features

Measures several properties describe shape for each disc and cup within region props function. Which computes Area, Convex area, Eccenterity, Centroid, Filled Area, Filled Image, Extent, Major Axis Length, Minor Axis Length, Solidity, radius and Perimeter, these measurements applied for disc and cup masks and the results shown in Table (5.8) and Table (5.9),which calculated by matlab 2016.

Table (5.8): Illustrates an examples of the cup shape features for only 10 image.

onex.are	ECC.	EQ.DIA	EXTENT	F.AREA	MAJ.axis	MIN.axis	OREN	PER.	SOLD.	C.AREA	C.center	c.centery
7734	0.51365	98.2921	0.79017	7588	106.713	91.5592	-36.166	314.046	0.98112	7588	139.057	125.206
8545	0.61837	103.338	0.84717	8387	117.596	92.417	79.3882	337.334	0.98151	8387	112.914	122.86
8979	0.65156	104.386	0.7703	8558	121.962	92.5199	-59.811	348.068	0.95311	8558	149.857	110.953
8352	0.54682	102.017	0.80931	8174	112.217	93.9534	47.6436	328.262	0.97869	8174	120.66	130.916
8462	0.52967	102.905	0.79971	8317	112.108	95.0897	-51.553	329.172	0.98286	8317	140.109	122.702
8602	0.65355	102.887	0.75438	8314	119.375	90.353	-42.763	341.826	0.96652	8314	142.535	116.383
8559	0.55092	103.682	0.80517	8443	113.797	94.9702	59.6989	329.85	0.98645	8443	98.7616	117.397
8079	0.6285	100.717	0.86786	7967	114.812	89.3026	-85.403	323.48	0.98614	7967	98.9665	127.523
8594	0.48608	103.59	0.83545	8428	112.069	97.9385	27.3424	336.904	0.98068	8428	110.236	120.323
8605	0.51489	103.866	0.80665	8473	112.913	96.7953	52.5652	332.24	0.98466	8473	115.999	100.395

Where cup features are: CON= convex area, EQU= equivalent diameter, EX=extent, MAJ= major axes, MIN= minor axes, OR= orientation, PER= perimeter, SOL=solidity, F.AREA= filled area, ECC= Eccenterity.

Table (5.9): Illustrates an examples of the disc shape features only for only 10 images.

D.AREA	D.center	D.center	d.rad.	D.CON	D.ECC	D.EQU	D.EX	D.F.ARE	D.MAJ.A	D.MIN.A	D.OR	D.PER	D.SOL	D.RAD
18582	132.25	128.139	96.1361	18705	0.04091	153.816	0.78352	18582	153.885	153.756	-20.743	480.392	0.99342	56.0946
16430	126.982	127.648	90.4076	16546	0.03836	144.635	0.78145	16430	144.693	144.587	-15.293	451.918	0.99299	64.1524
17955	129.304	118.283	94.5063	18069	0.02812	151.199	0.78747	17955	151.233	151.173	-46.992	471.94	0.99369	78.6076
17700	122.841	126.364	93.8218	17809	0.02418	150.121	0.78667	17700	150.147	150.103	-85.056	468.392	0.99388	59.7453
16800	123.275	115.251	91.414	16901	0.02691	146.255	0.78814	16800	146.286	146.233	51.2652	456.21	0.99402	60.8713
19378	135.66	115.769	98.1773	19497	0.024	157.076	0.78616	19378	157.103	157.058	-53.318	490.49	0.9939	65.1853
18543	113.516	120.333	96.014	18663	0.02615	153.654	0.78188	18543	153.685	153.632	8.29331	480.02	0.99357	63.8804
18901	112.982	127.223	96.972	19015	0.04101	155.131	0.78672	18901	155.2	155.069	-5.2522	484.122	0.994	71.229
17614	124.792	124.994	93.6193	17722	0.0375	149.756	0.7881	17614	149.813	149.708	7.91116	467.54	0.99391	59.0958

Where disc feature are: CON= convex area, EQU= equivalent diameter, EX=extent, MAJ= major axes, MIN= minor axes, OR= orientation, PER= perimeter, SOL=solidity, F.AREA= filled area, ECC= Eccenterity.

All these shape features applied to the t-test to obtain the most significance features based on, If P-value < α = 0.10, and acceptance the null hypothesis at α > 0.10 mean that there is no significance difference between variables.

Final results from Table (5.10) shown that, there is significance 95% in the cup minor axes and disc solidity features calculated using SPSS software.

Table (5.10): Shows the t-test results from the shape features.

Variables	Pictures	N	Mean	Std. Dev	Std. E. M	F	t.	df	P.Value
C.CONEX.ARE	Infect	36	8.73	1.01	1.7	0.029	0.841	151	0.402
	Control	117	8.57	9.95	9.16				
C.ECC	Infect	36	0.55	0.132	0.02	0.108	1.209	151	0.229
	Control	117	0.58	0.134	0.01				
C.EQ.DIA	Infect	36	1.04	4.17	0.71	0.25	0.934	151	0.352
	Control	117	1.03	5.58	0.51				
C.EXTENT	Infect	36	0.88	0.044	0.01	0.526	0.718	151	0.474
	Control	117	0.813	0.039	0				
C.F.AREA	Infect	36	8.48	7.19	1.22	0.113	0.909	151	0.365
	Control	117	8.34	8.48	7.81				
C.MAJ. AXES	Infect	36	1.16	1.15	1.95	0.005	0.245	151	0.807
	Control	117	1.17	1.25	1.15				
C.MIN. AXES	Infect	36	9.49	4.96	0.839	2.24	1.937	151	0.03
	Control	117	9.25	6.99	0.643				
C.OREN	Infect	36	1.63	5.93	1	4.695	0.739	151	0.461
	Control	117	7.03	6.72	6.18				
C.PER	Infect	36	3.41	4.15	7.02	0.868	0.777	151	0.438
	Control	117	3.36	3.02	2.78				
C.SOLD	Infect	36	0.974	0.025	0.004	0.935	0.11	151	0.912
	Control	117	0.975	0.022	0.002				
C.AREA	Infect	36	8.48	7.2	1.25	0.113	0.909	151	0.365
	Control	117	8.34	8.48	7.81				
C.CENTERX	Infect	36	1.23	1.99	3.38	0.004	0.96	151	0.339
	Control	117	1.27	2.11	1.95				
C.CENTRY	Infect	36	1.23	1.16	1.95	1.667	0.031	151	0.975
	Control	117	1.23	1.1	1.01				
D.AREA	Infect	36	1.87	1.31	2.22	5.881	0.932	151	0.353
	Control	117	1.83	2.68	2.47				
D.CENTERX	Infect	36	1.23	1.01	1.71	0.636	-0.394	151	0.165
	Control	117	1.26	9.62	0.886				
D.CENTRY	infect	36	1.25	8.06	1.36	0.002	0.611	151	0.542
	control	117	1.24	8.49	0.78				
D. Rad	infect	36	9.65	3.36	0.57	5.891	1.065	151	0.289
	control	117	9.51	7.33	0.67				
D.CON	infect	36	1.88	1.32	2.22	5.891	0.478	151	0.633
	control	117	1.84	2.69	2.48				
D.ECC	infect	36	0.034	0.009	0.002	0.018	1.063	151	0.29
	control	117	0.033	0.01	0.001				
D.EQU	infect	36	1.54	5.36	0.907	5.809	0.929	151	0.354
	control	117	1.52	1.17	1.08				
D.EX	infect	36	0.785	0.002	0	0.359	0.333	151	0.74
	control	117	0.785	0.003	0				
D.F.AREA	infect	36	1.87	1.31	2.22	5.881	0.932	151	0.353
	control	117	1.83	2.68	2.47				
D.MAJ. AXES	infect	36	1.54	5.37	0.91	5.893	1.063	151	0.29
	control	117	1.52	1.17	1.08				
D.MIN. AX	infect	36	1.54	5.36	0.906	5.924	1.062	151	0.29
	control	117	1.52	1.17	1.08				
D.OR	infect	36	8.81	4.86	8.22	0.391	0.265	151	0.792
	control	117	6.17	5.26	4.84				
D.PER	infect	36	4.82	1.68	2.83	0.94	1.057	151	0.292
	control	117	4.75	3.68	3.39				
D.SOL	infect	36	0.994	0	0	0.667	1.881	151	0.05
	control	117	0.993	0	0				
D.RADF	infect	36	6.59	7.46	1.26	0.069	0.058	151	0.954
	control	117	6.58	1.26	1.157				

From the table above, there is one significance features is cup minor axes, the results shown in figure: [5.25].

Table (5.11): The selected shape features for the glaucoma and healthy images.

Digital fundus images	Cup minor axes	Disc Solidity
Glaucoma	9.500	0.9936
Healthy	9.300	0.9934

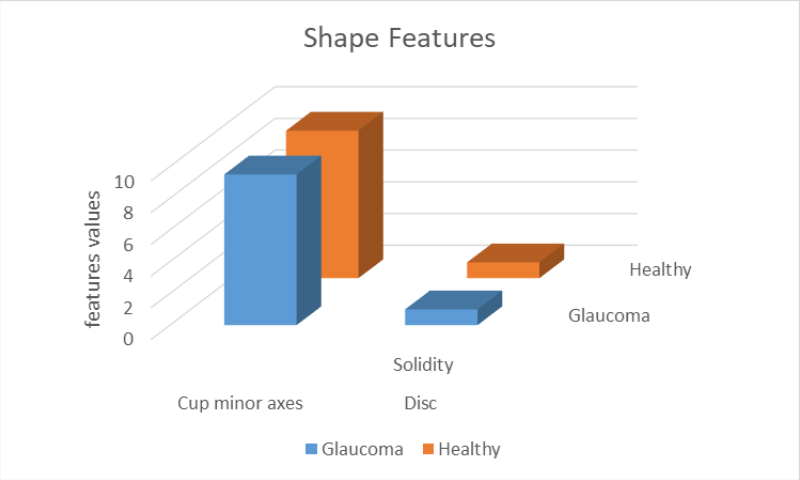

Figure [5.25]: Bar chart shows the cup minor axes and disc solidity for 40 glaucoma images and 118 healthy images.

5.3.1.2 Color Features

Color moments are measures that characterize color distribution in an image in the same way that central moments uniquely describe a probability distribution. Color moments are mainly used for color indexing purposes as features in image retrieval applications in order to compare how similar two images are based on color. Three color moments are computed per channel, 9 color feature are computed for each disc, cup and RNFL, and these features are mean, standard deviation and skewness (discussed in chapter two), the results shown in Table (5.12), Table (5.13) and Table (5.14).

Table (5.12): Illustrates an examples of cup color features for only 10 images.

c.meanb	c.meang	c.meanr	c.skb	c.skg	c.skr	c.stdb	c.stdg	c.stdr
7.90181	14.04892	25.24249	2.54386	2.584084	2.404483	22.1806	39.739	69.77914
2.095688	6.543976	20.08339	3.411929	3.216952	2.308777	6.225212	19.49272	52.90643
3.247665	9.007523	24.59483	2.953466	2.960921	2.244194	9.116987	25.84778	63.83207
6.937469	12.54155	26.21092	2.51523	2.579697	2.28106	18.89293	34.56495	69.50961
7.721024	14.27969	27.55458	2.402646	2.493259	2.247769	20.61168	38.68851	72.32332
5.842834	11.70863	28.78789	2.402344	2.591936	2.247194	15.61646	32.33374	75.5673
7.676926	14.33311	28.8349	2.314811	2.432832	2.223449	20.20122	38.46927	75.04939
9.216797	17.28461	29.37224	2.45051	2.486167	2.320597	25.1438	47.55311	78.99562
1.488968	6.372147	21.9944	2.648844	2.648259	2.252229	4.063342	17.53406	57.46885

Where c.meanb =cup mean for blue channel, c.meanr =cup mean for red channel, c.meang =cup mean for green channel, c.skg =cup skewness for green channel, c.skb =cup skewness for blue channel, c.skr =cup skewness for red channel, c.stdb =cup standard deviation for blue channel, c.stdr =cup standard deviation for red channel, c.stdg =cup standard deviation for green channel.

Table (5.13): Illustrates an examples of disc color features for only 10 images

d.meanb	d.meang	d.meanr	d.skb	d.skg	d.skr	d.stdb	d.stdg	d.stdr
17.1859	29.90857	59.43636	1.124948	1.203953	0.970426	27.99239	49.53667	94.62551
3.295288	10.19006	36.144	2.453966	2.314909	1.250022	6.786466	21.20881	63.38452
5.321747	14.44046	47.60818	1.981302	2.051152	1.088901	9.934429	28.00284	78.38685
13.0538	22.90872	54.23773	1.324543	1.456071	1.053684	22.40908	40.51896	89.41003
14.08235	25.14478	53.6949	1.295621	1.433597	1.127204	24.59974	45.04688	91.60313
12.40031	24.27518	64.02541	1.054549	1.256858	0.919114	19.62002	40.14743	99.20396
15.58417	28.00774	61.20389	1.10117	1.264006	0.975914	25.36398	47.18262	97.61609
19.25354	34.67758	67.4584	1.100833	1.234245	0.941758	30.99066	57.50805	106.0853
2.514542	10.77719	42.26846	1.640288	1.662586	1.103177	4.523128	19.78077	70.34166
13.42873	30.08844	61.62369	1.306984	1.273518	0.914804	22.03509	49.87152	95.05968

Where d.meanb =disc mean for blue channel, d.meanr =disc mean for red channel, d.meang =disc mean for green channel, d.skg =disc skewness for green channel, d.skb =disc skewness for blue channel, d.skr =disc skewness

for red channel, d.stdb =disc standard deviation for blue channel, d.stdr =disc standard deviation for red channel, d.stdg =disc standard deviation for green channel.

Table (5.14): Illustrates an examples of RNFL color features for only 10 images

rn.meanb	rn.meang	rn.meanr	rn.skb	rn.skg	rn.skr	rn.stdb	rn.stdg	rn.stdr
33.04367	57.96133	120.3777	-0.83114	-0.72161	-0.8025	21.19177	37.83722	77.59473
5.337463	21.27376	65.88588	0.850968	-0.24513	-0.3573	4.217105	14.15665	43.54503
6.793976	24.85201	74.96664	-0.07356	-0.24647	-0.28198	4.911454	17.02542	51.91936
29.0159	48.4364	111.5854	-0.89974	-0.63104	-0.72413	18.00881	31.37594	71.37176
32.28215	55.11308	116.7324	-0.86873	-0.50372	-0.71537	19.63159	35.34451	73.0528
25.38705	47.01894	117.8963	-0.75201	-0.55826	-0.62252	16.82775	32.11181	79.7713
32.25183	57.31044	112.6929	-0.83092	-0.61262	-0.55602	20.68434	38.04992	75.70935
39.45503	67.35126	129.4043	-0.8721	-0.66921	-0.66616	25.34794	44.59389	85.97335
3.712463	23.88306	84.02716	-0.62445	-0.82495	-0.84809	2.41081	14.94325	52.42571
19.39464	37.93088	104.9089	-0.75676	-0.44336	-0.51614	12.88353	26.37245	72.68975

Where rn.meanb =RNFL mean for blue channel, rn.meanr =RNFL mean for red channel, rn.meang =RNFL mean for green channel, rn.skg =RNFL skewness for green channel, rn.skb =RNFL skewness for blue channel, rn.skr =RNFL skewness for red channel, rn.stdb =RNFL standard deviation for blue channel, rn.stdr =RNFL standard deviation for red channel, rn.stdg =RNFL standard deviation for green channel.

SPSS software applied to the color features at the above tables to choose the most significance features using the t-test method, the results shown in Table (5.15),and illustrate there are five significance color features cup mean, cup STD, disc mean, disc STD, and RNFL STD shown in Figure:[5.26].

Table (5.15): Shows the t-test results from the color features.

Variables	Pictures	N	Mean	Std. D.	S.E.M	F	t.	df	P.Value
c.meanb	Infect	35	6.22	2.6	0.44	0.225	0.786	151	0.433
	control	118	6.76	3.79	0.35				
c.meang	Infect	35	12.19	3.48	0.59	0.332	0.121	151	0.904
	control	118	12.11	3.67	0.34				
c.meanr	Infect	35	26.16	3.31	0.56	0.22	2.588	151	0.011
	control	118	24.35	3.72	0.34				
c.stdb	Infect	35	16.66	6.86	1.16	0.041	0.853	151	0.395
	Control	118	18.2	9.95	0.92				
c.stdg	Infect	35	32.15	8.99	1.52	0.528	0.099	151	0.922
	Control	118	32.97	9.31	0.86				
c.stdr	Infect	35	68.07	8.22	1.39	4.303	2.802	151	0.012
	Control	118	63.77	7.9	0.73				
c.skb	Infect	35	2.54	0.32	0.05		0.516	151	0.607
	Control	118	2.57	0.37	0.03				
c.skg	Infect	35	2.59	0.27	0.05		0.08	151	0.936
	Control	118	2.58	0.27	0.02				
Cskr	Infect	35	2.23	0.13	0.02		0.998	151	0.32
	Control	118	2.27	0.22	0.02				
d.meanb	infect	35	12.32	5.64	0.95	0.1	0.466	151	0.642
	control	118	12.97	7.64	0.7				
d.meang	infect	35	23.4	8.02	1.35	0.198	0.277	151	0.782
	control	118	22.96	8.37	0.77				
d.meanr	infect	35	55.1	9.15	1.55	3.293	2.33	151	0.021
	control	118	50.61	10.23	0.94				
d.skb	infect	35	1.35	0.4	0.07	0.3	0.914	151	0.362
	control	118	1.43	0.46	0.04				
d.skg	infect	35	1.44	0.35	0.06	0.072	0.157	151	0.875
	control	118	1.45	0.36	0.03				
d.skr	infect	35	0.99	0.12	0.02	0.305	1.261	151	0.209
	control	118	1.04	0.26	0.02				
d.stdb	infect	35	20.2	8.67	1.47	0.021	0.646	151	0.519
	control	118	21.6	11.94	1.1				
d.stdg	infect	35	39.53	11.85	2	4.23	0.25	151	0.803
	control	118	38.97	11.75	1.08				
d.stdr	infect	35	87.29	12.4	2.1	3.002	2.81	151	0.01
	control	118	81.13	11.08	1.02				
rn.meanb	infect	35	21.64	11.34	1.92	0.026	0.264	151	0.792
	control	118	20.99	13.15	1.21				
rn.meang	infect	35	41.75	14.86	2.51	1.417	0.523	151	0.602
	control	118	40.26	14.74	1.36				
Rnmeanr	infect	35	101.61	20.25	3.42	0.659	1.226	151	0.222
	control	118	97.33	17.47	1.61				
rn.skb	infect	35	0.49	0.45	0.08	1.96	1.564	151	0.12
	control	118	0.05	1.65	0.15				
rn.skg	infect	35	0.48	0.25	0.04	3.151	0.856	151	.393.
	control	118	0.42	0.41	0.04				
rn.skr	infect	35	0.64	0.18	0.03	3.632	1.392	151	0.166
	control	118	0.7	0.25	0.02				
rn.stdb	infect	35	14.43	7.29	1.23	6.844	0.113	151	0.91
	control	118	14.25	8.46	0.78				
rn.stdg	infect	35	28.31	9.94	1.68	1.914	0.674	151	0.501
	control	118	27.08	9.38	0.86				
Rnstdr	infect	35	67.48	12.97	2.19	0.755	2.019	151	0.07
	control	118	63.12	10.65	0.98				

Table (5.16): Illustrates the mean values of the selected color features for both 40 glaucoma and 118 healthy images.

Digital fundus image	Cup (mean)	Cup (STD)	Disc (mean)	Disc (STD)	RNFL (STD)
Glaucoma	26.04	67.71	54.78	86.85	67.08
Healthy	24.38	63.84	50.66	81.20	63.20

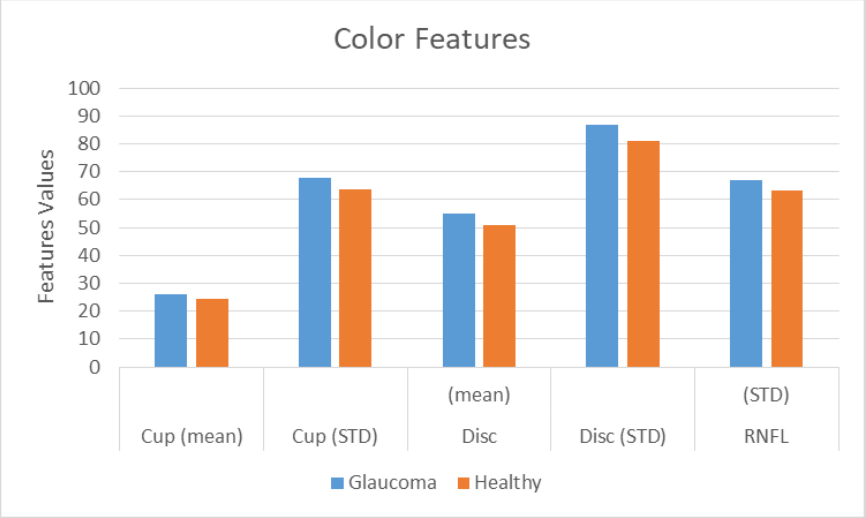

Figure [5.26]: Bar chart of selected color features for 40 glaucoma images and 118 healthy images.

5.3.1.3 Texture Features

GLCM and Tamara algorithms can be used to describe the main features of the textures such as coarseness and regularity. Gray-Level Co-occurrence matrices measure is one of the most important measures that can be used to describe the texture of the RNFL, the feature obtained are 22 feature from the GLCM at 32 quantization levels based on (Sakthivel *et al.* 2014) and 3 features from Tamara algorithm (coarseness, direction and contrast),the results shown in Table (5.17) .

Table (5.17): Illustrates an examples of RNFL texture features for only 10 images

coar.	cont	dir.	v1	v10	v11	v12	v13	v14
38.41763	40.69872	0.782514	8	0.828125	0.8075	0.714286	14.42212	4.625
38.46411	17.86302	0.062312	8.125	0.953125	0.9475	0.839286	11.05884	3.875
37.43988	21.51254	0.788693	8.125	0.953125	0.9475	0.839286	11.05884	3.875
38.7186	35.12054	0.788262	7.875	0.84375	0.825	0.732143	13.30103	4.5
38.84473	37.03552	0.79052	7.875	0.84375	0.825	0.732143	13.30103	4.5
38.18777	38.56587	0.807517	10.375	0.8125	0.79	0.660714	16.66431	5.25
38.31445	40.5225	0.780941	8	0.828125	0.8075	0.714286	14.42212	4.625
38.37451	46.92262	0.785659	9.375	0.796875	0.7725	0.660714	16.66431	5.125
38.84955	20.58708	-4.59394	7.125	0.9375	0.93	0.839286	9.937744	3.75
38.29657	33.39359	0.761134	8.875	0.859375	0.8425	0.732143	14.42212	4.625

Where, Coar. = coarseness, Cont. = contrast, Dir. = direction, V1= Energy V10= Cluster Prominence, V11= Maximum probability, V12 = Sum of Squares, V13 = Sum Average, V14 = Sum Variance.

After applied the t-test for the texture features, found that there is no significance difference, after that and based on previous studies (chapter three) proven that the texture are affected by the glaucoma disease. The SFS method discussed at chapter two are applied and coarseness feature are selected.

Table (5.18): Shows the t-test results from the texture features.

Variables	Pictures	N	Mean	Std. Dev.	S.E.M.	F	t.	df	P.Value
Coar	infect	36	3.84	0.42	0.07	8.815	0.951	151	0.343
	control	117	3.85	0.85	0.08				
Cont.	infect	36	3.28	9.04	1.53	1.289	1.282	151	0.202
	control	117	3.07	8.04	0.74				
Dir.	infect	36	3.47	1.27	0.21	0.005	0.299	151	0.765
	control	117	2.64	1.49	0.14				
v1	infect	36	7.95	1.57	0.27	2.646	1.171	151	0.243
	control	117	7.54	1.88	0.17				
v10	infect	36	8.66	0.05	0.01	3.032	0.124	151	0.901
	control	117	8.67	0.04	0				
v11	infect	36	8.5	0.06	0.01	3.032	0.124	151	0.901
	control	117	8.51	0.05	0				
v12	infect	36	7.54	0.07	0.01	0.472	0.65	151	0.517
	control	117	7.61	0.06	0.01				

v13	infect	36	1.32	2.59	0.44	0.084	0.826	151	0.41
	control	117	1.28	2.6	0.24				
v14	infect	36	4.38	0.56	0.09	0.01	0.925	151	0.356
	control	117	4.28	0.55	0.05				
v15	infect	36	3.35	6.3	1.06	0.648	1.112	151	0.268
	control	117	3.21	6.97	0.64				
v16	infect	36	7.02	0.13	0.02	0.863	0.542	151	0.588
	control	117	6.9	0.11	0.01				
v17	infect	36	7.5	3.04	0.51	0.032	0.124	151	0.901
	control	117	7.44	2.47	0.23				
v18	infect	36	4.13	0.12	0.02	4.83	0.176	151	0.86
	control	117	4.15	0.09	0.01				
v19	infect	36	2.16	0.16	0.03	3.19	0.935	151	0.351
	control	117	1.9	0.14	0.01				
v2	infect	36	7.5	3.04	0.51	3.032	0.124	151	0.901
	control	117	7.44	2.47	0.23				
v20	infect	36	3.1	0.12	0.02	0.433	0.875	151	0.383
	control	117	3.8	0.11	0.01				
v21	infect	36	9.29	0.03	0	3.032	0.124	151	0.901
	control	117	9.29	0.02	0				
v22	infect	36	9.34	0.03	0	3.032	0.124	151	0.901
	control	117	9.34	0.02	0				
v3	infect	36	4.79	0.18	0.03	1.505	0.866	151	0.388
	control	117	4.52	0.16	0.01				
v4	infect	36	4.79	0.18	0.03	1.505	0.866	151	0.388
	control	117	4.52	0.16	0.01				
v5	infect	36	1.77	370.37	62.6	0	1.101	151	0.273
	control	117	1.69	367.51	33.83				
v6	infect	36	1.47	28.95	4.89	0.065	1.016	151	0.311
	control	117	1.41	27.82	2.56				
v7	infect	36	1.07	0.43	0.07	3.032	0.124	151	0.901
	control	117	1.06	0.35	0.03				
v8	infect	36	5.96	0.09	0.02	0.994	0.567	151	0.571

	control	117	6.05	0.08	0.01				
v9	infect	36	7.95	0.18	0.03	1.907	0.392	151	0.696
	control	117	0.78	0.14	0.01				

Table (5.26): Shows the selected feature by SFS method

Digital fundus image	RNFL Coarseness
Glaucoma	38.3
Healthy	38.5

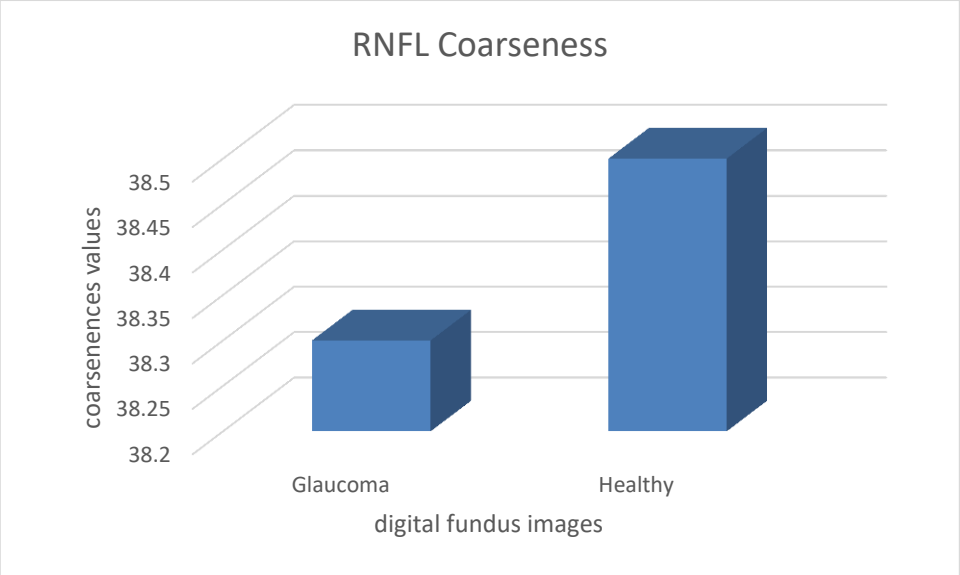

Figure [5.27]: Shows the difference means between the glaucoma and healthy RNFL coarseness feature.

5.3.1.4 Combined Features

From the above section, glaucoma disease can detect form fundus image via eight features (Cup mean, Cup STD, Cup minor axes, Disc mean, Disc STD, Disc Solidity, RNFL STD and RNFL coarseness).

R= 0.245, R^2= 60%, where R represent the effect of the features on the glaucoma by 60%.

The glaucoma linear regression

= 419.460+ OD mean.×3.962 + OC mean × -2.329 + OD STD × 0.340 + OC STD × -2.794 +OC minor axis × 0.309 +RNFL coarseness × -1.201

Where mean, standard deviation, minor axes and coarseness are explained in sections (2.8.6), (2.9.1), (2.9.2), and (2.11.1).

5.4 Section Three: Classification

The classification performance assessment done with Receive Operating Characteristics (ROC) Curve, a binary classification model classifies each instance into one of two classes; say *glaucoma* and a *non-glaucoma* class. This gives rise to four possible classifications for each instance: a true positive (TP), a true negative (TN), a false positive (FP), or a false negative (FN). This situation can be depicted as a confusion matrix (also called contingency table) given in Figure [5.28]. The confusion matrix illustrates the observed classifications for a phenomenon (columns) with the predicted classifications of a model, (rows). In Figure [5.35], the classifications that lie along the major diagonal of the table are the correct classifications, that is, the true positives and the true negatives. The other fields signify model errors. For a perfect model the true positive and true negative fields will be filled out, the other fields will be zero. The performance metrics can be calculated from the confusion matrix fields.

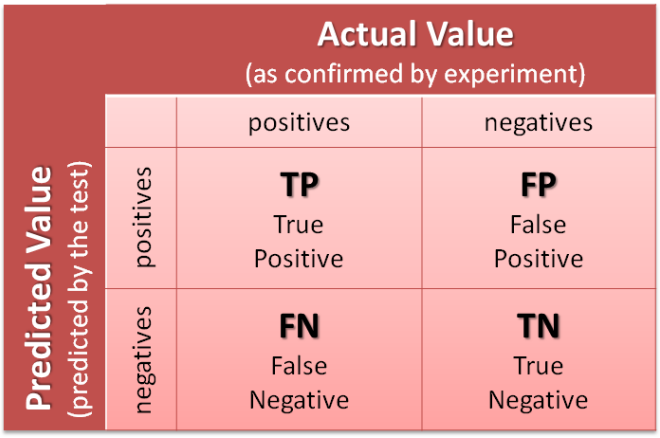

Figure [5.28]: Format of a confusion matrix

ROC curves were originally designed as tools to visually determine optimal operating points for the classifier. Two new performance metrics need to be introduced to construct ROC curves (defined here in terms of the confusion matrix), the true positive rate (TPR) and the false positive rate (FPR).

ROC graphs are constructed by plotting the true positive rate (TPR) against the false positive rate, Figure [5.29] Identify a number of regions of interest in a ROC graph. The diagonal line from the bottom left corner to the top right corner show the classifier performance. To the left bottom of the random performance line as a performance region, as the classifiers in this region shows few false positive errors. In the extreme case, denoted by the point in the bottom left corner, a conservative classification model will classify all instances as negative and it will not commit any false positives but it will also not obtained any true positives. The region of classifiers performance appears at the top of the graph. These classifiers have a good true positive rate but also have numbers of false positive errors. When the classifier at the top right corner that means it classifies every instance as positive. In this situation, the classifier will not miss any true positives but it will also miss a very large number of false positives. If the classifiers fall in

the right of the random performance line, mean it has a performance worse than random performance, due to it produce more false positive than true positive responses. However, because ROC graphs are symmetric along the random performance line the point in the top left corner denotes perfect classification: 100% true positive rate and 0% false positive rate.

Figure [5.30] shows some typical examples of ROC curves. Part (a) depicts the ROC curve of an almost perfect classifier where the performance curve almost touches the 'perfect performance' point in the top left corner. Part (b) and part (c) depict ROC curves of inferior classifiers.

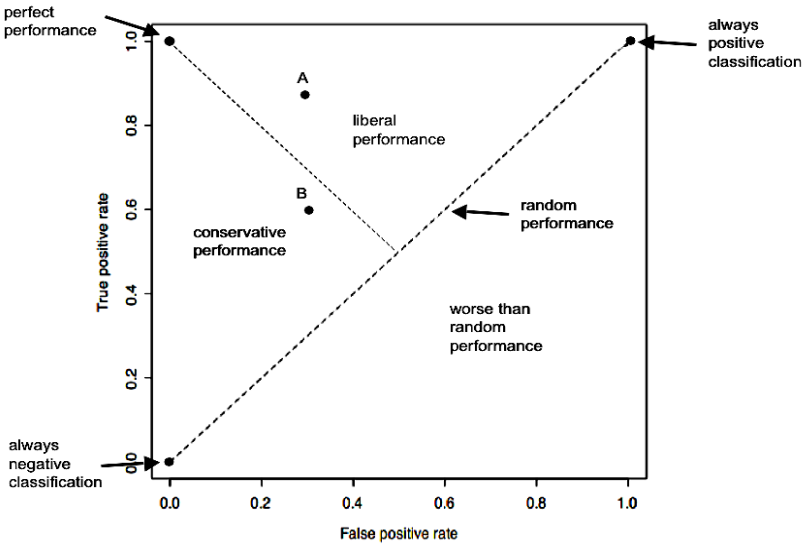

Figure [5.29]: ROC curve: regions of a ROC graph

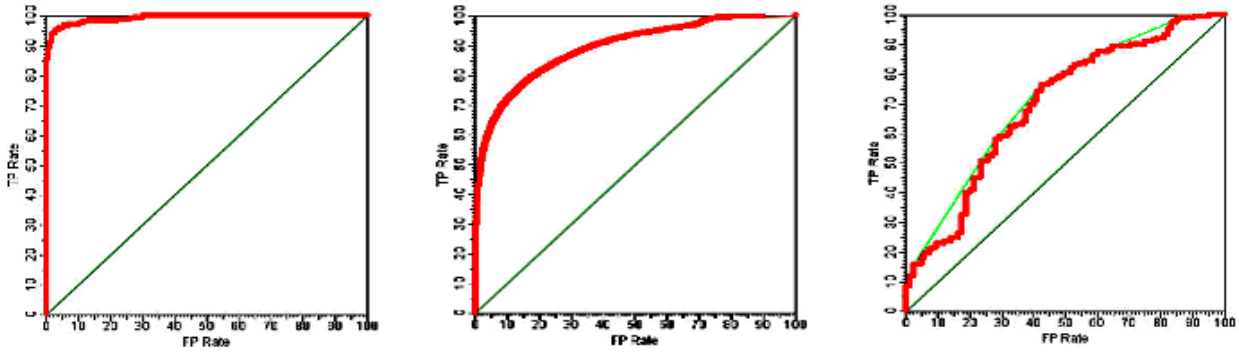

Figure [5.30]: ROC curves: (a) an almost perfect classifier (b) a reasonable classifier (c) a poor classifier

Here, the ROC curves used for checking the performance of classifiers to distinguish between normal and glaucoma fundus images, using the ROC curve parameters like sensitivity, specificity, and accuracy. Where Sensitivity indicates the number of subjects who have glaucoma and are accurately identified by the positive test. Thus, it is a measure of the probability of correctly diagnosing images. Specificity indicates the number of normal subjects are accurately identified by the negative test. Thus, it is a measure of the probability of correctly distinguishing the healthy images. The accuracy represents by the area under the curve (AUC), where it represents the expected performance of a classifier and the equivalent probability to randomly chosen positive instance higher than a randomly chosen negative instance.

• **True positive (TP)** is the number images detected as glaucoma by an expert and the proposed method.

• **True negative (TN)** is the number of images detected as non-glaucoma by an expert and the proposed method.

• **False positive (FP)** is the number of images detected as non-glaucoma by an expert but detected as glaucoma by the proposed method.

• **False negative (FN)** is the number of images detected as glaucoma by an expert but detected as non-glaucoma by the proposed method.

5.4.1 Shape features classification

The selected features are cup minor axes and disc solidity, these features are evaluated by many classifiers like SVM, KNN, ensembles bagging classifier and ensembles boosting classifier discussed in (section 2.13), the classification result in Figure [5.31] show best result using SVM, which are accuracy 76.5% and AUC 0.052.

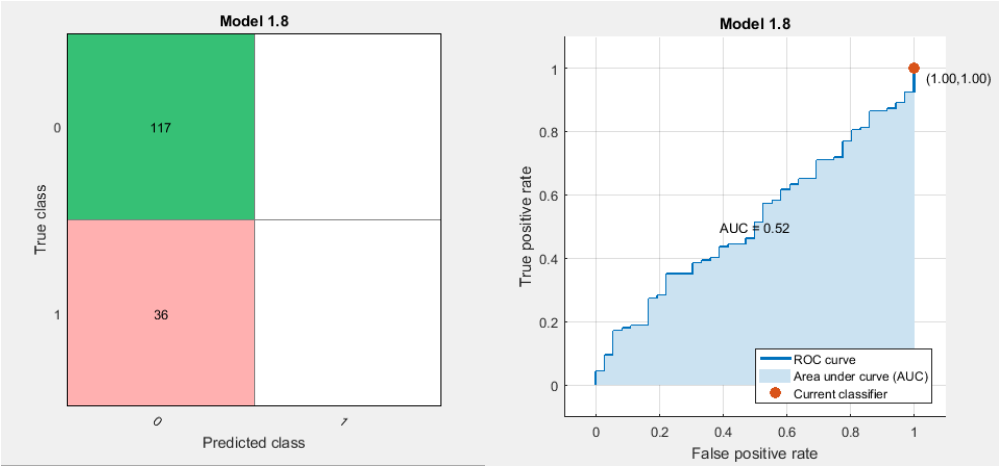

Figure [5.31]: Shows confusion matrix and ROC curve results from the shape selected features.

From the above results TP, TN, FP and FN=117, 0, 0 and 36 respectively, noticed that the healthy image are correctly classified (117) and all glaucoma image are misclassified (36 of 36) duo to imbalanced features (When examples of one class in a training data set vastly outnumber examples of the other class, traditional data mining algorithms tend to create suboptimal classification models), to solve this problem the smote a logarithm discussed at (section 2.14) same technique used before at (kumar *et al.* 2012),(Alghamdi *et al*.2017) and (Yuan *et al*.2015) were applied smote a logarithm to balance the features, here the balanced features are classified again and the results shown in Figure:[5.32] and get TP, TN, FP and FN=40, 134, 15 and 7 respectively, better accuracy 88.8% and AUC 0.93 by ensembles bagging tree at 5 folds cross validation.

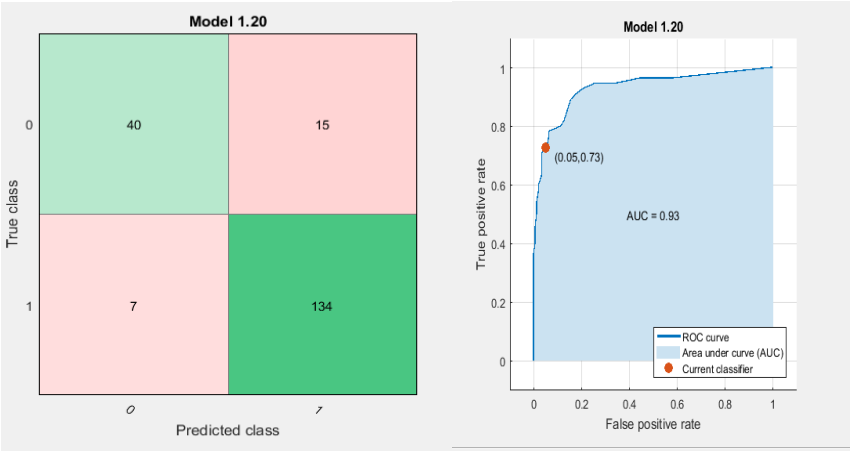

Figure [5.32]: Shows confusion matrix and ROC curve results from the shape balanced features at 5 folds cross validation.

Then the classifier cross validation value change to 10 to get more accuracy, at 10 folds cross validation by same improved selected feature the classification results in Figure:[5.33] are accuracy 91.3% and AUC 0.92 by ensemble RUSBOOSTED tree classifier.

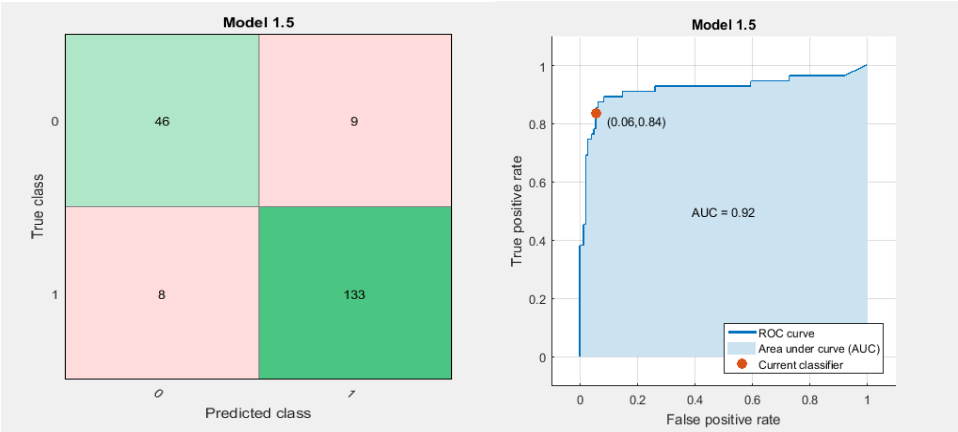

Figure [5.33]: Shows confusion matrix and ROC curve results from the shape balanced features at 10 folds cross validation.

The shape features classification error rate was an 8.7%, because the OD and OC segmentation accuracy due to main blood vessel and big size of PPA which affect in disc boundary and cup segmentation.

5.4.2 Color features classification

The selected features were five features are: cup mean and standard deviation, disc mean and standard deviation, and RNFL standard deviation these five features are classified by 3 types of classification are SVM, KNN and ensembles classification the result in Figure [5.34] as TP, TN, FP and FN=117, 1, 1 and 34 respectively, evaluated and get accuracy 77.1% and AUC 0.68 by SVM.

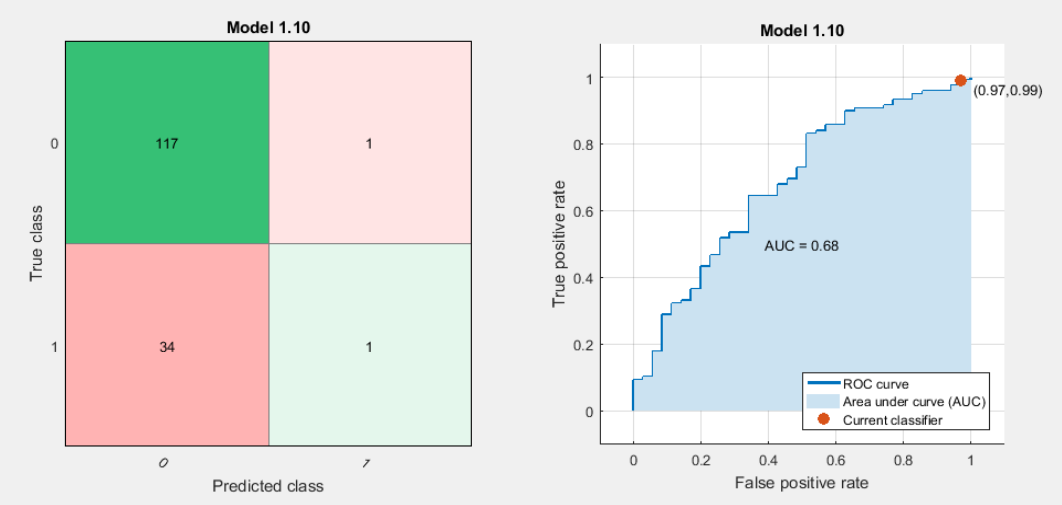

Figure [5.34]: Shows confusion matrix and ROC curve results from the color selected features at 5 folds cross validation.

Noticed that the same problem as in the shape features and solved by the same way in the previous section, and the classification result in Figure:[5.35], TP, TN, FP and FN=57, 133, 17 and 8 respectively, to the balanced feature are accuracy 88.4% and AUC 0.94 at 5 folds cross validation by ensembles subspace KNN.

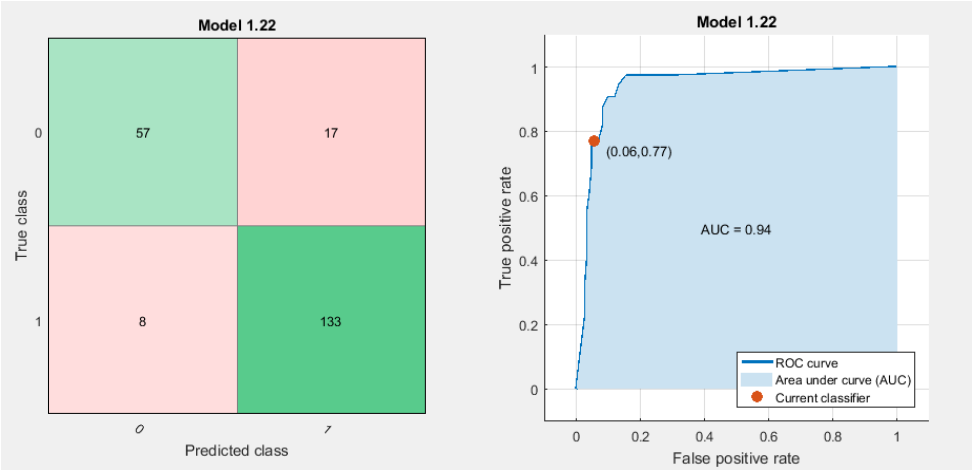

Figure [5.35]: Shows confusion matrix and ROC curve results from the color balanced features at 5 folds cross validation.

Then the classifier cross validation value change to 10 to get more accuracy, at 10 folds cross validation from Figure: [5.36] the TP, TN, FP and FN=65, 136, 9 and 5 respectively, the accuracy was 93.5% and AUC 0.96 by ensembles subspace KNN.

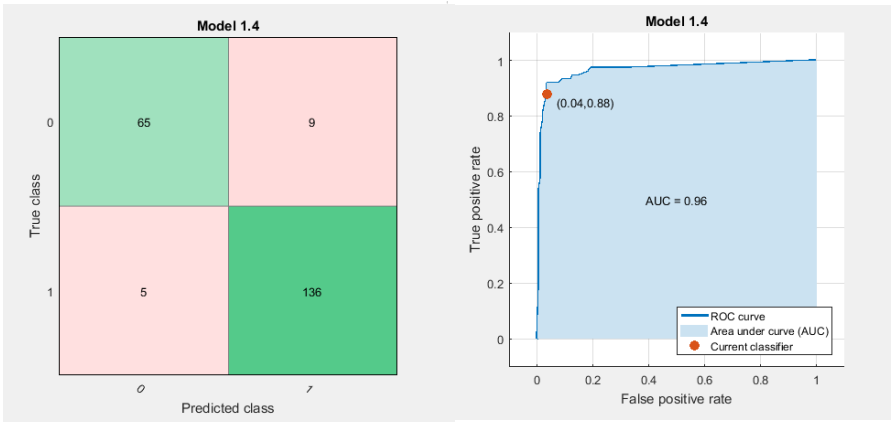

Figure [5.36]: Shows confusion matrix and ROC curve results from the color balanced features at 10 folds cross validation.

The color features classification error rate was 6.5%, due to non-uniform illumination happen in the peripheral part of the retina which often appears darker than the central region because of the curved retinal surface and the geometrical configuration of the light source and camera. These interferences

affect the illumination of the ONH and would have an influence to the subsequent statistical analysis in captured fundus images, compared with (Abir Ghosh *et al.* 2015), which used the grid color technique to detect glaucoma and obtained accuracy 87.47% there is a good improve in accuracy result from applying color features in specific regions (OD, OC).

4.5.3 Texture features classification

The 25 features extracted from the RNFL using GLCM and Tamara algorithm are then selected by sequential feature selector (SFS) discussed in chapter two to get the most relevant feature is the coarseness finally entered this feature to classifier Figure [5.37] and obtained TP, TN, FP and FN=116, 0, 0 and 37 respectively, 75.8% accuracy and 0.44 AUC by the SVM classifier.

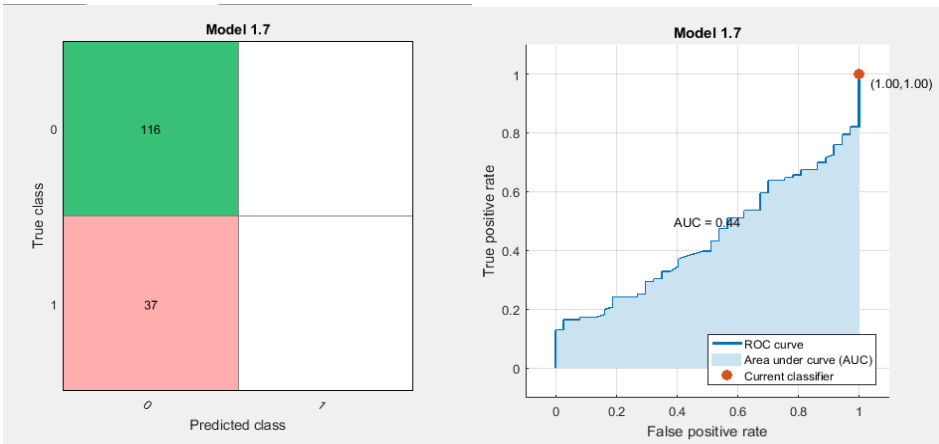

Figure [5.37]: Shows selected features confusion matrix and ROC curve classification results from the texture at 5 folds cross validation.

After balanced the features by the smote algorithm, the classification results Figure:[5.38] improved to be TP, TN, FP and FN=54, 128, 10 and 17 respectively, accuracy 87.1% and AUC 0.90 by ensembles boosted tree, ensembles subspace KNN and ensembles RUSBoosted tree at 5 fold cross validation.

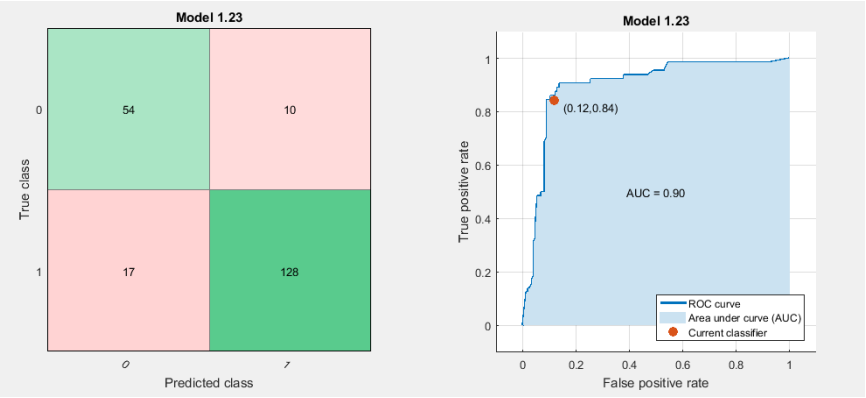

Figure [5.38]: Shows confusion matrix and ROC curve results from the texture balanced features at 5 folds cross validation.

Then the classifier cross validation value change to 10 to get more accuracy, at 10 fold cross validation Figure: [5.39] the results TP, TN, FP and FN=53, 134, 11 and 11 respectively, accuracy was 89.5% and the AUC 0.93 by ensembles RUSBoosted.

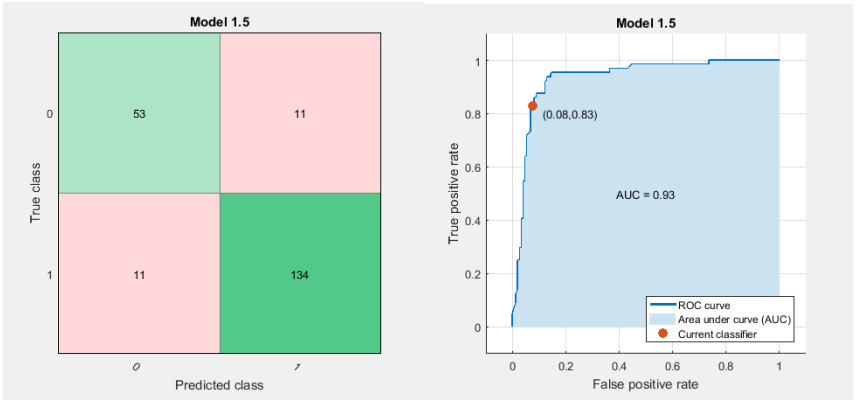

Figure [5.39]: Shows confusion matrix and ROC curve results from the texture balanced features at 10 folds cross validation.

The texture features classification errors can equal 10.5 can explained as, in advanced glaucoma or optic atrophy RNFL defects cannot be detected, since the mean intensity of the RNFL is low in all directions and a localized lesion is not distinguishable. However, in these cases, the pathologic features of disc cupping or atrophy are clearer than RNFL defects, and can easily be detected, , and can easily be detected but compared with (MORRIS *et al.*2015)

who used the Binary Robust Independent Elementary Features (BRIEF) as a texture features to detect the glaucoma and achieved AUC 0.84, and (Maya *et al.*2014) detected glaucoma by local texture features and achieves 95.1% success rate with a specificity of 92.3% and a sensitivity of 96.4%, which better than texture features presented in this research duo to 2 reasons: the first one the database used is a small and the texture features extracted from the whole image therefore the suggested method more better in glaucoma detection.

Where the matlab code used to extract Tamara texture features are get from free available matlab file exchange side coded by (Sudhir Sornapudi,2014), and the GLCM feature coded by (Avinash Uppuluri,2008).

4.5.4 Combined features classification

To get better accuracy, all selected features which are (disc sodality, mean and standard deviation and cup minor axes, mean and standard deviation and RNFL standard deviation and coarseness) are combined together the final classification results Figure: [5.40] was TP, TN, FP and FN=65, 143, 5 and 1 respectively, accuracy 97.2% and AUC 1.00 at 5 fold cross validation by SVM classifier.

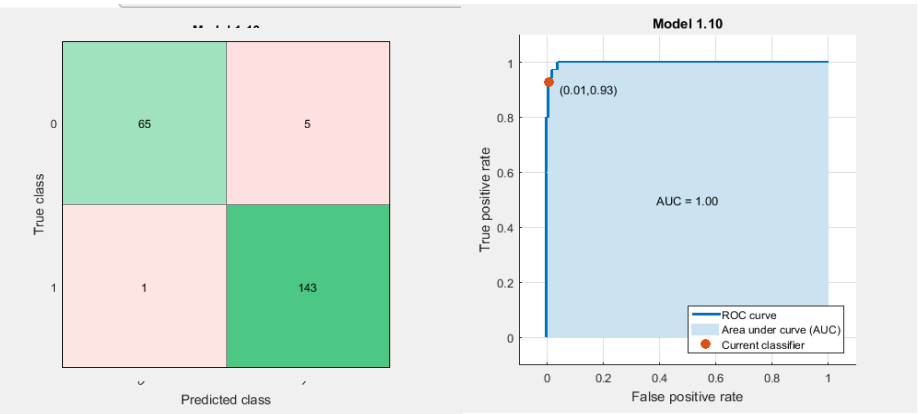

Figure [5.40]: Shows confusion matrix and ROC curve results from the combined features at 5 folds cross validation.

Then the classifier cross validation value change to 10 to get more accuracy, at 10 folds cross validation Figure: [5.41] the results TP, TN, FP and FN=64, 143, 6 and 1 respectively, accuracy was 96.7% and the ROC curve 1.00 by SVM classifier, where the SVM used before at (**Dharmanna** *et al*.2014), (Guerre et *al*.2014) and (Morris T. *et al.* 2015).

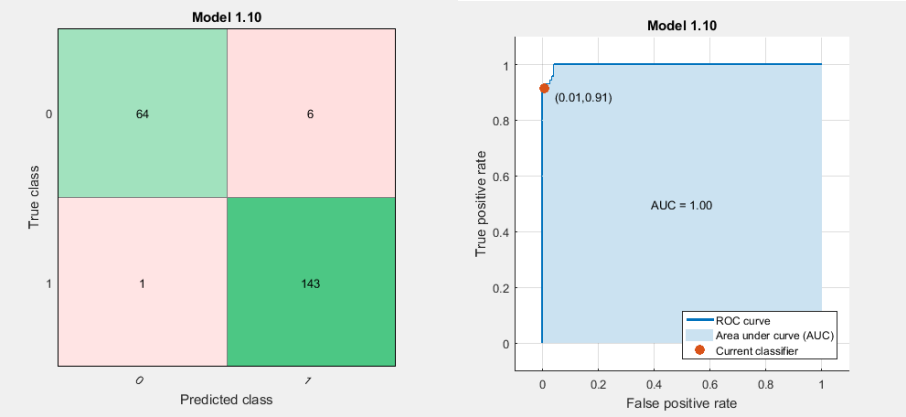

Figure [5.41]: Shows confusion matrix and ROC curve results from the combined features applied to RIM-ONE (version two) at 10 folds cross validation.

To evaluate the performance of the proposed algorithm ,the features was test in second database named Drishti-GS,contain 70 image glaucoma and 31 healthy image,the output Figure:[5.42] TP, TN, FP and FN=3, 116, 11 and 0 respectively, accuracy after features balanced at 10 fold cross validation was 91.5% and AUC 0.84 by ensembles Subspace KNN.

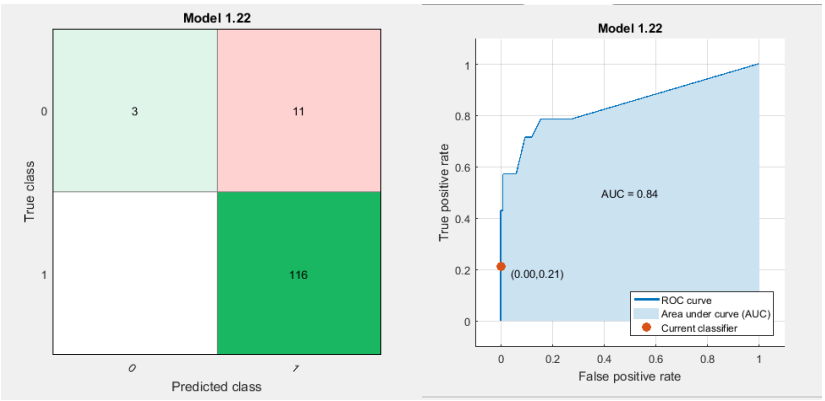

Figure [5.42]: Shows confusion matrix and ROC curve results from the combined features applied to Drishti-GS database at 10 folds cross validation.

The features was test in third database named RIM-ONE (version one) 200 image glaucoma and 255 healthy image,the output Figure:[5.44] TP, TN, FP and FN=36, 750, 45 and 0 respectively, accuracy after features balanced at 10 fold cross validation was 94.5% and AUC 0.96 by ensembles Subspace KNN.

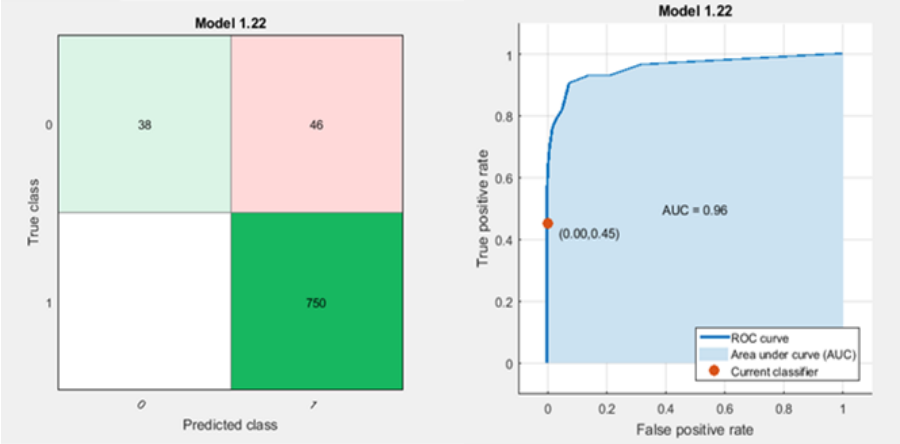

Figure [5.43]: Shows confusion matrix and ROC curve results from the combined features applied to RIM-ONE (version one) at 10 folds cross validation.

The new combination features compared with each feature types to prove the effectiveness of the new alogrithm compared with the existing methods, the results shown in Table (5.20) and Figure[5.43], the combined features shown the best performance in Figure[5.44].

Table (5.20): Shows the different types of features classification results at 10 folds.

Type of features	Accuracy%	AUC	Classifier
Shape features	91.3	0.92	Ensembles RUSBoosted tree
Color features	93.5	0.96	Ensembles subspace KNN
Texture features	89.5	0.93	Ensembles RUSBoosted tree
Combined features(proposed)	**96.7**	**0.99**	**SVM classifier**

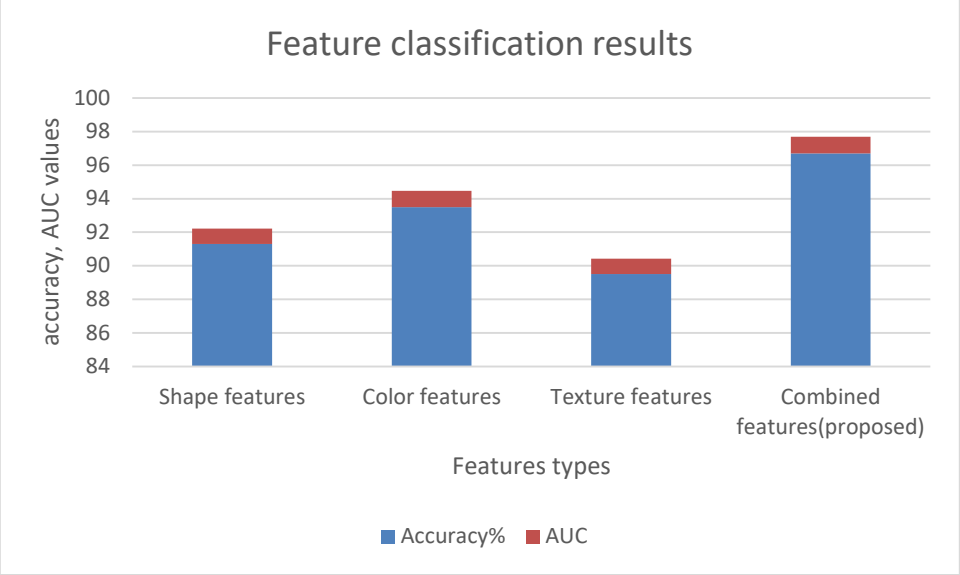

Figure[5.44]: Bar chart illustrates the different features applied for glaucoma detection.

Table(5.21): Show the proposed method classification results in the 4 database

Database	Accuracy%	AUC
RIM_ONE (version two)	96.7	1.00
Drishti_GS	91.5	0.84
RIM_ONE (version one)	94.5	0.96

The system validation is to evaluate each step separately as happened in filtering, segmentation and classification above, then evaluate the whole algorithm with existing ones as shown in table (5.22), based on the accuracy, sensitivity and specificity parameters.

Table (5.22): Shows the comparisons of the proposed system with previous studies in features types and system over all performances.

Authors	Year	Features	Accuracy %	Sensitivity%	Specificity%
Proposed system	**2018**	**Color, shape and texture features**	**97**	**98.4**	**96.6**
R. Geetha Ramani	2017	Statistical features	96.42	-	-
Mohd Nasiruddin	2017	CDR, blood vessel ratio, disc to center distance	-	100	80
Sharanagouda	2017	CDR+ISNT	97	-	-
Claro M.	2016	Disc segmentation, texture feature	93	-	-
Salem	2016	CDR, texture and intensity based features	-	100	87
Swapna’	2016	Fractal Dimension +LBP	88.7	87.2	90
Oh, Yang	2015	RNFL defects	94	86	75
Abir	2015	Grid Color Moment	87.5	-	-
Morris T.	2015	BRIEF	78	-	-
Karthikeyan Sakthivel	2015	LBP + Daugman's algorithm	-	95.4	95.4
Iyyanarappan	2014	DWT	95	-	-
Geetha Ramani	2014	color spaces, channel extraction, statistical, histogram, GLCM	86.67	-	-
Guerre, A.,	2014	CDR	89	93	85
Maya	2014	Local Binary Patterns	-	96.4	92.3
Ganesh Babu	2014	CDR+ISNT	96	96.5	93.3
Preethi	2014	CDR	96	-	-
Fauzia	2013	CDR,ISNT	94	-	-
Rama	2012	HOS,TT and DWT	91.67	90	93.33
Babu	2011	CDR	90	-	-
Muramatsu	2011	PPA	-	73	95

From the previous table, noticed that glaucoma detection can be performed through domain based features such as cup to disc ratio, PPA and ISNT ratio and/or other features such as texture and intensity based features

from the whole image. In the proposed system, domain based and statistical and texture features are extracted from the segmented optic disc, cup and RNFL and classified to detect Glaucoma.

Compared with (Anindita Septiarini *et al*.2018) which achieved accuracy 95.24% there is a good improved using proposed features.The result is reasonable because of the following considerations:

- The final accuracy is high after merge features more than each features type separately.
- The classification done by many classifiers and obtained similar high accuracy and high AUC.
- No significant over fitting has occurred because the final classification tested at 5 fold cross-validation and 10 fold cross-validation.

The results show the efficiency of the system based on the feature selected by the t-test and SFS method. Then, show the Glaucoma detection based on the final feature selected, Table: (5.23) Show the final proposed system evaluation parameters values. The performance of the research glaucoma detection method is expressed in terms of sensitivity, specificity, and accuracy. Those values are defined as follows:

Sensitivity (SE): Is the ratio of glaucoma images which were marked and classified as glaucoma, to all marked images.

SE=**TP**/ (**TP** + **FN**) **=TPR,** from this equation it calculated to be **0.98.**

Specificity (SP): Is the ratio of glaucoma which were marked and classified as healthy, to all marked images.

SP =**TN**/ (**FP** +**TN**) **=TNR,** from this equation it calculated to be **0.97.**

From the figure (5.20), we can notice that:

• **True positive (TP)** is the number images detected as glaucoma by an expert and the proposed method.

• **True negative (TN)** is the number of images detected as normal by an expert and the proposed method.

• **False positive (FP)** is the number of images detected as normal by an expert but detected as glaucoma by the proposed method.

• **False negative (FN)** is the number of images detected as glaucoma by an expert but detected as normal by the proposed method.

The values of sensitivity, specificity, and accuracy lie between 0 and 1. Therefore, if the result of the proposed method is accurate, it should be close to 1.

The performance of our proposed method was evaluated by comparing the results of glaucoma detection provided by an experts based on the classification results of our method using eight features .The marker on the plot shows the performance of the currently selected classifier. The marker shows the values of the false positive rate (FPR) and the true positive rate (TPR) for the currently selected classifier.

For more validation proposed algorithm compared with other glaucoma detection method used the same databases (RIM-ONE, DRISHTI-GS), the results shown in table (5.23).

Table (5.23): Shows the comparisons of the proposed system with previous studies used the same databases.

Authors	Used Database	Features	Accuracy %	Sensitivity %	Specificity %
Proposed system 2018	**DRISHTI-GS RIM-ONE**	**Color, Shape and Texture Features**	**97**	**98.4**	**96.6**
Cheriguene 2017	RIM-ONE	TWSVM and three types of features.	98.53	94.11	100
Artem 2017	DRISHTI-GS RIM-ONE	U-Net Convolutional Neural Network	92.08	80	62
Karkuzhali 2017	DRISHTI-GS	CDR,ISNT, DOO	100	100	100
Sharanagouda 2017	DRISHTI-GS	CDR+ISNT	96	-	-
Claro M. 2016	DRISHTI-GS RIM-ONE	Disc segmentation, texture feature	93	-	-
Swapna 2016	DRISHTI-GS	Texture Features Fractal Dimension +LBP.	88.70	87.2	90
Arunava 2016	DRISHTI-GS	Segmentation, Image-based Features	74.1	80	65
Ramaswamy 2016	RIM-ONE	A Depth Based Approach	-	83	83
Maila 2016	DRISHTI-GS RIM-ONE	GLCM,Entropy	93.03	-	-
Abir 2015	RIM-ONE	Grid Color Moment	87.5	-	-

From table (5.23) noticed that (Karkuzhali *et al*.2017) achieved 100% accuracy, sensitivity and specificity using small database 13 healthy images 13 glaucoma images. And (Cheriguene et al.2017) get accuracy 98.5% using twin support vector machine(TWSVM),where the TWSVM solves a pair of non-parallel hyper-planes whereas, the SVM solves a single complex one.(Swapna *et al*.2016) get accuracy 88.7% in detect glaucoma via texture

features, which is close to results obtained here using the texture features alone.

Table (5.24): Shows the final proposed system evaluation parameters values.

Sensitivity	Specificity	Overall accuracy
98.4%	96.6%	97%

For both glaucoma detection and classification, our method achieves excellent quality comparable to (Claro M. *et al.* 2016), which achieve accuracy 93% using texture and OD segmentation, and (Fauzia Khan *et al.* 2013) achieved overall accuracy 94% using CDR and ISNT rule features, and (Mohd Nasiruddin *et al*. 2017) achieved sensitivity and specificity of 100% and 80% respectively using ONH features, outperforming them in terms of the accuracy and type of features, even with the (salem *et al*.2016) who use a combination of structural (cup to disc ratio) and non-structural (texture and intensity) and achieved average sensitivity and specificity of proposed system are 100 and 87 % respectively, and (Sakthivel *et al.*2014) obtained accuracy 95% using GLCM features. Other algorithm based on for combined features is the study presented by (Sirel *et al.*2017), which conclude that the RNFL defects on OCT images alone may be misleading in glaucoma examination it needs another type of features to get accurate diagnose, where (Dharmanna *et al.*2014) find there is linear correlation coefficient between the RNFL defects and texture & fractal dimensions. Therefore, the glaucoma CAD system could be used in a low-priced medical screening, thus avoiding the inter-experts

variability issue by introducing the segmentation, features, and final diagnosing to the users as in figure [5.45].

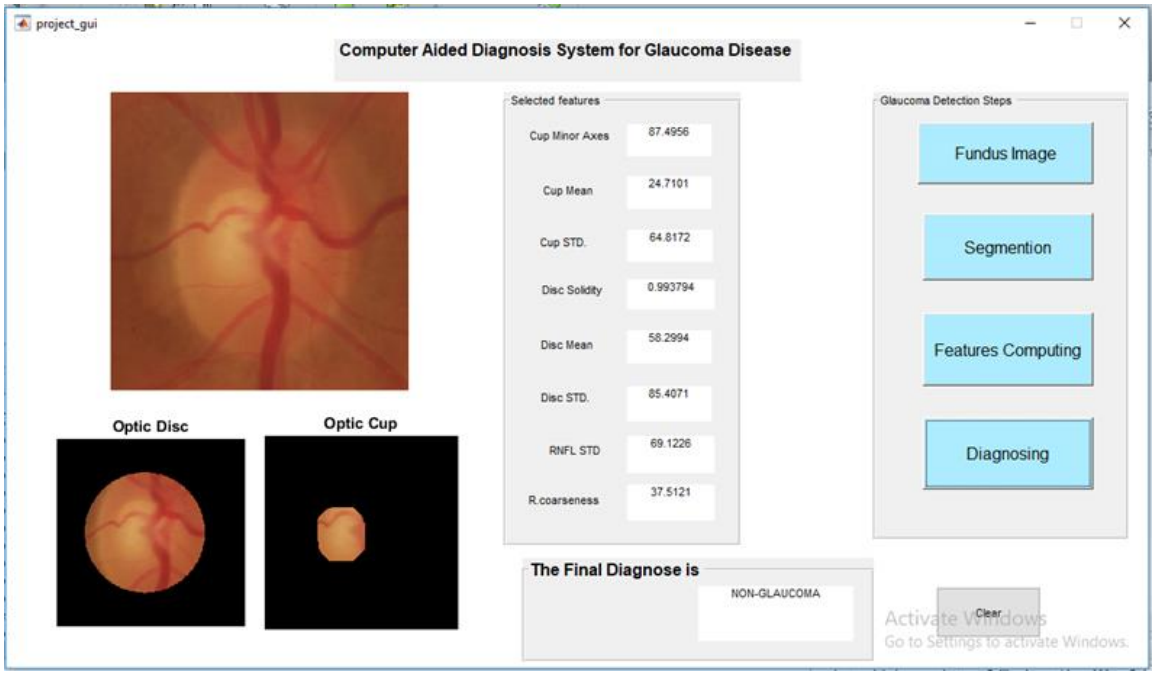

Figure [5.45]: Glaucoma CAD system.

CHAPTER SIX

CONCLUSION AND FUTURE SCOPE

6.1 Conclusions

In conclusion, where the glaucoma is a group of eye diseases and has no symptoms and if not detected at an early stage it may cause permanent blindness, it precedes some structural damage to the retina are the marked symptoms of glaucoma. Based on it is diagnosed by examination of size, structure, shape and color of optic disc and optic cup and retinal nerve fiber layer (RNFL), and due to the subjectivity of human due to experience, fatigue factor etc. there was a need for CAD system to manage large volumes of data, provide objective assessments for decision support and help in labor-intensive observer driven tasks used fundus image, because it among one of the biomedical imaging techniques to analyze the internal structure of retina. The proposed technique provides a novel algorithm to detect glaucoma from digital fundus image using MATLAB software and evaluated on a RIM_ONEv2 database containing digital fundus images from 158 patients (118 healthy and 40 glaucoma image) and Drishti_GS which contain 101 digital fundus images 70 glaucoma image and 31 healthy images, and RIM-ONEv1 (200 healthy image and 250 glaucoma image), where the proposed approach used to detect glaucoma via 3 steps: firstly, OD and OC segmentation. In OD and OC segmentation several steps were done like prepressing, thresholding, boundary smoothing, and disc reconstruction to be a full circle where OD segmentation achieved best dice coefficient(DSC) 90% and Structural Similarity (SSIM) 83% and OC segmentation results were dice

coefficient 73% and Structural Similarity (SSIM) 93%, and cup segmentation achieved SSIM 93%, secondly shape, color, and texture features were extracted from the segmented parts and then the most relevant features selected, thirdly and finally many types of classifier were applied to find the best classification accuracy via a set of color-based, shape-based, and texture features by extract 13 shape features from disc and cup, extract 25 texture features from RNFL (retinal nerve fiber layer) using gray level co-occurrence method and Tamar algorithm and 3 color feature for each of disc , cup, and RNFL. Next, best features were selected by T-test method and Sequential feature selection (SFS) to introduce eight features (cup minor axes, disc and cup mean and standard deviation and RNFL standard deviation and coarseness) with average accuracy 97% and maximize the area under the curve (AUC) 0.99 using SVM classifier. The key contribution in this work proposes new features are suitable for glaucoma detection.

In this study, an efficient approach for building a computerized system for glaucoma detection using digital fundus image is presented and discussed. The automated combined features system is a reliable and efficient method for glaucoma diagnosis. This research work focuses the digital fundus image analysis for glaucoma assessment to develop an automatic glaucoma detection system based on many features evaluation.

It is observed from the experimental results that the proposed system achieves better accuracy for glaucoma with combined feature than each type of features individually, and the proposed system achieves very promising results as accuracy for 97%, specificity 96.6% and sensitivity 98.4%. The objectives of this research are all met. The early detection system for

glaucoma diagnosis is effectively implemented, and features are computed to classify whether the corresponding digital fundus image is subjected with glaucoma or healthy. The experimental results pointed out that the use of shape, color and texture features of correctly segment OC, OD and RNFL region are affected in glaucoma diagnosis.

The proposed CAD system certainly will assist ophthalmologists for better diagnosis of the glaucoma disease and can make a valuable contribution to medical science by supporting medical image analysis for glaucoma detection.

6.2 Future Scope

As the field of interest and the results of this study turned out to be rich and broad, there are several ways to extend it. Some of the possible ways to investigate this work in the near future are discussed below:

1. Design a database connected with the software to save the patients fundus images and medical reports.
2. Design a complete, integrated, automated system to classify all different types of glaucoma namely: Primary Open-Angle Glaucoma, Normal Tension Glaucoma, Angle Closure Glaucoma, Acute Glaucoma, Exfoliation Syndrome and Trauma-Related Glaucoma.
3. Complete the system to do not just diagnose glaucoma but compute the progress of the disease by comparing the different image of the same patient to be used to follow up.
4. Design a holder to modify smartphones to be a simple and cheap fundus camera device with wide range availability.

References

Abdullah (2016). Localization and segmentation of optic disc in retinal images using circular Hough trans- form and grow-cut algorithm, PeerJ 4:e2003, DOI 10.7717.

Abir Ghosh, Amira S. Ashour, Nilanjan Dey, Anurag Sarkar, Dana Bălas-Timar, Valentina E. Balas (2015). Grid Color Moment Features in Glaucoma Classification, (IJACSA) International Journal of Advanced Computer Science and Applications Vol. 6, and (No. 9).

Abràmoff MD, Garvin MK, Sonka M (2010). Retinal imaging and image analysis, Copyright @ IEEE Rev Biomed Eng, Vol. 3, p.169–208.

Achanta R, Shaji A, Smith K, Lucchi A & Susstrunk S (2012). 'Slic super pixels compared to state-of-the-art super pixel methods', IEEE Transactions on Pattern Analysis and Machine Intelligence, Vol. 34, No. 11, P.2274–2281.

Acharya. U. R., S. Dua, X. Du, V. Sree S, and C. K. Chua (2011). Automated diagnosis of glaucoma using texture and higher order spectra features, IEEE Transactions on Information Technology in Biomedicine, vol. 15,(no. 3), p. 449–455.

Adrian B, Risteárd Ó, Peter M, Ronan Mc (2012). Discrepancy and Error in Radiology Concepts and Causes and Consequences, Ulster Med J, Vol.81 (1), p. 3-9.

Ahmed A (2017). Optic disc segmentation for glaucoma screening system using fundus images, Clinical Ophthalmology, p.2017–2029.

Ahmed Almazroa,1 Ritambhar Burman,2 Kaamran Raahemifar,3 (2015). Optic Disc and Optic Cup Segmentation Methodologies for

Glaucoma Image Detection: A Survey, Journal of Ophthalmology , Article ID 180972, 28 pageshttp://dx.doi.org/10.1155/2015/180972.

Ali Allam (2017). Automatic Detection of Landmarks and Abnormalities in Eye Fundus Images (February), publication at: https://www.researchgate.net/publication/308611012, DOI: 10.13140/RG.2.2.23488.12800.

Alghamdi M, Al-Mallah M, Keteyian S, Brawner C, Ehrman J, Sakr S (2017) Predicting diabetes mellitus using SMOTE and ensemble machine learning approach: The Henry Ford ExercIse Testing (FIT) project. Vol. 12(No.7):e0179805. https://doi.org/10.1371/journal. pone.0179805.

Almazroa, Ahmed & Sun, Weiwei & Alodhayb, Sami & Raahemifar, Kaamran & Lakshminarayanan, Vasudevan. (2017). Optic disc segmentation: level set methods and blood vessels inpainting. 1013806. 10.1117/12.2254174.

Allingham.R.R, K.F. Damji (2005). Shields Textbook of Glaucoma, 5th ed.: Lippincott Williams & Wilkins.

Alward.W. L. (1998). Medical management of glaucoma, New England Journal of Medicine, Vol. 339, (No. 18), p. 1298–1307.

Angel Suero, Diego Marin, Manuel E. Gegundez-Arias, and Jose M. Bravo. (2013). Locating the Optic Disc in Retinal Images Using Morphological Techniques, IWBBIO 2013 Proceedings, Granada, 18-20 March, p.593-600.

Anindita Septiarini, Agus Harjoko (2015). Automatic Glaucoma Detection Based On The Type Of Features Used: A Review, Journal of

Theoretical and Applied Information Technology (28th February), Vol.72 No.3, © 2005 - 2015 JATIT & LLS, ISSN: 1992-8645.

Anindita Septiarini, Dr, Dyna M. Khairina, MKom, Awang H. Kridalaksana, MKom,Hamdani Hamdani, MCs (2018). Automatic Glaucoma Detection Method Applying a Statistical Approach to Fundus Images, Healthcare Informatics Reasearch, (January, 24), p. 53-60 ,pISSN 2093-3681.

Annesha Malakar1, Joydeep Mukherjee2 (2013). Image Clustering using Color Moments, Histogram, Edge and K-means Clustering. International Journal of Science and Research (IJSR), Volume 2 Issue 1, January. India Online ISSN: 2319-7064.

Anum A. Salam, Tehmina Khalil, and Imran Basit (2016). Automated detection of glaucoma using structural and nonstructural features, Springer plus, Vol. 5(1): 1519. Published online 2016 Sep 9. doi: 10.1186/s40064-016-3175-4, PMCID: PMC5017972, PMID: 27652092.

Artem Sevastopolsky1 (2017). Optic Disc and Cup Segmentation Methods for Glaucoma Detection with Modification of U-Net Convolutional Neural Network, (4 Apr), Lomonosov Moscow State University, arXiv: 1704.00979v1.

Arwa Ahmed Gasm Elseid, Mohamed Eltahir Elmanna, Alnazier Osman Hamza (2018). Evaluation of Spatial Filtering Techniques in Retinal Fundus Images, American Journal of Artificial Intelligence. Vol. 2, No. 2, 2018, pp. 16-21. doi: 10.11648/j.ajai.20180202.11.

Arwa Ahmed Gasm Elseid and Mohamed Eltahir Elmanna (2018). Optic cup segmentation using manual thresholding level technique,

International Journal of Current Research in Life Sciences, 7, (10), 2769-2773.

Arwa Ahmed, and Alnazier Osman (2018). Optic Disc Segmentation Using Manual Thresholding Technique, Journal of Clinical Engineering, Vol. 44, N0.1, issue: January/March 2019, Copyright © 2018 Wolters Kluwer Health.

Arwa Ahmed Gasm Elseid, Alnazier Osman Hamza, and Ahmed Fragoon (2018). Developing A Real Time Algorithm For Diagnosing Glaucoma, ICTACT Journal On Image And Video Processing, VOL.09, ISSUE: 02.

Arwa A. Gasm Elseid and Alnazier O. Hamza (2018). Glaucoma Detection Based On Shape Features and SMOTE Algorithm, CiiT International Journal of Digital Image Processing, Vol. 10, No. 10, ISSUE: October – November.

Arunava Chakravarty and Jayanthi Sivaswamy (2016). Glaucoma Classification with a Fusion of Segmentation and Image-based Features, 978-1-4799-2349-6/16/$31.00 ©2016 IEEE.

Aslam, Javed A, Popa, Raluca A and Rivest, Ronald L (2007). On Estimating the Size and Confidence of a Statistical Audit, Proceedings of the Electronic Voting Technology Workshop (EVT07), Boston, MA, (August 6, 2007).n (1 − e − n ′ / n) {\displaystyle n(1-e^{-n'/n})}

Bermingham, Mairead L, Pong-Wong, Ricardo, Spiliopoulou, Athina, Hayward, Caroline; Rudan, Igor, (2015). Application of high-dimensional feature selection: evaluation for genomic prediction in man" , Sci. Rep. 5: 10312. Doi: 10.1038/srep10312.

Bernardes R, Serranho P, Lobo C. (2011). Digital ocular fundus imaging: a revie, Ophthalmological, Vol. 226, No. 4, p.161–181.

Bock, Rüdiger; Meier, Jörg; Nyúl, László G.; Hornegger, Joachim; Michelson (2010). Georg (Glaucoma Risk Index: Automated glaucoma detection from color fundus images), PMID.

Bowd.C, L. M. Zangwill, C. C. Berry, E. Z. Blumenthal, C. Vasile,C. Sanchez-Galeana, C. F. Bosworth (2001). Detecting early glaucoma by assessment of retinal nerve fiber layerthickness and visual function, Investigative Ophthalmology & Visual Science, Vol. 42, No. 9, p. 1993–2003.

Bourne RRA, Taylor HR, Flaxman SR, Keeffe J, Leasher J, Naidoo K, et al. (2016) Number of People Blind or Visually Impaired by Glaucoma Worldwide and in World Regions 1990 ± 2010: A Meta-Analysis. PLoS ONE 11(10): e0162229. doi:10.1371/journal.pone.0162229.

Breiman, Leo (1996).Bagging predictors, Machine Learning, CiteSeerX 10 .1. 1.32 .9399 Vol.24 (2): p. 123–140,doi:10.1007/BF00058655.

Cello.K. E, J. M. Nelson-Quigg, and C. A. Johnson (2000). Frequency doubling technology perimetry for detection of glaucomatous visual field loss, American Journal of Ophthalmology, Vol. 129, (No. 3), p. 314–322.

Chan .T. F and L. A. Vese, (2001). Active Contours without Edges, IEEE Transactions on Image Processing, vol. 10, (No. 2), pp. 266-277.

Cheriguene, N. Azizi, H. Djellali, O. Bounakhla, M, Aldwairi, A, Ziani.(2017), New Computer Aided Diagnosis System for

Glaucoma disease based on Twin Support Vector Machine, First international conference on Embedded & Distributed Systems, EDiS.

Chrastek.R, M. Wolf, K. Donath, G. Michelson, and H. Niemann(2002). Optic disc segmentation in retinal images, BVM, p. 263–266.

Chris Seiffert, Taghi M. Khoshgoftaar Jason Van Hulse, and Amri Napolitano (2010).Rusboost:a hybrid approach to alleviating class imbalance, ieee transactions on systems, man, and cybernetics—part a: systems and humans, VOL. 40, (NO. 1, JANUARY 2010).

Claro M., Leonardo Santos, Wallinson Silva ,Fl_avio Ara_ujo, Nayara Moura.(AUGUST 2016), Automatic Glaucoma Detection Based on Optic Disc Segmentation and Texture Feature Extraction, CLEI ELECTRONIC JOURNAL, VOL. 19, NUM. 2, P. 4.

Coleman.A. L and S. Miglior (2008). Risk factors for glaucoma onset and progression, Ophthalmology, Vol. 53, No. 6, Supplement, p. S3–S10.

Damms, Dannheim, (1993). Sensitivity and specificity of optic disc parameters in chronic glaucoma, PMID: 8505205, 1993 Jun, Vol.34 (7), p.2246-2250.

Deepikaa, L.Mary Gladenceb, S.Kalpanac (2016). Detection of glaucoma based on optic disc and optic cup segmentation using slice super pixels, International Journal of Pharmacy & Technology, Vol. 8 ,Issue 4, p. 22781-22792.

Denise Grady (1993). The Vision Thing: Mainly in the Brain, Discover, (June 01, 1993), http:// discovermagazine.com /1993/jun/ thevisionthingma227.

Delia Cabrera Fernández, Harry M. Salinas, Carmen A. Puliafito (2006). Automated detection of retinal layer structures on optical coherence tomography images, DOI: 10.1364/OPEX.13.010200 · Source: PubMed,@ 2005 Optical Society of America.

Dhawan A. and S. Dai (2008). Clustering and Pattern Classification, in Principles and Advanced Methods in Medical Imaging and Image Analysis. Singapore, World Scientific Publishing Co. Pte. Ltd, p. 229-265.

Dharmanna Lamani, T. C. Manjunath, Mahesh M, Y. S. Nijagunarya (2014). Early detection of glaucoma through retinal nerve fiber layer analysis using fractal dimension and texture feature, International Journal of Research in Engineering and Technology, eISSN: 2319-1163 | pISSN: 2321-7308, Vol.03 Issue: 10 .

Dougherty. G (2009). Digital Image Processing for Medical Applications, New York: Cambridge University Press, ISBN-13 978-0-511-53343-3.

Downs.J. C, M. D. Roberts, and I. A. Sigal (2011). Glaucomatous cupping of the lamina crib Rosa: a review of the evidence for active progressive modeling as a mechanism, Experimental Eye Research, Vol. 93, (No. 2), p. 133–140.

Dnyaneshwari D.Patil, RameshManza, Gangadevi C. Bedke (2014). Diagnose Glaucoma by Proposed Image Processing Methods,

International Journal of Computer Applications (0975 – 8887) Vol. 106 – No.8.

Drance.S, D. R. Anderson, and M. Schulzer (2001). Risk factors for progression of visual field abnormalities in normal-tension glaucoma, American Journal of Ophthalmology, Vol. 131, (No. 6), p. 699–708,

Eleesa Jacob1, R.Venkatesh2 (2014). A Method of Segmentation for Glaucoma Screening Using Superpixel Classification, International Journal of Innovative Research in Computer and Communication Engineering (An ISO 3297: 2007 Certified Organization) Vol.2, Special Issue 1, p.2536-2544.

Engelhorn.T, G. Michelson, S. Waerntges, T. Struffert, S. Haider, and A. Doerfler (2011). Diffusion tensor imaging detects rarefaction of optic radiation in glaucoma patients. Academic Radiology, Vol. 18, (No. 6), p. 764–769.

Fauzia Khan, Shoaib A. Khan, Ubaid Ullah Yasin, Ihtisham ul Haq, Usman Qamar (2013). Detection of Glaucoma Using Retinal Fundus Images, the 2013 Biomedical Engineering International Conference (BMEiCON-2013), DOI: 10.1109/BMEiCon.2013.6687674.

Fechtner. R and R. Weinreb (1994). Mechanisms of optic nerve damage inprimary open angle glaucoma, Surv Ophthalmol, Vol. 39, (No. 1), p. 23–42.

Ferreras. A, L. Pablo, J. Larrosa, V. Polo, A. B. Pajarin, and F. M.Honrubia (2008). Discriminating between normal and glaucoma-damaged

eyes with the Heidelberg retina Tomograph 3, Ophthalmology, Vol. 115, (No. 5), p. 775–781.e2.

Ferri, F. J., Pudil P., Hatef, M., Kittler, J. (1994). Comparative study of techniques for large-scale feature selection, Pattern Recognition in Practice IV, p. 403-413.

Fernandez-Granero, A. Sarmiento, D. Sanchez-Morillo, S. Jiménez,P. Alemany, and I. Fondón2(2017). Automatic CDR Estimation for Early Glaucoma Diagnosis, Journal of Healthcare Engineering, Vol. 2017, Article ID 5953621, 14 pages, https://doi.org/ 10.1155/2017/ 5953621.

F. Fumero1, J. Sigut2, S. Alayón3, (2015). Interactive Tool and Database for Optic Disc and Cup Segmentation of Stereo and Monocular Retinal Fundus Images, WSCG 2015 Conference on Computer Graphics, Visualization and Computer Vision, ISBN 978-80-86943-66-4.

Foster. P.J, R. Buhrmann, H. A. Quigley, and G. J. Johnson (2002). The definition and classification of glaucoma in prevalence surveys, British Journal of Ophthalmology, Vol. 86, (No. 2), p. 238–242.

Fumero1.F, S. Alayon1, J.L. Sanchez1, RIM-ONE (2011). An Open Retinal Image Database for Optic Nerve Evaluation, Proceedings of the IEEE Symposium on Computer-Based Medical Systems· (July 2011), DOI:10.1109/CBMS.2011.5999143·

Ganesh Babu T.R & S.Shenbagadevi (2011). Automatic detection glaucoma using fundus image, European journal of scientist research, Vol.59, (No.1), p.22-32, 2011.

Ganesh Babu.T.R, R.Sathishkumar and Rengara Jvenkatesh. (2014), Segmentation of Optic Nerve Head for Glaucoma Detection using Fundus images, Biomed. & Pharmacol. J., Vol. 7(2), p. 697-705.

Garaci.F, F. Bolacchi, A. Cerulli, M. Melis, A. Spano, C. Cedrone,R. Floris, G. Simonetti, and C. Nucci (2009). Optic nerve and optic radiation neuro degeneration in patients with glaucoma: in vivo analysis with 3-Tdiffusion-tensor MR imaging, Radiology, Vol. 252, (No. 2), p. 496–501.

Gareth James, Daniela Witten, Trevor Hastie; Robert Tibshirani (2013). An Introduction to Statistical Learning, Springer, p. 204.

Gaurav Kumar, Pradeep Kumar Bhatia (2014). A Detailed Review of Feature Extraction in Image Processing Systems, Research Gate, Conference Paper, (February 2014), DOI: 10.1109/ACCT.2014.74

Geetha Ramani, Sugirtharani S., Lakshmi B (2017). Automatic Detection of Glaucoma in Retinal Fundus Images through Image Processing and Data Mining Techniques, International Journal of Computer Applications (0975 – 8887), Vol. 166, (No.8, May 2017).

Geetha Ramani, R, Dhanapackiam, C and Lakshmi, B. (2014). Automatic Detection of Glaucoma in Fundus Images through Image Features, International conference on Knowledge Modelling and Knowledge Management, p. 135-144.

Gonzalez.R. C. and R. E.Woods (2008). Digital Image Processing, Third Edition.

Gopal Datt Joshi, Jayanthi Sivaswamy, Kundan Karan, S. R. Krishnadas (2010). Optic Disk and Cup Boundary Detection Using Regional

Information" Proceedings of the 2010 IEEE international conference on biomedical imaging: from Nano to Macro.

Guerre, A., Martinez-del-Rincon, J., Miller, P., & Azuara-Blanco, A. (2014). Automatic Analysis of Digital Retinal, Images for Glaucoma Detection. Paper presented at Irish Machine Vision and Image Processing Conference, Derry, United Kingdom.

Gupta. N and Y. Yucel (2007).What changes can we expect in the brain of glaucoma patients? Survey of Ophthalmology, Vol. 52, (No. 6), Supplement1, p. S122–S126.

Gupta.N, L. Ang, L. de Tilly, L. Bidaisee, and Y. Yucel (2006). Human glaucoma and neural degeneration in intracranial optic nerve, lateral geniculate nucleus, and visual cortex, British Journal of Ophthalmology, Vol. 90, (No. 6), p. 674–678, 2006.

Guyon, Isabelle, Elisseeff, André (2003). An Introduction to Variable and Feature Selection, JMLR. 3.

Harizman.N and C. Oliveira et al. (2006). The ISNT Rule and Differentiation of Normal, From Glaucomatous Eyes. Arch Ophthalmol, p. 1579-1583, 124.

Huazhu Fu, Jun Cheng, Yanwu Xu, Damon Wing Kee Wong, Jiang Liu, and Xiaochun Cao (2018). Joint Optic Disc and Cup Segmentation Based on Multi-label Deep Network and Polar Transformation, arXiv: 1801.00926v3 [cs.CV], p.1-9.

Huajun Ying, Ming Zhang and Jyh-Charn Liu (2007). Fractal-Based Automatic Localization and Segmentation of Optic Disc in Retinal Images, 28th Annual International Conference of the IEEE, Engineering in Medicine and Biology Society (EMBS).

Huiqi Li, Opas Chutatape (2003). Boundary detection of optic disc by a modified ASM method, The Journal of the Pattern Recognition Society, Vol. 36, p. 2093-2104.

Hussain, A.R. (2008). Optic nerve head segmentation using genetic active Contours, International, Conference on Computer and Communication Engineering, ICCCE 2008, (13-15 May 2008), p.783 – 787.

Imran Qureshi .(2015), Survey: Glaucoma Detection in Retinal Images Using Image Processing Techniques, Int. J. Advanced Networking and Applications, Vol. 7, Issue: 02, P. 2705-2718, ISSN: 0975-0290

Ingle.R and P. Mishra (2013). Cup segmentation by gradient method for the assessment of glaucoma from retinal image, International Journal of Engineering Trends and Technology, vol. 4, (no. 6), p. 2540–2543.

Iyyanarappan, G.Tamilpavai. (2014), Glaucomatous Image Classification Using Wavelet Based Energy Features and PNN, IJTEEE, VOL 2, p.85-90, ISSUE 4, ISSN 2347-4289.

Jan. J, J. Odstrcilik, J. Gazarek, and R. Kolar (2012). Retinal image analysis aimed at blood vessel tree segmentation and early detection of neural-layer deterioration, Computerized Medical Imaging and Graphics, Vol. 36, No. 6, P. 431–441.

Jan Odstrcilika,, Radim Kolara, Ralf-Peter Tornowc, Jiri Janb, Attila Budaid,Markus Mayerd, Martina Vodakovab, Robert Laemmerc, Martin Lamosb, Zdenek Kunab,Jiri Gazarekb, Tomas Kubenae, Pavel Cernoseke, Marina Ronzhinaa(2014). Thickness related textural properties of retinal nerve fiber layer incolor fundus images, Computerized Medical Imaging and Graphics, Vol. 38, p. 508–516.

Jaskowiak, P. A, Campello, R. J. G. B (2011). Comparing Correlation Coefficients as Dissimilarity Measures for Cancer Classification in Gene Expression Data, research gate conference publication at: https://www.researchgate.net/publication/260333185.

Jayanthi Sivaswamyy S.R. Krishnadas, Gopal Dutt Joshiy, Madhulika Jainy, Ujjwaly Syed Tabish A (2011), DRISHTI-GS: retinal image dataset for optic nerve head (ONH), Arvind Eye Hospital, Madurai, India.

Jen Hong Tan, U. Rajendra Acharya, Sulatha V. Bhandary, Kuang Chua Chua, Sobha Sivaprasad (2017).Segmentation of optic disc, fovea and retinal vasculature using a single convolutional neural network, arXiv.org > cs > arXiv:1702.00509, p.1-24.

Jonas.J.B, M.C. Fernandez and G.O. Naumann (1992). Glaucomatous parapapillary atrophy. Occurrence and correlations, Arch Ophthalmol, vol. 110, (no. 2), p. 214–222, (Feb).

Jonas.J.B, W.M. Budde and S. Panda-Jonas (1999), Ophthalmoscopic evaluation of the optic nerve head, Surv Ophthalmol, vol. 43, (no. 4), p. 293-320, (Jan-Feb 1999).

Jonas.J.B, M.C. Fernández and J. Stürmer. (1993). Pattern of glaucomatous neuroretinal rim loss, Ophthalmology, vol. 100, no. 1, p. 63-8, (Jan 1993).

Joshi G D, Sivaswamy J & Krishnaas S.R. (2011). Optic disk and cup segmentation from monocular color retinal images for glaucoma assessment, IEEE Transactions on Medical Imaging, Vol. 30, (No. 6), p.1192–1205.

Joshi, G.D., Sivaswamy, J., Karan, K., Prashanth, R., Krishnadas, S.R.(2010), Vessel Bend-Based Cup Segmentation in Retinal

Images, 20th International Conference on Pattern Recognition (ICPR), 2010, CVIT, IIIT Hyderabad, Hyderabad, India, 23-26 (Aug. 2010), p. 2536 – 2539.

Jun Cheng ,Jiang Liu ,Yanwu Xu ,Fengshou Yin ,Damon Wing Kee Wong (2013). Superpixel Classification Based Optic Disc and Optic Cup Segmentation for Glaucoma Screening, IEEE Transactions on Medical Imaging , Volume: 32, Issue: 6.

Kajić V, Povazay B, Hermann B, Hofer B, Marshall D, Rosin PL, Drexler W,R (2010).obust segmentation of intra retinal layers in the normal human fovea using a novel statistical model based on texture and shape analysis, Opt Express ,Vol. 18,(No.14), p.14730–14744.

Kass. M, A. Witkin and D. Terzopoulos (1988). Snakes: Active Contour Models, International Journal of Computer Vision, p. 321-331.

Kartik Thakkar, Dr. Kinjan Chauhan, Dr. Anand Sudhalkar, Dr. Ravi Gulati. (2017), Detection of Glaucoma from Retinal Fundus Images by analyzing ISNT Measurement and features of Optic Cup and Blood Vessels, International Journal of Engineering Technology Science and Research (IJETSR), ISSN 2394 – 3386, Vol. 4, Issue 7,p.487-493.

Karkuzhali S*, Manimegalai D.(2017), Computational intelligence-based decision support system for glaucoma detection, Biomedical Research 2017,VOL. 28 (11),P. 4737-4748.

Kavitha, IIM. Malathi (2014). Optic Disc and Optic Cup Segmentation for Glaucoma Classification, International Journal of Advanced Research in Computer Science & Technology (IJARCST 2014) Vol. 2 Issue Special ,p.87-90.

Kelly H. Zou, PhD, Simon K. Warfield (2006). Statistical Validation of Image Segmentation Quality Based on a Spatial Overlap Index, NIH Public Access Author Manuscript,Acad Radiol, available in PMC (2006 March 28).

Kumar 1, Ms. Sukanya Banerjee (2014). International Journal of Advanced Research in Computer Engineering & Technology (IJARCET) Volume 3 Issue 12, (December 2014).

Koprowski (2014). Automatic method of analysis of OCT images in assessing the severity degree of glaucoma and the visual field loss, BioMedical Engineering on Line 2014.

Koprowski R, Teper S, Wrobel Z, Wylegala E. (2013). Automatic analysis of selected choroidal diseases in OCT images of the eye fundus. Biomed Eng. Online, 12:117.

Koprowski R, Wróbel Z. (2011). Image Processing in Optical Coherence Tomography: Using Matlab. Katowice, Poland: University of Silesia, Copyright http://www.ncbi.nlm.nih.gov/books/NBK97169.

Kotecha. (2002). Clinical examination of the glaucomatous patient [Online], www.optometry.co.uk.

Kou, W. Chen, C. Wen and Z. Li. (2015), Gradient Domain Guided Image Filtering, in IEEE Transactions on Image Processing, vol. 24, no. 11, pp. 4528 - 4539, ,doi: 10.1109/TIP.2015.2468183.

Kroese.M and H. Burton (2003). Primary open angle glaucoma: The need for a consensus case definition, Journal of Epidemiology and Community Health, Vol. 57, (No. 9), p. 752–754.

Kuehn.M, J. Fingert, and Y. Kwon (2005). Retinal ganglion cell death in glaucoma: mechanisms and neuroprotective strategies, Ophthalmol Clin North Am, Vol. 18, pp. 383–395.

Kumar Arun M.N, H.S. Sheshadri (2012). Building Accurate Classifier for the Classification of Micro calcification, (IJCSIT) International Journal of Computer Science and Information Technologies, Vol. 3 6, p.5346-5350.

Kwon.Y. H., J. H. Fingert, M. H. Kuehn, and W. L. Alward (2009). Primary open-angle glaucoma, New England Journal of Medicine, Vol. 360, (No. 11), p. 1113–1124.

Lalonde.M, M. Beaulieu, and L. Gagnon (2001). Fast and robust optic disc detection using pyramidal decomposition and hausdorff-based template matching, IEEE Trans Med Imaging,Vol. 20(11), p. 1193–1200.

Lim. R, I. Goldberg, mph, franzco, franzco, fracs , paul n. schacknow, john r. samples (2010). A Practical Evidence-Based Approach to Patient Care, the Glaucoma Book: (Chapter 1, p. 3).

Lim. T.C, S. Chattopadhyay, U.R. Acharya, (2012). A survey and comparative study on the instruments for glaucoma detection, j. Biomedical Engineering and Technology, Vol. 34, No. 2, p. 129–139.

luis j. haddock, md • allie nadelson, md.(2016), Teleophthalmology of Retinal Diseases, Retinal Physicians, Vol.13, Issue: April 2016, p.34, 36-38.

Mahalakshmi, S.Karthikeyan (2014). Clustering Based Optic Disc and Optic Cup Segmentation for Glaucoma Detection, International Journal of

Innovative Research in Computer and Communication Engineering, An ISO 3297: 2007 Certified Organization, Vol. 2, Issue 4.

Maila Claro, Leonardo Santos, Wallinson SilvaFliavio Araiujo, Nayara Moura.(2016), Automatic Glaucoma Detection Based on Optic Disc

Segmentation and Texture Feature Extraction, Clei Electronic Journal, Vol. 19, No. 2, P. 4.

Manohar. (2011), coded SMOTE algorithm, matlab file exchange, https://www.mathworks.com/matlabcentral/fileexchange/38830-smote-synthetic-minority-over-sampling-technique

Mauricio Maia, Juliana Prazeres, Bruno de Paula Freitas, Rubens Belfort (2017). The Zika Virus: Review of Ocular Findings, from book: Emerging infectious uveitis, pp.199-203.

Maya Alsheh Ali, Thomas Hurtut, Timothée Faucon, Farida Cheriet (2014). Glaucoma Detection based on Local Binary Patterns in Fundus Photographs, SPIE Medical Imaging, Feb 2014, United States, p. 903531-903531-7, 2014, <10.1117/12.2043098>. <hal-00993552.

Maureen van Eijnatten1 , Juha Koivisto1,2 , Kalle Karhu2·Tymour Forouzanfar1 , Jan Wolff1 (2017). The impact of manual threshold selection in medical additive Manufacturing, Int J CARS ,12:607–615, DOI 10.1007/s11548-016-1490-4.

Matlab background, http://cimss.ssec. wisc.edu/wxwise/class/ aos340/spr00/ whatismatlab.htm, visited at (JAN,2018).

Medha V., Dr. Pradeep M. (2014). Performance Evaluation of Optic Disc Segmentation Algorithmsin Retinal Fundus Images: an Empirical Investigation, International Journal of Advanced Science and Technology Vol. 69, pp.19-32.

Muramatsu.C, Y. Hatanaka, A. Sawada, T. Yamamoto and H. Fujita (2011). Computerized Detection of Peripapillary Chorioretinal Atrophy by Texture Analysis, in 33rd Annual International Conference of the IEEE EMBS, Boston, p.5974-5950.

Mohd Nasiruddin1, Faizan Ahmed2, Ashar Quazi3, Mubashara Mehrosh4, Kahekashan Anjum. (March 2017), Computer Aided Design of Glaucoma Detection, International Journal of Engineering Science and Computing, Vol. 7, Issue No.3.

Morris T., Suraya Mohammed (2015), characterizing glaucoma using texture, the University Of Manchester.

Monica Gandhi, suneeta dubey.(2013), Evaluation of the Optic Nerve Head in Glaucoma, Journal of Current Glaucoma Practice, September-December 2013,Vol.7, Issue No.3,p.106-114.

Murugan C, Golodza BZ, Pillay K, et al (2015). Retinal nerve fiber layer thickness of black and Indian myopic students at the University of KwaZulu- Natal. Vision Eye Health. 2015, Vol. 74(1), Art. #24, 6 pages. http://dx.doi.org/10.4102/ aveh.v74i1.24

Nave.R, S. Foresti, A. Pratesi, A. Ginestroni, M. Inzitari, E. Salvadori,M. Giannelli, S. Diciotti, D. Inzitari, and M. Mascalchi (2007). Whole-brain histogram and voxel-based analyses of diffusion tensor imaging in patients with leukoaraiosis: correlation with motor and cognitive impairment, AJNR Am J Neuroradiol, Vol. 28, (No. 7), p. 1313–1319.

Nouri, Mahdavi. K, D. Hoffman, D. P. Tannenbaum, S. K. Law, and J. Caprioli (2004). Identifying early glaucoma with optical coherence

tomography, American Journal of Ophthalmology, Vol. 137, (No. 2), p. 228–235, 2004.

Noor Elaiza Abdul Khalida, Noorhayati Mohamed Noora, Norharyati Md. Ariffa. (2014), Fuzzy c-Means (FCM) for Optic Cup and Disc Segmentation with Morphological Operation, Procedia Computer Science, Vol. 42, P. 255 – 262.

Odstrcilik.J,R.Kolar,V.Harabis, J.Gazarek, and J. Jan (2010).Retinal nerve fiber layer analysis via markov random fields texture modelling, in Proceedings of the 18th European Signal Processing Conference, p. 1650–1654.

Oh JE, Yang HK, Kim KG, Hwang J-M (2015). Automatic computer-aided diagnosis of retinal nerve fiber layer defects using fundus photographs in optic neuropathy. Invest Ophthalmol Vis Sci, p.2872–2879, DOI:10.1167/iovs.14-15096.

Otsu, N. (1979). A Threshold Selection Method from Gray-Level Histograms , IEEE Transactions on Systems, Man, and Cybernetics, Vol. 9, (No. 1), p. 62-66.

Pallawala.P, W. Hsu, M. Lee, and K. Eong (2004). Automated optic disc localization and contour detection using ellipse fitting and wavelet transform, Proc. ECCV, p. 139–151.

Peter Ndajah, Hisakazu Kikuchi, Masahiro Yukawa, Hidenori Watanabe, Shogo Muramatsu (2011). An Investigation on The Quality of Denoised Images, International Journal Of Circuits, Issue 4, Vol. 5.

Pachiyappan, Arulmozhivarman, Undurti N Das, Tatavarti VSP Murthy and Rao Tatavarti (2012). Automated diagnosis of diabetic retinopathy

and glaucoma using fundus and OCT images, Lipids in Health and Disease, 11:73.

Prageeth.P. G, J. David, and A. Sukesh Kumar (2011). Early detection of retinal nerve fiber layer defects using fundus image processing, in Proceedings of the IEEE Recent Advances in Intelligent Computational Systems (RAICS ’11), (September 2011), p. 930–936.

Prasad N. Maldhure, Prof. V. V. Dixit. (2015). Glaucoma Detection Using Optic Cup and Optic Disc Segmentation, International Journal of Engineering Trends and Technology (IJETT), Vol. 20, No. 2.

Prasantha (2010). Medical Image Segmentation, (IJCSE) International Journal on Computer Science and Engineering Vol. 02, (No. 04), p.1209-1218.

Preethi Rajaiah, R. John Britto.(2014), Optic Disc Boundary Detection and Cup Segmentation for Prediction of Glaucoma, International Journal of Science Engineering and Technology Research (IJSETR), Vol. 3, Issue 10,(October 2014),p. 2665-2671.

Priyadharshini, M., Glory, L. and Anitha, J. (2014). A Region Growing method of Optic Disc segmentation in retinal images, International Conference on Electronics and Communication Systems, p. 1-5.

Pudil, P., Novovičová, J., & Kittler, J. (1994). Floating search methods in feature selection, Pattern recognition letters 15.11 (1994): p.1119-1125.

Quellec G, Lee K, Dolejsi M, Garvin MK, Abràmoff MD, Sonka M (2010). Three-dimensional analysis of retinal layer texture: identification of

fluid-filled regions in SD-OCT of the macula, Copyright @ IEEE Trans Med Imaging, Vol. 29, (No. 6), p.1321–1330.

Quigley.H. A. (1999). Neuronal death in glaucoma, Progress in Retinal and Eye Research, Vol. 18, No. 1, p. 39 – 57.

Quigley, A T Broman (2006). The number of people with glaucoma worldwide in 2010 and 2020, Br J Ophthalmol 2006, Vol. 90, p.262–267. doi: 10.1136/bjo.2005.081224.

Ravi Thomas1, Klaus Loibl1, Rajul Parikh3 (2011), Evaluation of a glaucoma patient, Indian J Ophthalmol: 2011; 59 Suppl 1:S43-52 DOI: 10.4103/0301-4738.73688 PMID: 21150033.

Ravi & Khan, Am. (2013). Morphological Operations for Image Processing: Understanding and its Applications, NCVSComs-13 conference proceedings.

Rama Krishnan M, Muthu and Faust, Oliver (2012). Automated Glaucoma Detection Using Hybrid Feature Extraction in Retinal Fundus Images, Journal of Mechanics in Medicine and Biology, Vol.13 (1), p.1350011-1350032.

Ramaswamy, Akshaya; Ram, Keerthi; and Sivaprakasam, Mohanasankar. (2016) A Depth Based Approach to Glaucoma Detection Using Retinal Fundus Images. In: Chen X, Garvin MK, Liu J, Trucco E, Xu Y editors. Proceedings of the Ophthalmic Medical Image Analysis Third International Workshop, OMIA 2016, Held in Conjunction with MICCAI 2016, Athens, Greece, October 21, p. 9–16. Available from https://doi.org/10.17077/omia.1041.

Ranjith.N., C. Saravanan, M. R. Bibin (2015). International Journal of Inventive Engineering and Sciences (IJIES) ISSN: 2319–9598, Vol.3, Issue.5.

Ritch.R and J. M. Liebermann (1999). Angle closure glaucoma, Asian Journal of Ophthalmology, Vol. 1, (No. 3), p. 10–16.

Ritch.R, J. Liebmann, and C. Tello (1995). A construct for understanding angle-closure glaucoma: the role of ultrasound bio microscopy, Ophthalmology Clinics of North America, Vol. 8, p. 281–293.

Sirshad, Xiaoxia Yin2, Lucy Qing Li3,4, and Umer Salman5 (2016). Automatic Optic Disk Segmentation in Presence of Disk Blurring, Springer International Publishing, Part I, LNCS 10072, p. 13–23, DOI: 10.1007/978-3-319-50835-1_2.

Sahu, A., Runger, G., Apley, D. (2011). Image denoising with a multi-phase kernel principal component approach and an ensemble version, IEEE Applied Imagery Pattern Recognition Workshop, p.1-7.

Sakthivel Karthikeyan and 2N. Rengarajan. (2014). Performance analysis of gray level co-occurrence matrix texture features for glaucoma diagnosis, American Journal of Applied Sciences, VOL 11, p. 248-257, 2014 ISSN: 1546-9239 ©2014 Science Publication.

Sakthivel K, Narayanan R. (2015), An automated detection of glaucoma using histogram features, Int J Ophthamol, vol.8(1), p.194-200.

Salam, A.A., Khalil, T., Akram, M.U., Jameel, A. and Basit, I. (2016). Automated detection of glaucoma using structural and non-structural features. Springer Plus, Vol.5 (1), p.1519.

Sample.P. A, C. F. Bosworth, E. Z. Blumenthal, C. Girkin, and R. N.Weinreb (2000). “Visual function-specific perimetry for indirect

comparison ofdifferent ganglion cell populations in glaucoma". Investigative Ophthalmology& Visual Science, Vol. 41, (No. 7), p. 1783–1790.

Satish T, Sunita J (2015). Optic Disc and Cup Segmentation for glaucoma Screening based on Superpixel classification , International Journal of Innovations & Advancement in Computer Science IJIACS ISSN 2347 – 8616 Volume 4, Special Issue (March 2015).

Sek-Tien Hoh, (2007). Analysis of Fused Ophthalmologic Image Data, Research Gate, V O L. 4 7, No 3, P. 4 5 5 – 4 8 1.

Senthilk umaran and R. Rajesh (2009). Edge Detection Techniques for Image Segmentation–A Survey of Soft Computing Approaches, International Journal of Recent Trends in Engineering, Vol. 1, (No. 2, May 2009).

Sharanagouda Nawaldgi and Y, S. Lalitha. (2017), a Novel Combined Color Channel and ISNT Rule Based Automatic Glaucoma Detection from Color Fundus Images, Indian Journal of Science and Technology, Vol. 10(13), DOI: 10.17485/ijst/2017/v10i13/111722.

Shields.M. B. (2008). Normal-tension glaucoma: is it different from primaryopen-angle glaucoma?, Current Opinion in Ophthalmology, Vol. 19, (No. 2), p. 85–88.

Shijian Lu and Joo Hwee Lim (2010). Automatic optic disc detection through background estimation, Proceedings of 2010 IEEE 17th International Conference on Image Processing, Hong Kong, (September 26-29, 2010).

Shinde, Amit, Anshuman Sahu, Daniel Apley, and George Runger (2014). Pre images for Variation Patterns from Kernel PCA and Bagging, IIE Transactions, Vol.46, Iss.5.

Siddeeqa, Murugan C, Golodza BZ, Pillay K, et al.(2015). Retinal nerve fibre layer thickness of black and Indian myopic students at the University of KwaZulu- Natal. Afr Vision Eye Health. 2015, Vol. 74 (1), Art. #24, 6 pages. http://dx.doi.org/10.4102/ aveh.v74i1.24.

Sivaswamy, Jayanthi & Krishnadas, Subbaiah & Joshi, Gopal & Jain, Madhulika & Ujjwaft Syed Tabish, A. (2014). Drishti-GS: Retinal image dataset for optic nerve head(ONH) segmentation, 2014 IEEE 11th International Symposium on Biomedical Imaging, ISBI 2014. 53-56. 10.1109/ISBI.2014.6867807.

Sirel Gür Güngör, Ahmet Akman (2017). Are All Retinal Nerve Fiber Layer Defects on Optic Coherence Tomography Glaucomatous?, Turk J Ophthalmol ,VOL. 47, P. 267-273, DOI: 10.4274/tjo.86461.

SobiaNaz, 2, Sheela N Rao (2014). Glaucoma Detection in Color Fundus Images Using Cup to Disc Ratio, The International Journal of Engineering and Science (IJES), Volume 3, Issue 6, p. 51-58, ISSN (e): 2319 – 1813 ISSN (p): 2319 – 1805.

Soille, P. (1999). Morphological Image Analysis: Principles and Applications, Springer, p. 164-165.

Sommer.A, J. M. Tielsch, J. Katz, H. A. Quigley, J. D. Gottsch, J. Javitt, and Sing (1991). Relationship between intraocular pressure and primary open angle glaucoma among white and black Americans: The Baltimore eye survey, Arch Ophthalmol, Vol. 109, (No. 8), p. 1090–1095.

Stricker. M and M. Orengo (1995). Similarity of Color Images, In SPIE Conference on Storage and Retrieval for Image and Video Databases III, (Feb. 1995), Vol. 2420, p. 381-392.

Sundari.B1, Sivaguru.S2 (2017). Early Detection of Glaucoma from Fundus Images by Using MATLAB GUI for Diabetic Retinopathy, International Journal of Innovative Research in Computer and Communication Engineering, An ISO 3297: 2007 Certified Organization, Vol. 5, Issue 1, (January 2017).

Swati Saxena1, R.L Yadav 2 (2015). Hybrid Feature of Tamura Texture Based Image Retrieval System, International Journal of Recent Research and Review, Vol. VIII, Issue 2, (June 2015), ISSN 2277 – 8322.

Swapna P.P., and Mini M.G. (2016), A Regression Neural Network based Glaucoma Detection System using Texture Features, Int'l Journal of Computing, Communications & Instrumentation Eng. (IJCCIE), Vol. 3, Issue 2, ISSN 2349-1469 EISSN 2349-1477.

Syed Akhter Hussain (2015). Automated Detection and Classification of Glaucoma from Eye Fundus Images: A Survey, (IJCSIT) International Journal of Computer Science and Information Technologies, Vol. 6 (2).

Syed M,Kwang h. (2016). Depth edge detection by image-based smoothing and morphological operations, Journal of Computational Design and Engineering 3 p.191–197. Available online at, www. sciencedirect. com.

Thresiamma Devasia, Poulose Jacob and Tessamma Thomas.(2015), Fuzzy clustering based glaucoma detection using the CDR, Signal & Image Processing : An International Journal (SIPIJ) Vol.6, No.3.

Tyler , Patrick J. Saine and Marshall E.(2014). Fundus Photography Overview, Ophthalmic Photography society, ISBN: 0750673729, www.opsweb.org/page/fundusphotography.

Uchida.H, S. Ugurlu and J. Caprioli (1998). Increasing peripapillary atrophy is associated with progressive glaucoma, Ophthalmology, vol. 105, (no. 8, Aug 1998), p. 1541–1545.

Vaishnavi Kamat, Shruti Chatti, Alvira Rodrigues, Chinmayee Shetty, Anusaya Vadji (2017). Glaucoma Detection Using Enhanced K-Strange Points Clustering Algorithm and Classification, IOSR Journal of Computer Engineering (IOSR-JCE) e-ISSN: 2278-0661, p-ISSN: 2278-8727, Vol. 19, Issue 4, P. 44-49.

Weinreb.R. N. And P. T. Khaw (2004). Primary open-angle glaucoma, The Lancet, Vol. 363, (No. 9422), p. 1711–1720.

Wong, D.W.K. ; Jiang Liu ; Joo Hwee Lim ; Ngan Meng Tan ; Zhuo Zhang ; Huiqi Li ; Shijian Lu ; Tien Yin Wong (2010). Method of detecting kink-bearing vessels in a retinal fundus image (CDR), The 5th IEEE Conference on Industrial Electronics and Applications (ICIEA), (June 2010), p. 1690 – 1694.

Xu.J, O. Chutatape, E. Sung, C. Zheng, and P. C. T. Kuan (2007). Optic Disk Feature Extraction via Modified Deformable Model Technique for Glaucoma Analysis, Pattern Recognition, Vol. 40, p. 2063–2076.

Yazdanpanah A, Hamarneh G, Smith B, Sarunic M. (2009). Intra-retinal layer segmentation in optical coherence tomography using an active

contour approach. Med Image Comput Assist Interv, Vol.12, No. 2, p.649–656.

Youssif.A. A. A, A. Z. Ghalwash and A. A. S. A. Ghoneim (2008). Optic Disc Detection from Normalized Digital Fundus Images by Means of a Vessels' Direction Matched Filter, IEEE Transactions on Medical Imaging, Vol. 27 (no. 1), p. 11-18.

Yucel.Y. H., Q. Zhang, R. N. Weinreb, P. L. Kaufman, and N. Gupta (2003). "Effects of retinal ganglion cell loss on magno, parvo, konio cellular path ways in the lateral geniculate nucleus and visual cortex in glaucoma, Progress in Retinal and Eye Research, Vol. 22, (No. 4), p. 465–481.

Yuan Sui, Ying Wei, and Dazhe Zhao (2015). Computer-Aided Lung Nodule Recognition by SVM Classifier Based on Combination of Random Undersampling and SMOTE, Hindawi Publishing Corporation Computational and Mathematical Methods in Medicine, Vol. 2015, Article ID 368674, p. 13, http://dx.doi.org/10.1155/2015/368674

Zhang Zhuo, Ruchir Srivastava, Huiying Liu, Xiangyu Chen, Lixin Duan1, Damon Wing Kee Wong, Chee Keong Kwoh, Tien Yin Wong3 and Jiang Liu (2014). A survey on computer aided diagnosis for ocular diseases, BMC Medical Informatics and Decision Making, Copyright @ www.biomedcentral.com/1472-6947/14/80, p.2-29.

Zhang Z, Khow CK, Liu J, Cheung YLC, Aung T, et al. (2012). Automatic Glaucoma Diagnosis with mRMR-based Feature Selection. J Biomet Biostat, S7:008. doi:10.4172/2155-6180.S7-008.

Zhi-Hua Zhou, Ensemble Learning, National Key Laboratory for Novel Software Technology, Nanjing University, Nanjing 210093, China zhouzh@nju.edu.cn, p.1-5.

Zhou, W., A. C. Bovik, H. R. Sheikh, and E. P. Simoncelli (2004). Image Qualifty Assessment: From Error Visibility to Structural Similarity, IEEE Transactions on Image Processing. Vol. 13, Issue 4, (April 2004), p. 600–612.

Zhou Zhang , Khow CK, Liu J, Cheung YLC, Aung T, et al. (2012) Automatic Glaucoma Diagnosis with mRMR-based Feature Selection. J Biomet Biostat S7:008. doi:10.4172/2155-6180.S7-008.

Zhuo Zhang ,Jiang Liu , Cherian, N.S. ,Ying Sun, Joo Hwee Lim , Wing Kee Wong , Ngan Meng Tan ,Shijian Lu , Huiqi Li , Tien Ying Wong. (2009), Convex hull based neuro-retinal optic cup ellipse optimization in glaucoma diagnosis, Engineering in Medicine and Biology Society.

Zuiderveld.K. (1994). Contrast limited adaptive histogram equalization, in Graphics Gems IV, Academic Press, p. 474–485.

Website

AdiBronshtein, Data Scientist, https://medium.com/@adi.bronshtein/a-quick-introduction to k-nearest-neighbors algorithm-62214cea29c7, Apr (Jan, 2017).

AucklandUniversity https:// www.cs.auckland.ac. nz/courses/compsci773s1c /lectures/ImageProcessing-html/topic4.htm.

Computerized Medical Imaging and Graphics, (2014). Vol. 38, p. 508–516, copyright@ www.biomedical-engineering-online.com.

Channel (digital image) (2018). https://en.wikipedia.org/wiki/Channel_ (digital image), last edited on (9 February), at 08:37.

Community eye health, https://www.google .com/search?q=Anatomy+ of+the+Optic+Nerve+Head+-+Clinical+features+of+the+optic+ nerve.&safe=strict&client=firefox-b&source=lnms&tbm= isch&sa= X&ved=0ahUKEwjgjqipwcHcAhULNhoKHSbvAG4Q_AUICigB &biw=1252&bih=600#imgrc=Tgl6p5qv865crM:, (SEP, 2017).

Eye diseases, https://www.google .com/search?q=Vision+with+ normal+ eye+(bad)+Vision+with+GLAUCOMA+eye&safe=strict&client=fir efox-b&source= lnms&tbm= isch&sa=X&ved= 0ahUKEwjp0 eShr MHcAhUSUBoKHR1EBSkQ_AUICigB&biw=1252&bih=600#im grc=-bBiwYWqvqqhcM, (OCT, 2017).

GLCM Texture Feature, https:/ /support. echo view. com ComebHelp /Windows_and_Dialog_Boxes/Dialog_Boxes/Variable_properties_ dialog_box/Operator_pages/GLCM_Texture_Features, Wednesday 8th November 2017.

GLCM matlab code, https:/ /www.mathworks. com/matlabcentral / fileexchange /22187-glcm-texture-features

Copyright (c) 2008, Avinash Uppuluri, All rights reserved.

GLCM Alogorithm, (https:/ /support.echoview .com/ Web Help/ Windows _and_ Dialog_ Boxes /Dialog_ Boxes/Variable_properties _dialog_ box/Operator_pages/GLCM_Texture_Features.htm), visited at (AUG, 2018)

Heidelberg engineering,https://www .google.com/search? safe=strict&client =firefox- b&biw= 1252&bih=600&tbm =isch&sa=1&ei=sQNcW_ OoHouSaMnFiPAO&q=Heidelberg+Retina+Tomography+HRT+i mage&oq=Heidelberg+Retina+Tomography+HRT+image&gs_l=im g.12...33928.36238.0.38324.2.2.0.0.0.0.1211.1473.2-1j7-1.2.0.... 0... 1c.1.64.img..0.0.0....0.M-bc1KS CONE#imgrc= RpiyWY0y9tmOK M,(Dec,2017).

Human eye structure, www.shutterstock.com, (April, 2017).

Eye source, http://www.ammoparadise.com/anatomy-and-physiology-of-the-human-eye/, (April, 2017).

Regions properties function, https://octave. Source forge. Io/image/function/ regionprops.html, (May, 2017).

Retina Image Bank, http://imagebank.asrs.org/discover-new/ files/4/ 25? q = fundus %20autofluorescence%20(faf),(May,2018).

Math Works. https://www.mathworks.com/discovery/image segmentation. Html,(Feb, 2018) .

The MathWorks, Inc., "Marker-Controlled Watershed Segmentation, [Online]. Available: http:// www.m athworks.com/ products/demos/ image/watershed/ipexwatershed.html, (Aug, 2013).

What are the mean and median filters, https://www. markschulze. Net /java/ meanmed. html, (Nov,2017).

Median filter, https://en.wikipedia.org/wiki/Median_filter , (Nov, 2017).

Morphological Image Processing, https://www. cs.auckland.ac.nz/courses/ compsci773s1c/lectures/ImageProcessinghtml/topic4.htm?_ga=2.48 742822.1040376964.1531844914443133705.1524854676, (Dec,2016).

OCT, https://www.google.com/search?safe=strict&client=firefox-b&biw=1252&bih=600&tbm=isch&sa=1&ei=FSVcW5fWKY-Wa5WRn8gC&q=images+produced+via+Optical+Coherence+Tomography%28OCT%29+images&oq=images+produced+via+Optical+Coherence+Tomography%28OCT%29+images&gs_l=img.12...308366.311585.0.314570.7.7.0.0.0.0.505.2162.2-4j2j0j1.7.0....0...1c.1.64.img..0.0.0. ...0.w 0FO0Y 2DPXI# imgrc=k8wyMn 8bfPmjHM: (Aug, 2017).

Practical Guide to deal with Imbalanced Classification Problems, https://www.analyticsvidhya.com/blog/2016/03/practical-guide-deal-imbalanced-classification-problems/,(July,2018).

Tamura Features Matlab, Coded by Sudhir Sornapudi, https://github.com/Sdhir/TamuraFeaturesm, Copyright (c) 2014, Sudhir Sornapudi, All rights reserved.

Retinal imaging device modified from smart phone, https://www.google.com/search?q=fundus+camera+using+smart+phone&safe=strict&client=firefox-b&source=lnms&tbm=isch&sa=X&ved=0ahUKEwiV4uzgisHcAhUPUBoKHS47DpsQ_AUICigB&biw=1252&bih=600#imgrc=gwi-W6w9uaApzM (July,2018).

Suport Vector Machine, (https://www. analyticsvidhya. com/blog/2017 /09/ understaing -support-vector-machine-example-code/), visited at (OCT,2017).

APPENDIX

I. This matlab code is the main code use for fundus image preprocessing, segmentation and feature extraction.

```
function results = od_and_oc(im)
%Image Processing Function
% IM - Input image.
% RESULTS - A scalar structure with the processing results.
%this code for optic cup &optic disc segmentation.
%, CUP and DISC and RNFL features extraction.
%all this feature will use for classification healthy image form glaucoma
% Image Preprocessing (resize, histogram equalization, vessel remove and
%filtering)
Im=imresize(im,[256,256]);
% subplot(131),imshow(Im)
% title('orginal image');
results.Im=Im;
w=color_filt(Im);
% Blood Vessel Remove Step
se=strel('disk',8);
a= imopen(w,se);
%figure,imshow(a)
c= imopen(a,se);
d= imopen(c,se);
e= imopen(d,se);
f= imopen(e,se);
g= imdilate(f,se);
he= imclose(g,se);
% subplot(332),imshow(he)
% title('vessel removed image');
% results.he=he;
% close all
f=he(:,:,1);
% f=imhist(f)
% subplot(322),imshow(f)
% title('red channel ');
v=histeq(f);
% subplot(334),imshow(v)
% title('histogram egualization');
% Smax= 3*3;
I1 = medfilt2(v,[5 5]);
% subplot(335),imshow(I1)
% title('filtered image');
% Optic Disc Segmentation Step
[m,n]=size(I1);
I3=zeros(m,n);
for i=1:m
for j=1:n
if I1(i,j)>180
I3(i,j)=1;
else
I3(i,j)=0;
```

```
end
end
end
se=strel('disk',8);
I4=imdilate(I3,se);
I4_1=immultiply(double(I4),double(I1));
% subplot(232),imshow(uint8(I4_1))
% title('Segmented disc');
seD = strel('disk',8);
BWfinal = imerode(I4,seD);
BWfinal = imerode(BWfinal,seD);
%subplot(333), imshow(BWfinal), title('segmented image');
% Clear and smooth the disc boundary
M2 = imclearborder(BWfinal);
%subplot(334),imshow(M2)
bw2 = imdilate(M2,se);
d = imdilate(bw2,se);
%subplot(335),imshow(d), title('Original')
BM = bwareaopen(d , 2000);
% subplot(337), imshow(BM);
% title('cleared border image');
a=edge(BM);
[c cc]=find(a~=0);
% subplot(334),imshow(a,[])
level = graythresh(I4_1);
mas=im2bw(BM,level);
ma=~mas;
mask=ma;
% subplot(133),imshow( mas)
% title('disc mask');
s = regionprops(1-
ma,'Centroid','Area','MajorAxisLength','MinorAxisLength');
s.MajorAxisLength
s.MinorAxisLength
s.Centroid
% results.discarea=s.Area;
% discMajorAxisLength=s.MajorAxisLength;
radius1 = sum(sqrt((c-s.Centroid(1)).^2+(c-
s.Centroid(1)).^2)/(1*length(c)));
% h = imellipse(gca,[s.Centroid(1)-radius1 s.Centroid(2)-radius1
2*radius1 2*radius1]);
% Create a logical image of a circle with specified diameter, center, and
image size.
% First create the image.
imageSizeX = 256;
imageSizeY = 256;
[columnsInImage rowsInImage] = meshgrid(1:imageSizeX, 1:imageSizeY);
% Next create the circle in the image.
centerX = s.Centroid(1);
centerY = s.Centroid(2);
radius=radius1;
%Disc Reconstruction as a Circle
circlePixels = (rowsInImage - centerY).^2 ...
+ (columnsInImage - centerX).^2 <= radius.^2;
% circlePixels is a 2D "logical" array.
% Now, display it.
```

```
% image(circlePixels) ;
% colormap([0 0 0; 1 1 1]);
% title('Binary image of a circle');
% subplot(233),imshow(circlePixels)
 % title('constructed disc');
% results.circlePixels=circlePixels;
% Disc Shape Features Extraction
stat2 =
regionprops(circlePixels,'Centroid','Area','ConvexArea','EquivDiameter','
perimeter','ConvexHull','ConvexImage','Eccentricity','EulerNumber',...
'Extent','Extrema','FilledArea','MajorAxisLength','MinorAxisLength','Orie
ntation','Solidity' );
stat2.EquivDiameter
stat2.ConvexArea
stat2.Centroid
stat2.Area
stat2.Perimeter
% s.BoundingBox
stat2.Eccentricity
% stat2.EulerNumber
stat2.Extent
stat2.FilledArea
stat2.MajorAxisLength
stat2.MinorAxisLength
stat2.Orientation
stat2.Solidity
%results.disc_center=stat2.Centroid;
disc_area=stat2.Area;
results.disc_area=disc_area;
results.xEccentricity=stat2.Eccentricity;
results.xExtent=stat2.Extent;
results.xFilledArea=stat2.FilledArea;
results.xMajorAxisLength=stat2.MajorAxisLength;
results.xMinorAxisLength=stat2.MinorAxisLength;
results.xOrientation=stat2.Orientation;
results.xPerimeter=stat2.Perimeter;
results.DISC_solidity=stat2.Solidity;
results.xEquivDiameter=stat2.EquivDiameter;
results.xConvexArea=stat2.ConvexArea;
disc_radius = sum(sqrt((c-stat2.Centroid(1)).^2+(c-
stat2.Centroid(1)).^2)/(.8*length(c)));
results.disc_radius=disc_radius;
discdiameters = mean([stat2.MajorAxisLength stat2.MinorAxisLength],2);
results.discdiameters=discdiameters;
% Disc Color Features Extraction
discRgbImage = bsxfun(@times, w, cast( circlePixels, 'like', w));
% figure,imshow(discRgbImage);
image=discRgbImage;
% extract color channels
R = double(image(:, :, 1));
G = double(image(:, :, 2));
B = double(image(:, :, 3));
% compute 2 first color moments from each channel
meanR = mean( R(:) );
stdR = std( R(:) );
meanG = mean( G(:) );
```

```
stdG = std( G(:) );
meanB = mean( B(:) );
stdB = std( B(:) );
skewessR = skewness( R(:) );
results.discskewnessR=skewessR;
skewessG = skewness( G(:) );
results.discskewnessG=skewessG;
skewessB = skewness( B(:) );
results.discskewnessB=skewessB;
results.DISC_meanR=meanR;
results.DISC_stdR=stdR;
results.discmeanG=meanG;
results.discstdG=stdG;
results.discmeanB=meanB;
results.discstdB=stdB;
% Optic Cup Segmentation Step
[m,n]=size(I4_1);
I9=zeros(m,n);
for i=1:m
for j=1:n
if I4_1(i,j)>240
I9(i,j)=1;
else
I9(i,j)=0;
end
end
end
se=strel('disk',10);
cupied=imdilate(I9,se);
final_cupied=immultiply(double(cupied),double(I4_1));
% subplot(234),imshow(uint8(final_cupied))
% title(' segmented cup');
% Clear and Smooth Cup Boundary
seD = strel('disk',8);
BWfinal1 = imerode(cupied,seD);
BWfinal1 = imerode(BWfinal1,seD);
% %subplot(333), imshow(BWfinal), title('segmented image');
M22 = imclearborder(BWfinal1);
% subplot(335),imshow(M22),title('cleared border image');
bw22 = imdilate(M22,se);
d1 = imdilate(bw22,se);
% % subplot(335),imshow(d),
BM1 = bwareaopen(d1 , 2000);
% % subplot(333), imshow(BM1);
a=edge(BM1);
[c cc]=find(a~=0);
% % subplot(4,4,13),imshow(a,[])
level = graythresh(final_cupied);
mas2=im2bw(BM1,level);
% subplot(235),imshow( mas2)
% results.cup=mas2;
ma2=~mas2;
mask2=ma2;
% subplot(335),imshow( mask2)
% title('cup mask');
% Cup Shape Features Extraction
```

```
stat = regionprops(1-
ma2,'Centroid','Area','ConvexArea','EquivDiameter','perimeter','BoundingB
ox','ConvexHull','ConvexImage','Eccentricity','EulerNumber',...
'Extent','Extrema','FilledArea','MajorAxisLength','MinorAxisLength','Orie
ntation','Solidity' );
 stat.EquivDiameter;
stat.ConvexArea;
% stat.Centroid;
stat.Area;
stat.Perimeter;
% s.BoundingBox
stat.Eccentricity;
% stat2.EulerNumber
stat.Extent;
stat.FilledArea;
stat.MajorAxisLength;
stat.MinorAxisLength;
stat.Orientation
stat.Solidity
cup_area=stat.Area;
results.ucup_area=cup_area;
results.uEccentricity=stat.Eccentricity;
results.uExtent=stat.Extent;
results.uFilledArea=stat.FilledArea;
results.uMajorAxisLength=stat.MajorAxisLength;
results.uCUP_MinorAxisLength=stat.MinorAxisLength;
results.uOrientation=stat.Orientation;
results.uPerimeter=stat.Perimeter;
results.uSolidity=stat.Solidity;
results.uEquivDiameter=stat.EquivDiameter;
results.uConvexArea=stat.ConvexArea;
%results.cup_center=stat.Centroid;
cupdiameters = mean([stat.MajorAxisLength stat.MinorAxisLength],2);
results.xcupdiameters=cupdiameters;
cup_radius = sum(sqrt((c-stat.Centroid(1)).^2+(c-
stat.Centroid(1)).^2)/(.8*length(c)));
results.xcup_radius=cup_radius;
% h = imellipse(gca,[stat.Centroid(1)-radius2 stat.Centroid(2)-radius2
2*radius2 2*radius2]);
% Cup Color Features Extraction
cupRgbImage = bsxfun(@times, w, cast( mas2, 'like', w));
% % figure,imshow(cupRgbImage);
imagec=cupRgbImage;
% extract color channels
Rc = double(imagec(:, :, 1));
Gc = double(imagec(:, :, 2));
Bc = double(imagec(:, :, 3));
% compute 2 first color moments from each channel
meanR = mean( Rc(:) );
stdR = std( Rc(:) );
meanG = mean( Gc(:) );
stdG = std( Gc(:) );
meanB = mean( Bc(:) );
stdB = std( Bc(:) );
skewessR = skewness( Rc(:) );
results.ycupskewnessR=skewessR;
```

```
skewessG = skewness( Gc(:) );
results.ycupskewnessG=skewessG;
skewessB = skewness( Bc(:) );
results.ycupskewnessB=skewessB;
results.yCUPmeanR=meanR;
results.yCUPstdR=stdR;
results.ycupmeanG=meanG;
results.ycupstdG=stdG;
results.ycupmeanB=meanB;
results.ycupstdB=stdB;
% RNFL Determine Step
mam=1-circlePixels;
% subplot(131),imshow(mam);title ('RNFL ROI')
%RNFL Color Features Extraction
rnfl = bsxfun(@times, he, cast( mam, 'like', he));
% subplot(132), imshow(rnfl);title(' orginal RNFL')
imager=rnfl;
% extract color channels
Rr = double(imager(:, :, 1));
Gr = double(imager(:, :, 2));
Br = double(imager(:, :, 3));
% % compute 2 first color moments from each channel
meanR = mean( Rr(:) );
stdR = std( Rr(:) );
meanG = mean( Gr(:) );
stdG = std( Gr(:) );
meanB = mean( Br(:) );
stdB = std( Br(:) );
skewessR = skewness( Rr(:) );
results.xrnflskewnessR=skewessR;
skewessG = skewness( Gr(:) );
results.xrnflskewnessG=skewessG;
skewessB = skewness( Br(:) );
results.xRNFLskewnessB=skewessB;
results.xrnflmeanR=meanR;
results.xrnflstdR=stdR;
results.xrnflmeanG=meanG;
results.xrnflstdG=stdG;
results.xrnflmeanB=meanB;
results.xrnflstdB=stdB;
% RNFL Texture Features Extraction (Tamara, GLCM algorithm)
h=rnfl;
t = tamara_mothed(h);
coarseness = getfield(t, 'coarseness');
contrast = getfield(t, 'contrast');
direction = getfield(t, 'direction');
results.xrnflcoarseness=coarseness;
results.xrnflcontrast=contrast;
results.xrnfldirection=direction;
k=rgb2gray(rnfl);
% % subplot(133), imshow(k);title(' gray RNFL')
% C1= imge(:,:,1);
% % subplot(4,4,11),imshow(C1);
% C2= imge(:,:,2);
% % subplot(4,4,12),imshow(C2);
% k=C2;
```

```
GLCM2 = graycomatrix(k);
% % % % % % 'Offset',[2 0;0 2]);
sts = GLCM_Features2_modified(GLCM2,0);
v1 = getfield(sts, 'autoc');
v2 = getfield(sts, 'contr');
v3 = getfield(sts, 'corrm');
v4 = getfield(sts, 'corrp');
v5 = getfield(sts, 'cprom');
v6 = getfield(sts, 'cshad');
v7 = getfield(sts, 'dissi');
v8= getfield(sts, 'energ');
v9 = getfield(sts, 'entro');
v10 = getfield(sts, 'homom');
v11 = getfield(sts, 'homop');
v12 = getfield(sts, 'maxpr');
v13 = getfield(sts, 'sosvh');
v14 = getfield(sts, 'savgh');
v15 = getfield(sts, 'svarh');
v16 = getfield(sts, 'senth');
v17 = getfield(sts, 'dvarh');
v18 = getfield(sts, 'denth');
v19 = getfield(sts, 'inf1h');
v20 = getfield(sts, 'inf2h');
v21 = getfield(sts, 'indnc');
v22 = getfield(sts, 'idmnc');
results.zzv1=v1;
results.zzv2=v2;
results.zzv3=v3;
results.zzv4=v4;
results.zzv5=v5;
results.zzv6=v6;
results.zzv7=v7;
results.zzv8=v8;
results.zzv9=v9;
results.zzv10=v10;
results.zzv11=v11;
results.zzv12=v12;
results.zzv13=v13;
results.zzv14=v14;
results.zzv15=v15;
results.zzv16=v16;
results.zzv17=v17;
results.zzv18=v18;
results.zzv19=v19;
results.zzv20=v20;
results.zzv21=v21;
results.zzv22=v22;
```

GUI Code

II. This matlab code generated by GUI guide to be a window show fundus image, segmentations, selected features and final diagnose to the users.

```
function varargout = project_gui(varargin)
% PROJECT_GUI MATLAB code for project_gui.fig
% PROJECT_GUI, by itself, creates a new PROJECT_GUI or raises the
existing
% singleton*.
%
% H = PROJECT_GUI returns the handle to a new PROJECT_GUI or the handle
to% the existing singleton*.
%
% PROJECT_GUI('CALLBACK',hObject,eventData,handles,...) calls the local
% function named CALLBACK in PROJECT_GUI.M with the given input
arguments.
%
% PROJECT_GUI('Property','Value',...) creates a new PROJECT_GUI or raises
the
% existing singleton*. Starting from the left, property value pairs are
% applied to the GUI before project_gui_OpeningFcn gets called. An
% unrecognized property name or invalid value makes property application
% stop. All inputs are passed to project_gui_OpeningFcn via varargin.
%
% *See GUI Options on GUIDE's Tools menu. Choose "GUI allows only one
% instance to run (singleton)".
%
% See also: GUIDE, GUIDATA, GUIHANDLES
% Edit the above text to modify the response to help project_gui
% Last Modified by GUIDE v2.5 29-May-2018 16:40:55
% Begin initialization code - DO NOT EDIT
gui_Singleton = 1;
gui_State = struct('gui_Name', mfilename, ...
'gui_Singleton', gui_Singleton, ...
'gui_OpeningFcn', @project_gui_OpeningFcn, ...
'gui_OutputFcn', @project_gui_OutputFcn, ...
'gui_LayoutFcn', [] , ...
'gui_Callback', []);
if nargin && ischar(varargin{1})
gui_State.gui_Callback = str2func(varargin{1});
end
if nargout
[varargout{1:nargout}] = gui_mainfcn(gui_State, varargin{:});
else
gui_mainfcn(gui_State, varargin{:});
end
% End initialization code - DO NOT EDIT
% --- Executes just before project_gui is made visible.
function project_gui_OpeningFcn(hObject, eventdata, handles, varargin)
% This function has no output args, see OutputFcn.
% hObject handle to figure
% eventdata reserved - to be defined in a future version of MATLAB
% handles structure with handles and user data (see GUIDATA)
```

```
% varargin command line arguments to project_gui (see VARARGIN)
% Choose default command line output for project_gui
handles.output = hObject;
% Update handles structure
guidata(hObject, handles);
% UIWAIT makes project_gui wait for user response (see UIRESUME)
% uiwait(handles.figure1);
% --- Outputs from this function are returned to the command line.
function varargout = project_gui_OutputFcn(hObject, eventdata, handles)
% varargout cell array for returning output args (see VARARGOUT);
% hObject handle to figure
% eventdata reserved - to be defined in a future version of MATLAB
% handles structure with handles and user data (see GUIDATA)
% Get default command line output from handles structure
varargout{1} = handles.output;
% --- Executes on button press in feature_button.
function feature_button_Callback(hObject, eventdata, handles)
% hObject handle to feature_button (see GCBO)
% eventdata reserved - to be defined in a future version of MATLAB
% handles structure with handles and user data (see GUIDATA)
global d results
results = final_features(d);
set (handles.text12,'String',results.uCUP_MinorAxisLength)
set (handles.text13,'String',results.DISC_solidity)
set (handles.text14,'String',results.yCUPmeanR)
set (handles.text15,'String',results.yCUPstdR)
set (handles.text16,'String',results.DISC_meanR)
set (handles.text17,'String',results.DISC_stdR)
set (handles.text18,'String', results.xrnflcoarseness)
% --- Executes on button press in giagnose_button.
function giagnose_button_Callback(hObject, eventdata, handles)
% hObject handle to giagnose_button (see GCBO)
% eventdata reserved - to be defined in a future version of MATLAB
% handles structure with handles and user data (see GUIDATA)
% global selected_features
global results
% load dbtrainedClassifier
load oldrimtrainedClassifier
% load model7.mat
% load selected_features
H=[results.DISC_meanR,results.DISC_solidity,results.DISC_stdR,results.uCU
P_MinorAxisLength,results.yCUPmeanR,results.yCUPstdR,results.xrnflcoarsen
ess];
%
FF=[results.CUP_MinorAxisLength,results.CUP_meanR,results.CUP_stdR,result
s.DISC_meanR,results.DISC_stdR];%,
results.rnflstdR,results.Eccentricity,results.zzv1,results.zzv15];
% FF yfit = trainedModel.predictFcn(selected_features(20,1:10))
% yfit = trainedClassifier7.predictFcn(FF)
% yfit = dbtrainedClassifier.predictFcn(H)
yfit = oldrimtrainedClassifier.predictFcn(H)
if yfit==1
set (handles.final,'String','GLAUCOMA')
elseif yfit==0
set (handles.final,'String','NON-GLAUCOMA')
end
```

```
% --- Executes on button press in segment_button.
function segment_button_Callback(hObject, eventdata, handles)
% hObject handle to segment_button (see GCBO)
% eventdata reserved - to be defined in a future version of MATLAB
% handles structure with handles and user data (see GUIDATA)
global d
results2 = od_and_oc(d);
axes(handles.axes3)
imshow(results2.discRgbImage), title ('Optic Disc')
axes(handles.axes5)
imshow(results2.cupRgbImage), title ('Optic Cup')
% --- Executes on button press in pushbutton5.
function pushbutton5_Callback(hObject, eventdata, handles)
% hObject handle to pushbutton5 (see GCBO)
% eventdata reserved - to be defined in a future version of MATLAB
% handles structure with handles and user data (see GUIDATA)
% --- Executes on button press in pushbutton6.
function pushbutton6_Callback(hObject, eventdata, handles)
% hObject handle to pushbutton6 (see GCBO)
% eventdata reserved - to be defined in a future version of MATLAB
% handles structure with handles and user data (see GUIDATA)
global d
[filen,pathn]=uigetfile('*.jpg;*.tif;*.bmp');
d=imread([pathn,filen]);
d=imresize(d,[256,256]);
axes(handles.axes2)
imshow(d);
```